ECSS-E-HB-20-01A
15 June 2020



Space engineering

Multipactor handbook

ECSS Secretariat
ESA-ESTEC
Requirements & Standards Division
Noordwijk, The Netherlands

Foreword

This Handbook is one document of the series of ECSS Documents intended to be used as supporting material for ECSS Standards in space projects and applications. ECSS is a cooperative effort of the European Space Agency, national space agencies and European industry associations for the purpose of developing and maintaining common standards.

The material in this Handbook is defined in terms of description and recommendation how to organize and perform the work for the design and test of RF component and equipment to achieve respectable performance with respect to multipactor-free operation in service in space.

This handbook has been prepared by the ECSS-E-ST-20-01C Working Group, reviewed by the ECSS Executive Secretariat and approved by the ECSS Technical Authority.

Disclaimer

ECSS does not provide any warranty whatsoever, whether expressed, implied, or statutory, including, but not limited to, any warranty of merchantability or fitness for a particular purpose or any warranty that the contents of the item are error-free. In no respect shall ECSS incur any liability for any damages, including, but not limited to, direct, indirect, special, or consequential damages arising out of, resulting from, or in any way connected to the use of this document, whether or not based upon warranty, business agreement, tort, or otherwise; whether or not injury was sustained by persons or property or otherwise; and whether or not loss was sustained from, or arose out of, the results of, the item, or any services that may be provided by ECSS.

Published by: ESA Requirements and Standards Office
ESTEC, P.O. Box 299,
2200 AG Noordwijk
The Netherlands
Copyright: 2020© by the European Space Agency for the members of ECSS

Table of contents

Change log **10**

Introduction **11**

1 Scope **12**

2 References **13**

3 Terms, definitions and abbreviated terms **14**

3.1 Terms from other documents 14

3.2 Abbreviated terms 15

4 Verification **16**

4.1 Verification process 16

4.2 Multipactor verification plan 16

4.2.1 Generation and updating 16

4.2.2 Description 16

4.3 Power requirements 16

4.3.1 General power requirements 16

4.4 Classification of equipment or component type 17

4.4.1 General classification of equipment or component type 17

4.5 Verification routes 20

4.6 Single carrier 20

4.6.1 General 20

4.6.2 Verification by analysis 20

4.6.3 Verification by test 20

4.7 Multicarrier 22

4.7.1 General 22

4.7.2 Verification by analysis 22

4.7.3 Verification by test 22

4.8 Bibliography for clause 4 23

5 Design analysis **24**

5.1 Overview 24

5.2 Field analysis 24

5.3 Multipactor design analysis 24

5.3.1 Frequency selection 24

5.3.2 Design analysis levels 24
5.3.3 Available data for Multipactor analysis 58
5.4 Bibliography for clause 5 62

6 Multipactor - Test conditions 64
6.1 Cleanliness 64
6.2 Pressure 65
6.3 Temperature 66
6.4 Signal characteristics 67
6.4.1 Applicable bandwidth 67
6.4.2 Single-frequency test case 67
6.4.3 Multi-frequency test case 68
6.4.4 Pulsed testing 73
6.5 Electron seeding 74
6.5.1 General 74
6.5.2 Multipactor test in CW operation 74
6.5.3 Multipactor test in pulsed operation 74
6.5.4 Multipactor test in multi-carrier operation 74
6.5.5 Seeding sources 74
6.5.6 Seeding verification 82
6.6 Bibliography for clause 6 82

7 Multipactor - Methods of detection 83
7.1 General 83
7.2 Detection methods 83
7.2.1 Introduction 83
7.2.2 Global detection methods 84
7.2.3 Local detection methods 86
7.3 Detection method parameters 87
7.3.1 Verification 87
7.3.2 Sensitivity 87
7.3.3 Rise time 87

8 Multipactor - test procedure 88
8.1 General 88
8.2 Test bed configuration 89
8.3 Test bed validation 89
8.3.1 Reference multipactor test 89
8.4 Test sequence 93

8.4.1 Power profile 93
8.5 Acceptance criteria 93
8.5.1 Definitions 93
8.5.2 Multipactor Free Equipment or component 93
8.5.3 Steps in case of Discharges or Events during test 93
8.5.4 Investigation of Test Anomalies 93
8.6 Test procedure 93
8.6.1 Test procedure for high power loads 93
8.7 Test reporting 97
8.8 Bibliography for clause 8 99

9 Secondary electron emission yield requirements 100
9.1 General 100
9.1.1 SEY definition and properties 100
9.1.2 SEY and Multipactor 101
9.1.3 Factors affecting SEY 102
9.1.4 SEY testing 103
9.2 SEY measurements justification 106
9.3 Worst case SEY measurement 106
9.4 SEY measurements conditions 106
9.4.1 Environmental conditions 106
9.4.2 SEY test bed conditions 115
9.4.3 SEY sample characteristics 118
9.5 SEY measurements procedure 119
9.5.1 SEY Measurements procedure documents 119
9.5.2 SEY measurement calibration 119
9.6 ECSS SEY data selection 120
9.7 Bibliography for clause 9 139

Figures

Figure 4-1: Component assembly with consideration of reflection coefficient 16
Figure 4-2: Isolator block diagram 17
Figure 4-3: Tested component – Coaxial filter 18
Figure 4-4: Multipactor simulations and multipactor measurements with and without thermal baking for a RF component with different dielectric materials 19
Figure 4-5: Schematic diagram of discharge at a triple point in the inverted voltage gradient configuration with potential contours indicated by colour scale. 20
Figure 4-6: Component assembly with consideration of the reflection coefficient of the downstream component assembly for test margin 21

Figure 4-7: Power correction with respect to mismatch of the payload downstream component assembly 21
Figure 5-1: 2D schematic of a typical iris-like structure 25
Figure 5-2: 2D Typical Sombrin chart with fringing field effect for different d/l ratios. ...27
Figure 5-3: 2D Typical multipactor chart computed with non-stationary theory with fringing field effect for different d/l ratios. 28
Figure 5-4: 2D Experimental results corresponding to EVEREST project [5-12] 29
Figure 5-5: 2D Experimental results corresponding to ESA-TESAT activity [5-10].....29
Figure 5-6: 2D Experimental results corresponding to ESA-AURORASAT activity [5-11].....30
Figure 5-7: 2D Numerical results corresponding to ESA-AURORASAT activity [5-11] .30
Figure 5-8: 2D Analytical results corresponding to ESA-AURORASAT activity [5-11]..31
Figure 5-9: Fringing field analysis method 1 for L1 analysis type. 32
Figure 5-10: Fringing field analysis method 2 for L1 analysis type. 33
Figure 5-11: Single-carrier L1 analysis flow diagram. 34
Figure 5-12: Schematic network used for multipactor analysis. 36
Figure 5-13: Example of multicarrier signal and corresponding pulse approximation. ..37
Figure 5-14: Electron absorption rate for zero applied voltage. 38
Figure 5-15: L1 analysis for multicarrier, Pulsed model flow chart 39
Figure 5-16: 3D view of Ku-band transformer of ESA TRP activity [5-19] 40
Figure 5-17: Pulse amplitude and carrier amplitude vs t_{on}.....41
Figure 5-18: Example with 3 different “on intervals” corresponding to 10%, 30% and 70% of the envelope period together with the theoretical limit (boundary) .42
Figure 5-19: 3D of Ku band bandpass filter of ESA TRP activity [5-19].....43
Figure 5-20: Hybrid L1/L2 multi-carrier analysis steps. 45
Figure 5-21: Electron growth over 10 envelope periods for 10 different “on intervals” for one amplitude factor.....47
Figure 5-22: Convergence of the amplitude factor, showing also how Γ converges towards one electron.....48
Figure 5-23: Hatch and William chart with the multicarrier in-phase amplitude indicated by a green circle. The red dashed line is the fd-product of the average multicarrier frequency and the critical gap size 49
Figure 5-24: KS3 sample geometry. 50
Figure 5-25: KS3 sample simulated RF performance 50
Figure 5-26: 3D view of L-band sample 52
Figure 5-27: Predicted S-parameter Performance of Preliminary L-band RF Device Design.....53
Figure 5-28: Predicted Voltage Distribution in Preliminary L-band RF Device Design..53
Figure 5-29: Predicted S-parameter Performance of Finalised L-band RF Device (1525 MHz) 54

Figure 5-30: Predicted Voltage Distribution in Finalised L-band RF Device (1525 MHz) 54
Figure 5-31: Predicted S-parameter Performance of Finalised L-band RF Device (1405 MHz) 55
Figure 5-32: Predicted Voltage Distribution in Finalised L-band RF Device (1405 MHz) 55
Figure 5-33: Variation of peak voltage on each resonator with frequency – 30 MHz design bandwidth 56
Figure 5-34: Variation of peak voltage on each resonator with frequency – 10 MHz design bandwidth 56
Figure 5-35: Variation of peak voltage on central resonator with bandwidth change (Fc = 1525 MHz) 57
Figure 5-36: RF performances with machining tolerances (Resonant reference sample S-3 and S-4).....58
Figure 5-37: Electric field (12,75 GHz – samples S-3 and S-4).....59
Figure 5-38: Voltage inside critical gap (samples S-3 and S-4).....59
Figure 5-39: Nominal model 60
Figure 5-40: Re-tuned model.....61
Figure 5-41: Return Loss nominal (red) and tuned (pink).....61
Figure 6-1: Work in a clean room environment. 64
Figure 6-2: Screenshot of clean room monitoring. The pressure reading corresponds to the overpressure delta in the clean room.....64
Figure 6-3: A pressure gauge. 65
Figure 6-4: Picture of a typical pressure profile for a P1 component or equipment. 65
Figure 6-5: Picture of a typical pressure profile for a P2/P3 component or equipment with pressure spikes related to outgassing. 66
Figure 6-6: RF cable with thermocouples. 66
Figure 6-7: RF cable with thermocouples. 67
Figure 6-8: A multicarrier test facility.....68
Figure 6-9: Schematic of a three-carrier multipactor test bed.....68
Figure 6-10: Error probability distributions for different $f \cdot d$ 69
Figure 6-11: Error dependency on the similarity degree 70
Figure 6-12: Margin definition with respect pulsed model and CW operation.....71
Figure 6-13: Typical pulse parameters during multipactor test.....73
Figure 6-14: Decay of Strontium-90.....75
Figure 6-15: Picture of an encapsulated radioactive source. 75
Figure 6-16: Sketch of the photoelectric effect.....77
Figure 6-17: Picture of the UV lamp as part of a test bed. 77
Figure 6-18: Spectrum of the typical lamps used for electron seeding. 78
Figure 6-19: Diagram of an electron gun. 79

Figure 6-20: Sketch of the functioning of an electron gun. 79
Figure 6-21: Picture of an electron gun installed into a test bed. 80
Figure 7-1: Schematic of global detection systems implemented in a typical test bed. ..84
Figure 7-2: Electron probe circuit diagram. 86
Figure 8-1: Multipactor test procedure overview. 89
Figure 8-2: Example of an L- and S-band reference sample. 90
Figure 8-3: Measured S-parameter performance of broadband multipactor sample. ...91
Figure 8-4: Ku-band Broadband Multipactor Sample. 91
Figure 8-5: Multipactor threshold variation vs. gap height. 92
Figure 8-6: Ku-band reference sample dimensions. 92
Figure 8-7: Heat pipe. 94
Figure 9-1: Typical dependence of SEY coefficients on primary electron energy. 101
Figure 9-2: Energy distribution curve of emitted electron from gold target surface submitted to 112 eV electron irradiation [9-1] 101
Figure 9-3: Experimental arrangement for SEY test with emission collector 103
Figure 9-4: SEY experimental setup (without collector around the sample) 105
Figure 9-5: Typical composition of exposed to air metal surface 107
Figure 9-6: Measured SEY of metals exposed to air without a specific surface cleaning procedure 108
Figure 9-7: Schematic view of material exposed to atmosphere: the case of silver 109
Figure 9-8: Effect of cleaning of the surface by heating on the SEY of Nb. 110
Figure 9-9: Effect of the water absorption on the SEY. 110
Figure 9-10: Effect of baking on the SEY of dielectrics. 111
Figure 9-11: Evolution of the SEY of the technical silver versus pressure. 112
Figure 9-12: Effect of the temperature on the SEY of silver. Figure extracted from [9-18]. 113
Figure 9-13: Effect of the temperature on the SEY of MgO and BN-SiO2 ceramics. ...114
Figure 9-14: Effect of the temperature on the SEY of coverglass and CVD diamond. 115
Figure 9-15: Effect of the incidence angle variations on the SEY of silver 116
Figure 9-16: Effect of electron irradiation on SEY (CERN) 116
Figure 9-17: Influence of the primary electron energy on the charging process. TEEY = SEY, E_{C1} = E1 and E_{C2}=E2 117
Figure 9-18: Influence of the primary electron energy on the charging process, EEY = SEY, E_{C1} = E1 and E_{C2}=E2 118
Figure 9-19: SEY as a function of the primary electron energy for aluminium 120
Figure 9-20: SEY as a function of the primary electron energy for copper 121
Figure 9-21: SEY as a function of the primary electron energy for gold 121
Figure 9-22: SEY as a function of the primary electron energy for silver coatings 122
Figure 9-23: Comparison of the SEY curves for Cu, Al, Ag and Au 122

Tables

Table 4-1:Multipactor simulations and multipactor measurements with and without thermal baking for a RF component with different dielectric materials 18

Table 5-1: Characteristics Ku-band transformer of ESA TRP activity [5-19].....40

Table 5-2: Characteristics Ku-band transformer of ESA TRP activity [5-19].....43

Table 5-3: Multicarrier signal characteristics.....44

Table 5-4: Predicted and testes multipactor breakdown levels 44

Table 5-5: SEY characteristics of KS3 sample 51

Table 5-6: Multipactor thresholds for KS3 sample 51

Table 5-7: SEY data for L-band sample.....57

Table 5-8: Multipactor thresholds for L-band sample 57

Table 5-9: Multipactor threshold vs. manufacturing errors (samples S-3 and S-4).....60

Table 6-1: Error statistics in dB for silver and aluminium, and different values of carriers, frequency band and fxd product 69

Table 6-2: Rate and energy of injected electrons going through a particular aluminium wall [6-4].....76

Table 8-1: Example of Multipactor Test Specification Sheet 88

Table 8-2: Maximum RF power applied to the load range (margin in bold). 95

Table 8-3: Multipactor test report summary 97

Table 8-4: Test setup validation without sample 98

Table 8-5: Test setup validation with reference sample 98

Table 8-6: Test of DUT at reduced power level at ambient pressure just before closing the vacuum chamber (RECOMMENDED 99

Table 9-1: Average values of the main SEY parameters for all “as built” (mentioned, “Before RF testing” in the below table) and all the “as tested” SEY samples (mentioned, “After RF testing” in the below table) for a given SEY measurement facility 109

Table 9-2: Requirement in the experimental conditions for SEY measurement 119

Table 9-3: SEY parameters of the SEY curves of Al, Cu, Au and Ag samples.....120

Table 9-4: SEY curve data for aluminium 123

Table 9-5: SEY curve data for copper.....127

Table 9-6: SEY curve data for gold.....131

Table 9-7: SEY curve data for silver 135

Change log

ECSS-E-HB-20-01A 15 June 2020	First issue

Introduction

Multipactor is a well-understood RF breakdown mechanism in high vacuum conditions. It has been investigated both theoretically and experimentally over many years, as listed in references from [2-1] to [2-7]. Essential ingredient for multipactor is initial free electrons, also called primary electrons. Free electrons can be accelerated under the action of the high power electromagnetic signals inside the RF component. These accelerated electrons impact the RF internal surface with such a kinetic energy to knock out secondary electrons. This resonant process repeats until an avalanche-like growth of electrons is reached, and a multipactor discharge occurs. A multipactor discharge produces signal noise, power reflection and ultimately a local ionization that leads to a complete short circuit. In the worst case, this can develop to a complete system failure.

A typical multipactor event can be described as follows:

1. Free electrons exist within the RF field region of a component whose dimensions are small compared with the electron mean free path as a result of low pressure within the component.
2. The electric field within the component accelerates the free electrons towards a surface.
3. The electrons impact on the surface with appropriate energies to liberate more secondary electrons than the incident ones.
4. Under the specific condition of synchronism of the RF electric field and the electron impact time, resonance conditions are met and steps b. and c. repeat until multipactor discharge occurrence.

Beside the multipactor discharge, other electrical breakdown of different nature in RF components such as multipactor leading to corona due to local outgassing and discharge occurrence in intermediate pressure range can also arise [2-8], [2-9] and [2-10].

NOTE The Multipactor Handbook follows the same structure as the Standard. Where the WG has decided that the content of a clause of the Standard needs no supporting material this clause is left empty. The text "*No supporting material needed.* " is added there.

1
Scope

This Handbook describes the guidelines and recommendations for the design and test of RF components and equipment to achieve acceptable performance with respect to multipactor-free operation in service in space. This document is the mirror document of the ECSS-ST-20-01 normative document. Thus it includes the same contents as the normative text and has the same structure.

This Handbook is intended to result in the effective design and verification of the multipactor performance of the equipment and consequently in a high confidence in achieving successful product operation.

This Handbook covers multipactor events occurring in all classes of RF satellite components and equipment at all frequency bands of interest. Operation in single carrier CW and pulse modulated mode are included, as well as multi-carrier operations. A detailed chapter on secondary emission yield is also included.

This Handbook does not include breakdown processes caused by collisional processes, such as plasma formation.

2 References

ECSS-S-ST-00-01	ECSS system – Glossary of terms
ECSS-E-ST-10-02	Space engineering – Verification
ECSS-E-ST-10-03	Space engineering - Testing
ECSS-E-ST-20-01	Space engineering – Multipactor design and test
ECSS-M-ST-10	Space project management – Project planning and implementation
ECSS-M-ST-40	Space project management – Configuration and information management
ECSS-Q-ST-20-08	Space product assurance – Storage, handling and transportation of spacecraft hardware
ECSS-Q-ST-70-01	Space product assurance – Cleanliness and contamination control
ECSS-Q-ST-70-02	Space product assurance – Thermal vacuum outgassing test for the screening of space materials
ESCC-20600	Preservation, packaging and despatch of ESCC component
ISO 14644–1:2015	Clean rooms and associated controlled environments – Part 1: Classification of air cleanliness by particle concentration

[2-1] A. Woode & J. Petit, Diagnostic Investigations into the Multipactor Effect, Susceptibility Zone Measurements and Parameters Affecting A Discharge, ESTEC Working Paper 1556, November 1989

[2-2] Abstract Book, Workshop on Multipactor and Passive Intermodulation Products Problems in Spacecraft Antennas, ESTEC, December 1990

[2-3] Final Presentations & Working Meeting: Multipactor & PIM in Space RF Hardware, ESTEC, January 1993

[2-4] A. J. Marrison, R. May, J.D. Sanders, A. D. Dyne, A. D. Rawlins, J. Petit, A study of Multipactor in Multicarrier RF Components, Report no AEA/ TYKB/31761/01/RP/05 Issue 1, January 1997

[2-5] A. J. Hatch and H.B. Williams, J. Appl. Phys. 25, 417 (1954)

[2-6] A. J. Hatch and H.B. Williams, Phys. Rev. 112, 681 (1958)

[2-7] R. Woo, Multipacting Discharges between Coaxial Electrodes, J. Appl. Phys. 39, 1528-1533 (1968)

[2-8] R. Woo, Final Report on RF Voltage Breakdown in Coaxial Transmission Lines, JPL Technical Report 32-1500, October 1970

[2-9] F. Höhn, W. Jacob, R. Beckmann, R. Wilhelm, The Transition of a Multipactor to a low-pressure gas discharge, Phys. Plasma, 4, 940-944 (1997)

[2-10] J. M. Meek and J. D. Craggs, Electrical Breakdown of Gases, Wiley (1978)

3
Terms, definitions and abbreviated terms

3.1 Terms from other documents

a. For the purpose of this standard, the terms and definitions from ECSS-S-ST-00-01 apply, in particular the following terms:
   1. acceptance
   2. bakeout
   3. component
   4. development
   5. equipment
   6. integration
   7. uncertainty
   8. validation
   9. verification

b. For the purpose of this standard, the terms and definitions from ECSS-E-ST-10-02 apply, in particular the following terms:
   1. acceptance stage
   2. analysis
   3. inspection
   4. model philosophy
   5. qualification stage
   6. review of design
   7. test
   8. verification level

c. For the purpose of this standard, the terms and definitions from ECSS-E-ST-10-03 apply, in particular the following terms:
   1. acceptance margin
   2. qualification margin

d. For the purpose of this standard, the terms and definitions from ECSS-Q-ST-70-02 apply, in particular the following terms:
   1. outgassing

3.2 Abbreviated terms

For the purpose of this document, the abbreviated terms from ECSS-S-ST-00-01 and the following apply:

Abbreviation	Meaning
DUT	device under test
EDC	energy distribution curve
EM	electromagnetic
ESD	electron stimulated discharge
FEM	finite element method
HPA	high power amplifier
LNA	low noise amplifier
OMUX	output multiplexer
REG	regulated electron gun
RF	radiofrequency
SEY	secondary emission yield
TVAC	thermal vacuum chamber
UV	ultraviolet

4 Verification

4.1 Verification process

No supporting material needed.

4.2 Multipactor verification plan

No supporting material needed.

4.2.1 Generation and updating

No supporting material needed.

4.2.2 Description

No supporting material needed.

4.3 Power requirements

4.3.1 General power requirements

4.3.1.1 Nominal power

No supporting material needed.

4.3.1.2 Increased power ΔP due to payload mismatch

The increased power ΔP, as a positive value expressed in dB, within the component *i* due to payload mismatch can be derived as follows:

$$\Delta P = 20\log_{10}(1+|\Gamma_{i-1}|)$$

where Γ_{i-1} is the reflection coefficient of the downstream component assembly (also called "component *i-1*" in the Figure 4-1).

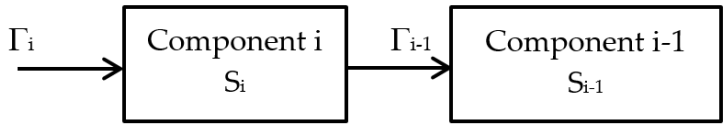


Figure 4-1: Component assembly with consideration of reflection coefficient

Since ΔP is frequency dependent, the worst case ΔP over the operational frequency bandwidth is taken into account.

4.3.1.3 Failure

Failure case for circulators

Circulators are used for protecting high power amplifiers in case of a failure or for improving the RF performance of a network. Therefore, the isolated port has to be matched towards an adequate load. The key feature, the non-reciprocity, of the circulator enables the isolation of the corresponding paths of the system and leads to the mentioned properties.

The next picture shows a typical block diagram of such a circulator with a connected or integrated load. The combination of a circulator with a load is a so-called isolator.

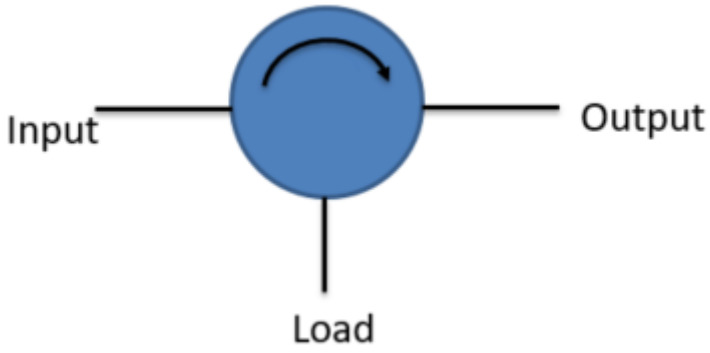


Figure 4-2: Isolator block diagram

To use an isolator for a high power application (peak and average) two failure cases are considered. The first case is the mismatch of the system, which causes additional superposition of the E-Field with respect to the phase. The second case is the total reflection of the signal, e.g. miscommand of a switch, which leads to a standing wave in the circulator. Standing wave condition with respect to worst-case phase produces 2 times the E-field amplitude of the input signal. To prevent an over specification of the isolator the proper application are considered case by case. Therefore, the complete isolator is analysed for multipactor to locate the area where multipactor occurred. This is important for definition of the surface property for the multipactor analysis itself. It is good practise for the margin definition to distinguish between nominal case and the failure case. The margin for the failure case is orientated on the actual application to avoid the situation for over specification, that no isolator design can physically meet.

The impact of the failure case is assessed at system level, taking into account the downstream component assembly.

4.4 Classification of equipment or component type

4.4.1 General classification of equipment or component type

Effect of dielectric charging for P2 components

For RF components with dielectrics, the charging effect adds DC electrostatic fields that can affect the multipactor discharge significantly, depending on the geometry of the device and the applied RF fields. Moreover, the charging properties of dielectrics are extremely sensitive to the dielectric history

(handling, triboelectrification, temperature baking…). Thus, baking can have different effects on the charging behaviour and therefore on the multipactor effect. The initial charge of the dielectric, as well as the induced charge during the multipactor avalanche, are highly unpredictable, which implies a high uncertainty of the multipactor threshold on both analysis and test. The analytical multipactor analysis for the moment do not take into account the charging effect. On the other hand, numerical analysis can model it accurately, although the initial charge of the dielectrics is an input parameter that is usually unknown and is non uniform over the dielectric surface. In most cases, the charging effect implies an increase of the multipactor breakdown [4-1] [4-2] and therefore, analysis with zero charge is usually considered as the worst-case. However, this depends on many parameters and is studied case by case. In addition, the SEY characteristics of the dielectrics can be affected by charging leading to dispersion in the result. This can generate inaccuracy in the analysis (see clause 9). For high power measurements, the dielectric charge is an unknown parameter and can produce significant differences with respect analysis and also between different test campaigns. The Table 4-1 and Figure 4-4 below given by ESA illustrate the discrepancy between multipactor simulations and multipactor measurements for a RF component with different dielectric materials.

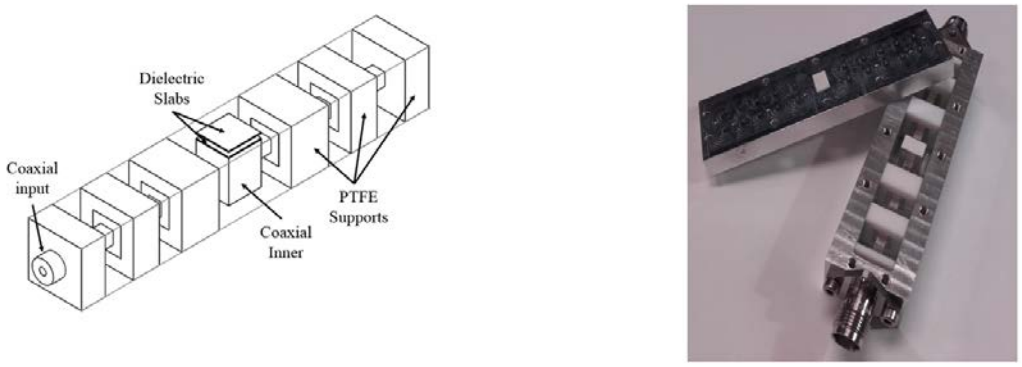


Figure 4-3: Tested component – Coaxial filter

Table 4-1:Multipactor simulations and multipactor measurements with and without thermal baking for a RF component with different dielectric materials

Dielectric	Predicted Worst W/dBm	Predicted Best W/dBm	Delta 0 dB	Baking (80ºC)	Measurements W/dBm	Delta 1 dB	Delta 2 dB
Alumina	143,55/51,57	1023,41/60,1	8,53	NO	426/56,29	4,72	-3,81
				YES	478/ 56,79	5,22	-3,31
Rogers	1984,31/62,98	2296,82/63,61	0,64	NO	818/59,13	-3,85	-4,48
				YES	1020/ 60,08	-2,9	-3,53
Ultem	294,92/54,7	2640,58/64,22	9,52	NO	479/56,8	2,11	-7,42
				YES	563/ 57,50	2,8	-6,72
Rexolite	240,23/53,81	2359,32/63,73	9,92	NO	853/59,31	5,50	-4,42
				YES	602/ 57,79	3,98	-5,94
Teflon	2296,82/63,61	3343,6/65,24	1,63	NO	1070/60,29	-3,32	-4,95
				YES	954/ 59,79	-3,82	-5,45

Delta 0: difference between both simulations which depends on SEY values
Delta 1: difference between worst case simulation and test
Delta 2: difference between best case simulation and test

SEY data used for computing the predicted threshold of Table 4-1 was obtained by different test campaigns.

The worst predicted values of Table 4-1correspond to the Multipactor analysis considering the less conservative SEY figures for each sample.

The best predicted values of Table 4-1 correspond to the Multipactor analysis considering the more conservative SEY figures for each sample.

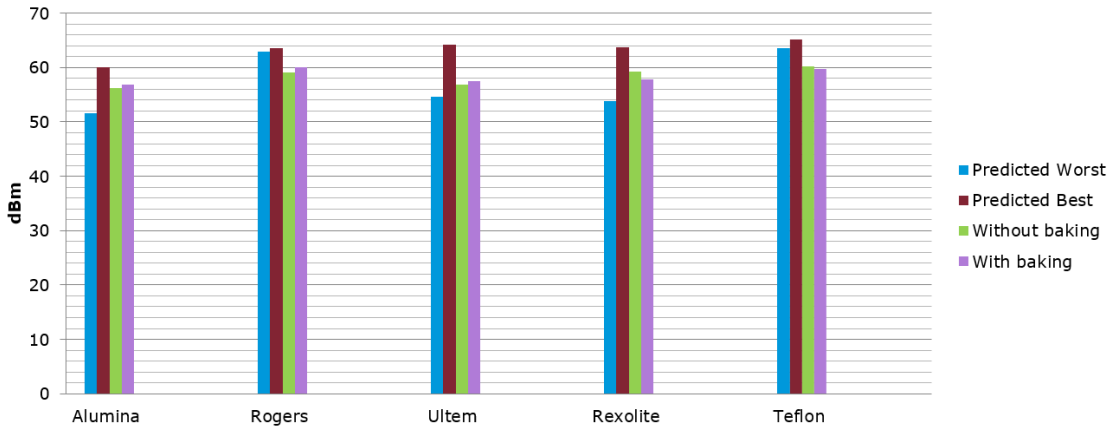


Figure 4-4: Multipactor simulations and multipactor measurements with and without thermal baking for a RF component with different dielectric materials

The discrepancy noticed on the multipactor threshold in the above table can also be explained by other phenomena than multipactor such as corona triggered by local outgassing, or triple point effects.

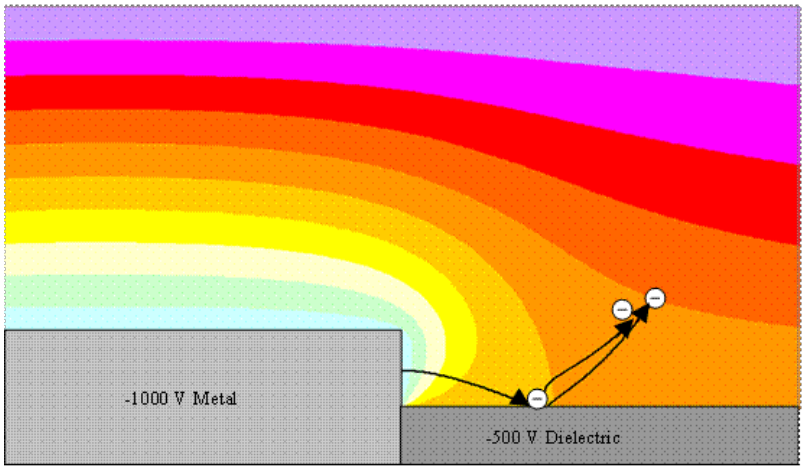
In [4-3], the modelling accuracy for dielectrics with different conductivities was investigated. For dielectrics with relatively high conductivity, a good agreement between the measured and predicted multipactor threshold with 'metal-like' approach was found. A 'metal-like' approach do not take into account the charging properties. For dielectrics with lower conductivity, a large discrepancy between test and prediction was observed.

In order to differentiate between dielectrics showing a high conductivity or not, a charging test can be performed as in [4-4].

Other types of discharge related to P2 and P3 components

In presence of dielectrics inside space RF components (for type 2 and possibly type 3 components), electron stimulated discharge (ESD) phenomena can occur.

These ESD phenomena named "triple point effect" can also occur with RF fields inside RF components with 3 media such as metal, dielectric and vacuum intersecting and with a sharp edge in the metal in an area called "triple point" (see Figure 4-5). When a critical RF field is reached at the level of the metal sharp edge, field emission of electrons can occur. The electron is driven towards the relatively positive dielectric area with energy near the maximum secondary emission yield (see Figure 4-5). If the general configuration of the electric field provides trajectories to infinity, secondary electrons are blown off. For a yield larger than 1, the dielectric region is left more positively charged than before, which increases the DC electric field and field emission capability. So, the process avalanche is only limited by the melting of the sharp edge or tip, when heated by the increasing current density. Then once the melting process is completed, the RF electric field amplitude decreases. Thus the "triple point" phenomenon tends to disappear.



NOTE: Electrons emitted by the metal near the triple point are attracted to the adjacent dielectric. Secondary electrons may be released with yield greater than 1, further increasing the difference in potentials.

Figure 4-5: Schematic diagram of discharge at a triple point in the inverted voltage gradient configuration with potential contours indicated by colour scale.

This phenomenon can be avoided when using rounded metal edge inside the RF component in the "triple point" area.

4.5 Verification routes

4.6 Single carrier

4.6.1 General

No supporting material needed.

4.6.2 Verification by analysis

No supporting material needed.

4.6.3 Verification by test

Influence of the payload mismatch (see 4.6.3.1 b of ECSS-E-ST-20-01)

The test margins assume a nominal return loss of -12dB for the downstream component assembly of the payload. In order to take into account the real mismatch of the downstream component assembly of the payload, a power correction Pc, as an algebraic value expressed in dB, can be applied to the test margin M, by using the following analytical formula:

$$P_c = 20\log_{10}(1 + |\Gamma_{i-1}|) - 1{,}946 \quad [dB] \qquad [4\text{-}1]$$

where Γi-1 is the reflection coefficient of the downstream component assembly (also called "component i-1" in the Figure 4-6 below).

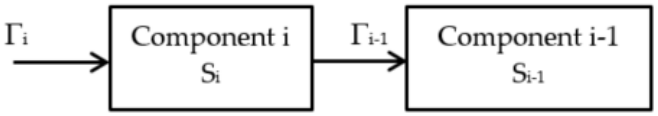


Figure 4-6: Component assembly with consideration of the reflection coefficient of the downstream component assembly for test margin

The corrected margin Mc then becomes:

$$M_c = M + P_c \quad [dB] \qquad [4\text{-}2]$$

The graph as illustrated in Figure 4-7 here below can be utilized to derive the power correction in dB, as a function of the return loss of the downstream component assembly of the payload.

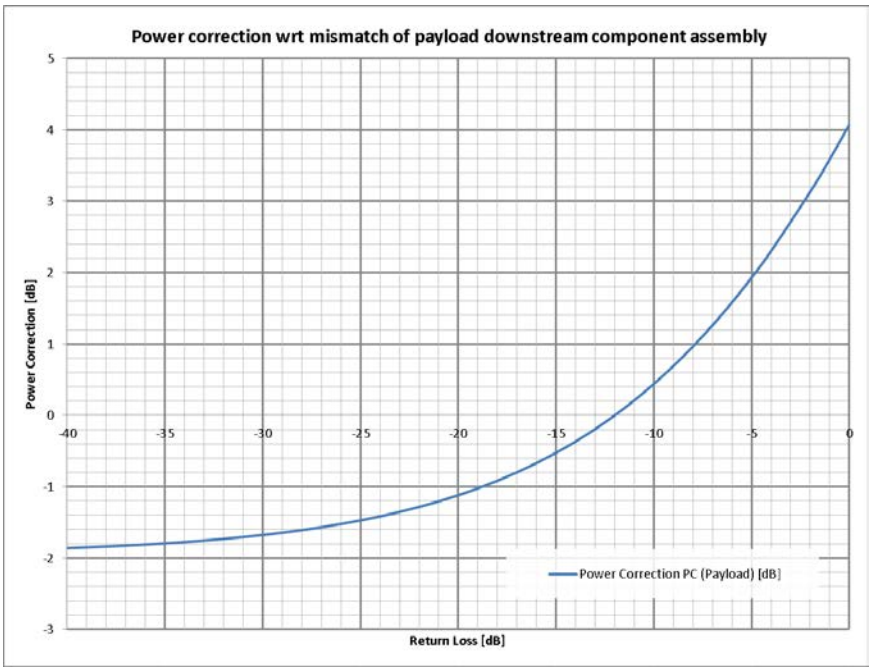


Figure 4-7: Power correction with respect to mismatch of the payload downstream component assembly

Influence of the temperature (see 4.6.3.1d of ECSS-E-ST-20-01)

In order to perform multipactor test for P1 component at ambient temperature with single carrier signal, the following justifications are provided:

- Any parameter concerning the component dimensions' stability versus the temperature (see clause 9.4.1.4),
- The SEY data related to critical gap material versus the temperature (see clause 9.4.1.4),
- Any other parameter affecting the multipactor threshold.

4.7 Multicarrier

4.7.1 General

No supporting material needed.

4.7.2 Verification by analysis

No supporting material needed.

4.7.3 Verification by test

4.7.3.1 Test margins

Margins for multipactor test with multicarrier signal with free running phase (see 4.7.3.1 b of ECSS-E-ST-20-01)

Multipactor test with a multicarrier signal implies specifying the relative phase distribution among the different carriers. Among all possible phase combinations, there is a particular one which yields the lowest breakdown power, which is called worst-case phase distribution. All other distributions will have a higher breakdown power. Since in general the worst-case distribution is unknown, the test is performed with free-running phases, or equivalently, with signal generators with unlocked clocks for each of the carriers. This produces a multipactor signal with phases that shift randomly in time due to thermal drift. Theoretically, if the test is left long enough, the phases would have swept through the possible combination domain in order to cover the worst-case (or close to the worst-case). What part of the domain is covered depends on many parameters, such as the number of carriers, the phase change speed (it is a characteristic of each specific set-up) and the test time. Since the test time is limited, it is impossible to cover the whole domain. Therefore, the potential breakdown threshold will be higher than the real one. This difference, or error, is taken in consideration on top of the official margin and it depends on different parameters of the multipactor discharge, such as fxd, number of carriers, frequency band, frequency spacing, etc. This error is justified case by case. See 6.4.3 for a detailed explanation.

Influence of the temperature see 4.7.3.1 d of ECSS-E-ST-20-01)

In order to perform multipactor test for P1 component at ambient temperature with multicarrier signal, the following justifications are provided:

- Any parameter concerning the component dimensions' stability versus the temperature (see 9.4.1.4),
- The SEY data related to critical gap material versus the temperature (see 9.4.1.4),
- Any other parameter affecting the multipactor threshold.

4.8 Bibliography for clause 4

[4-1] G. Torregrosa, A. Coves, C. P. Vicente, A. M. Perez, B. Gimeno and V. E. Boria, "Time evolution of an electron discharge in a parallel-plate dielectric-loaded waveguide," in IEEE Electron Device Letters, vol. 27, no. 7, pp. 619-621, July 2006.

[4-2] E. Sorolla, M. Belhaj, J. Sombrin, and J. Puech, New multipactor dynamics in presence of dielectrics, Physics of Plasmas 24, 103508 (2017).

[4-3] J. Puech, E. Sorolla, J. Sombrin, M. Belhaj, P. Mader, J. Sinigaglia, “Multipactor effect within RF dielectric components”, Mulcopim 2017.

[4-4] M. Belhaj, “Emission électronique secondaire – R-S13/TC-0007-021”, ONERA report for CNES R&T, November 2013.

5 Design analysis

5.1 Overview

No supporting material needed.

5.2 Field analysis

A multipactor analysis cannot be performed without a good knowledge of the electric fields within the component. Therefore, the first step is to calculate the electrical field within the RF component by using validated EM software or equivalent circuit models considering a perfect match (mismatch is considered in the margin philosophy).

The analysis will allow to identify any region where high voltages and small gaps exist within the equipment. The relevant gap distance is considered at the most critical regions.

In the case of numerical analysis, the convergence of the solution for the S parameter does not necessarily imply a convergence of the RF electric field inside the critical gap which usually needs mesh refinement.

Examples for analytical and numerical multipactor analysis can be found in [5-1] [5-2]. Multipactor analysis with ferrite materials can be found in [5-3] [5-4].

5.3 Multipactor design analysis

5.3.1 Frequency selection

The two key parameters for multipactor, fxd and voltage at the critical gap, vary with the frequency. The higher the frequency the higher the fxd and presumably the higher the multipactor breakdown. But in some cases, higher frequencies can also imply higher fields which can compensate the increase in fxd, producing lower multipactor discharges.

This is why it is recommended to perform a EM field analysis at, at least, three frequency points in the band: centerfrequency and lower and upper edges. This study is done case by case.

5.3.2 Design analysis levels

5.3.2.1 General design analysis requirements

No supporting material needed.

5.3.2.2 Analysis level 1 (L1)

5.3.2.2.1 General requirements for analysist level 1 (L1)

No supporting material needed.

5.3.2.2.2 Criteria for geometry and material

A. Fringing Field Effect

The basic physics involved in the multipactor phenomenon is well known for the case of a homogeneous RF field between two infinite parallel plates. However, most realistic RF device geometries involve inhomogeneous RF electric fields and curved field lines. In such situations, breakdown threshold extrapolations based on the parallel plate results tend to be overly pessimistic and lead to non-optimized designs. An important example of such a situation is waveguides containing irises. The iris is a common waveguide section which is used e.g. for matching purposes. It is also used to couple different electromagnetic modes in different cavities in the filter design. It typically consists of a step like, short length reduction of the waveguide height thus inherently involving an inhomogeneous electric field and curved field lines at the ends of the iris. An estimate for the breakdown threshold based on the voltage over the iris height, assuming homogeneous electric field, does not provide an accurate prediction, in particular for the higher order modes, if the height to width ratio of the iris is large. An approximation can lay on the fact that the RF electric field is homogeneous in the centre of the iris.

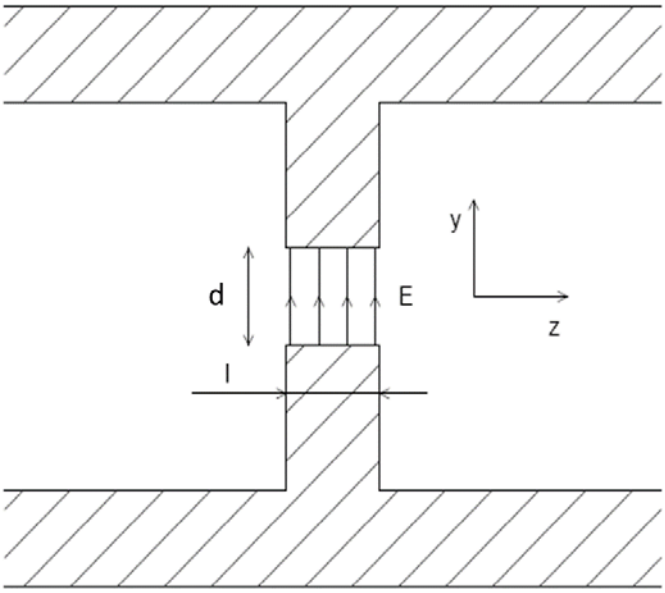


Figure 5-1: 2D schematic of a typical iris-like structure

The existing multipactor theoretical models are only valid when the electric fields inside the structure approach those of a parallel-plate configuration. This is the case of the fields at the center of a rectangular waveguide propagating the fundamental mode when the waveguide height is small compared to its width. However, if geometrical or material discontinuities are present, higher modes are excited (evanescent and/or propagating) and the field lines get curved in the vicinity of such discontinuities. This produces an increase in breakdown power, because of the loss of electrons at the limits of the iris and because of the increase of the effective gap due to the curvature of the field lines. As a consequence, classical multipactor theories cannot be applied in structures with very short irises.

In fact, experimental and numerical results have shown an increase in the breakdown power in irises with respect to the parallel-plate approach. Such works show that the ratio between height and length of the iris (d/l) determines the increase of the breakdown voltage.

Not only irises show this behaviour, also special formed steps or transitions can increase the breakdown power which leads to a higher multipactor threshold.

A.1. Analytical models

Existing theories are only formulated for rectangular waveguide irises in which there is a ratio between height and length of the iris (d/l). These theories model electron losses and derive an effective SEY, which is then used with the classical parallel-plate multipactor theory to compute breakdown.

A.1.1. Electron loss due to lateral diffusion

In [5-5] 2D irises are studied assuming the parallel-plate theory and adding a mechanism of electron loss due to the non-zero tangential velocity of emitted electrons. The displacement of the electrons along the tangential direction of the iris is modelled statistically solving a 1-D Random Walk problem. In order to ignite a multipactor discharge, the rate of production of new secondary electrons is higher than the rate of extinguishing electrons. Therefore, by approximating the rate of electron loss, [5-5] finds the effective secondary emission yield (σ_{eff}) defined as

$$\sigma_{eff} = \gamma_0 \sigma \qquad [5\text{-}1]$$

which is always lower than the nominal SEY (σ) given by the material and the parallel-plate theory. The value of the factor γ_0 is approximated by the diffusion formula

$$\gamma_0 = exp\left(-\frac{\pi^2}{\eta\left(\sqrt{2\pi^3}+2\eta\right)}\right) \qquad [5\text{-}2]$$

where η is in turn

$$\eta = \frac{2l}{v_t d}\frac{fd}{N} \qquad [5\text{-}3]$$

being the average of the tangential secondary emission velocity v_t, l the length of the iris, d the gap size, f the working RF frequency and N the multipactor mode order. Notice that η is directly related to the ratio d/l, in agreement with experimental results.

A.1.2. Electron loss due to fringing fields

The work presented in [5-6] models a 2D capacitive iris and solves analytically the static fields employing the conformal mapping technique. With this method, the electric field can be calculated along the tangential direction of the iris. It is found that the field can be approximated by the parallel plate approximation at the center of the iris, but it starts to deviate at a distance of $l/2+d/2\pi$. Beyond that point, electrons are supposed to be absorbed and, therefore, the iris can be considered to have an effective length of $l_{eff} = l/2+d/2\pi$. By combining this effective length with the effective SEY of Annex A.1.1, it is possible to calculate the multipactor breakdown voltage of an iris employing the analytical parallel-plate approach and considering also lateral random emission velocity and fringing fields.

A.1.3. Application to Sombrin and/or Hatch and Williams charts

Classical Sombrin or Hatch and Williams charts can be computed with the effective SEY derived from the models above, which renders different thresholds for different ratios. A typical chart is shown in Figure 5-2.

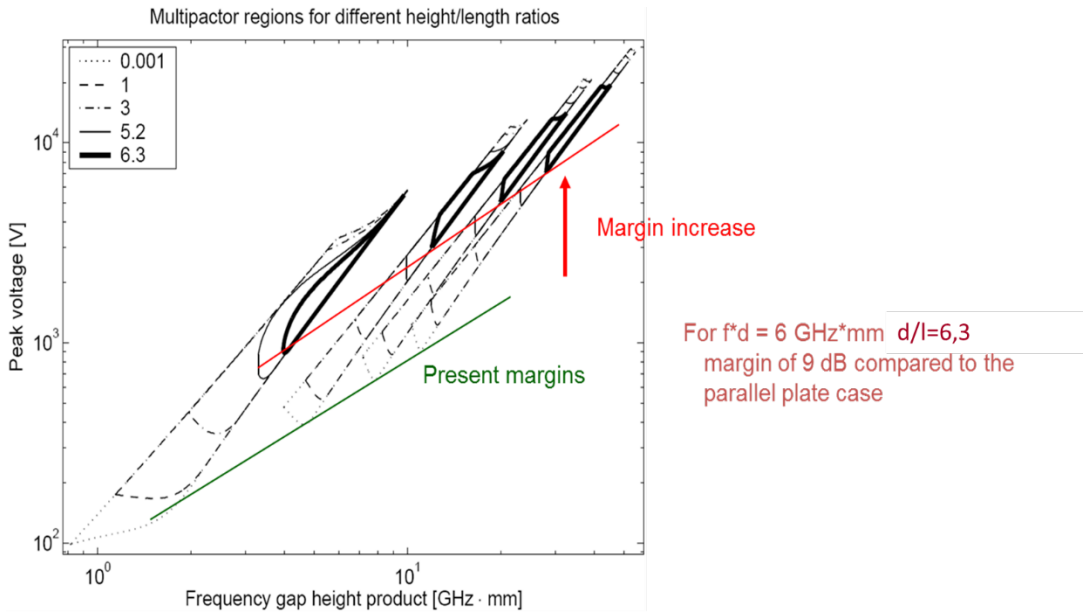


Figure 5-2: 2D Typical Sombrin chart with fringing field effect for different d/l ratios.

In the case of using these classical multipactor theories, the envelop line connecting multipactor order is used instead of the exact multipactor order regions, as shown in the figure above. This is because in classical theories there is a significant gap between orders that can lead to non-conservative predictions

Unfortunately, both Sombrin and Hatch and Williams curves, if not fitted to experimental data, only match accurately the experimental results for the first multipactor order. The rest of them have a shift in voltage. In addition, the resonant conditions yield regions that are too narrow to be able to produce multipactor, even if intercalating even-modes [5-7].

A.1.4. Application to non-stationary theory

The non-stationary theory [5-7] incorporates the randomness of the electron emission velocity and is able to accurately reproduce multipactor breakdown level for all multipactor orders. Arbitrary SEY curves can be used. Multipactor regions using the effective SEY coming from sections above can be computed. Figure 5-3 shows an example.

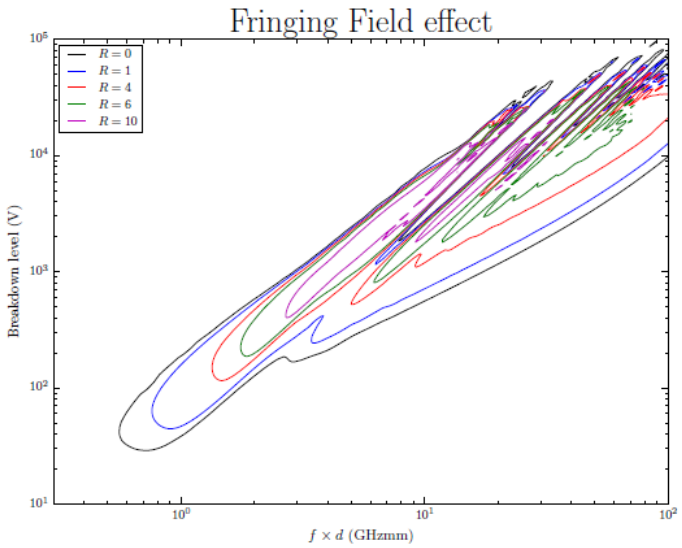


Figure 5-3: 2D Typical multipactor chart computed with non-stationary theory with fringing field effect for different d/l ratios.

A.2. Numerical computation

3D numerical RF electromagnetic software, with added capability to simulate particle trajectories through electromagnetic fields, computes the fields within a microwave structure and automatically incorporates the fringing field effect. This constitutes a reasonably accurate method to predict the multipactor discharge in these cases.

A.3. Experimental test campaigns and comparison with numerical and theoretical methods

Four test campaigns are compared here. NASA report [5-8], results from TAS-CNES studies [5-9] activity, results from ESA-TESAT activity [5-10] and results from ESA-AURORASAT activity [5-11] and results from the EVEREST activity [5-12].

During the EVEREST activities, comparisons were performed between measurements and numerical means on RF equipment's with an RF structure. The validated software were the following ones:

- FEST3D/SPARK3D (Aurorasat)
- CST Particle Studio (CST)
- Conformal mapping software (IAP, Chalmers University, CNES)

In the context of the EVEREST project, the Figure 5-4 shows the comparison between the numerical results coming from the conformal mapping approach using ONERA SEY data and the EVEREST test campaign results [5-12]. The RF component used was a coaxial filter with fringing field geometry.

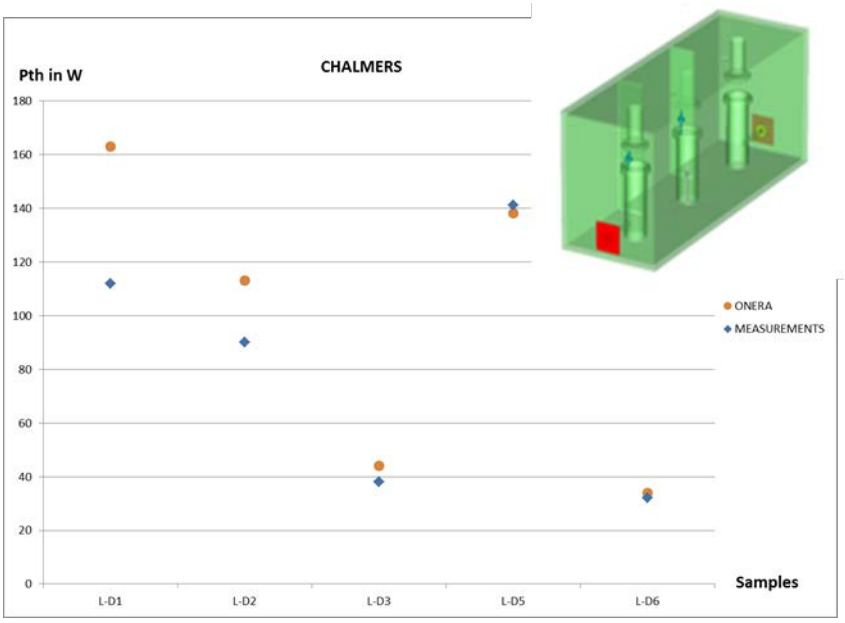


Figure 5-4: 2D Experimental results corresponding to EVEREST project [5-12]

Experimental results of the ESA-TESAT activity [5-10], show the voltage increase factor (breakdown voltage compared to parallel-plates one) of the activity compared to the NASA report. It can be seen that the NASA curve increases rapidly for large height/thickness ratio. ESA-TESAT measurements show lower increase factors and present multipactor discharges for values beyond the NASA limit (1.4).

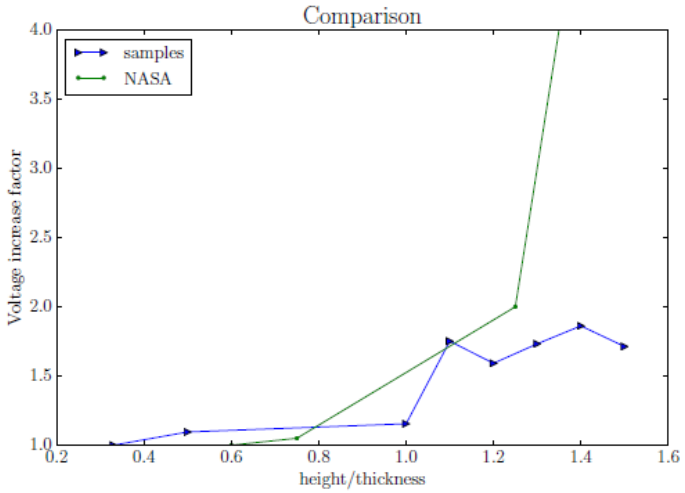


Figure 5-5: 2D Experimental results corresponding to ESA-TESAT activity [5-10]

The three plots in Figure 5-6, Figure 5-7 and Figure 5-8, correspond to the experimental, numerical and analytical results of the ESA-AURORASAT activity [5-11], respectively, which also agree with ESA-TESAT activity. Lower voltage increase factors with respect to the NASA report are obtained. Multipactor has been found (for measurements, numerical and analytical analysis) for ratios beyond 1.4 and even up to a ratio of 6.

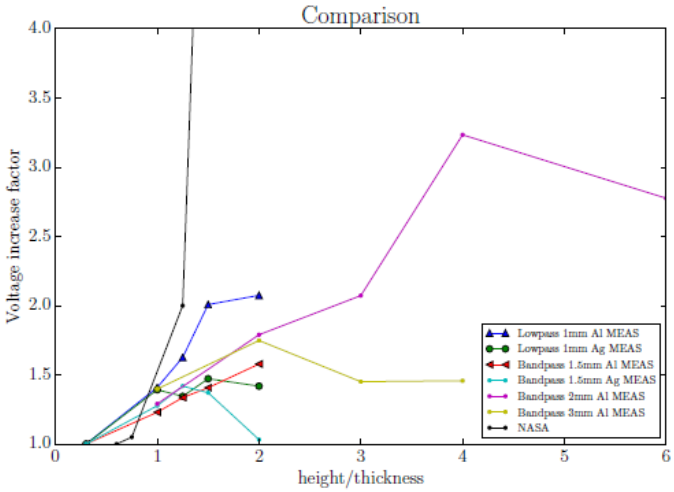


Figure 5-6: 2D Experimental results corresponding to ESA-AURORASAT activity [5-11]

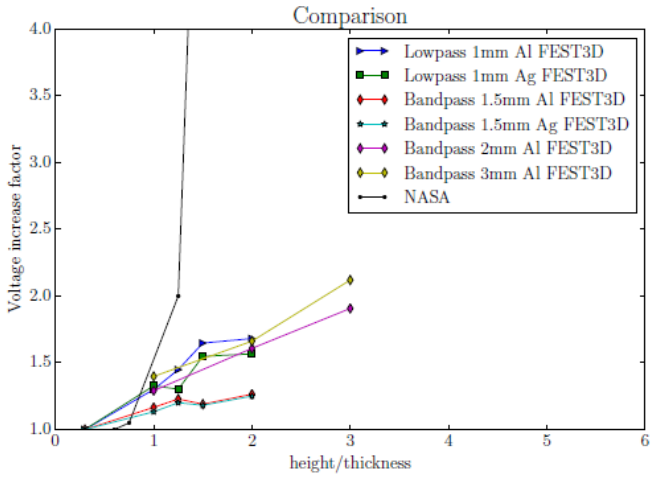


Figure 5-7: 2D Numerical results corresponding to ESA-AURORASAT activity [5-11]

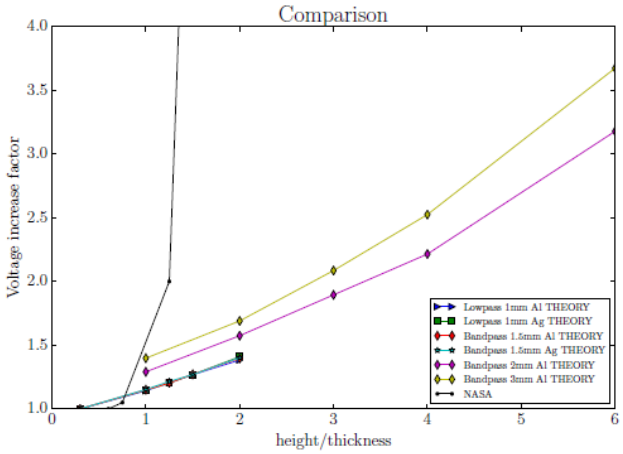


Figure 5-8: 2D Analytical results corresponding to ESA-AURORASAT activity [5-11]

The conclusion is that the curves highly depend on the geometry of the component and the SEY properties, and therefore the increase ratio is obtained case by case.

A.4. Conclusions

With regard to the prediction, there are four possible ways of prediction

A.4.1. Fringing field analysis based on level 1 analysis level

Method 1: Use L1 analysis for parallel plate and a fitting function (exponential, parabolic, polynomial) adjustment based on the length/height ratio for a given fxd product. This fitting function comes from measurements, at a specific fxd product, for a specific topology and coating material, which has to be representative of the analysed component. A margin can be applied to this fitting function to ensure conservativeness. The validity of the selected fitting function is justified case by case.

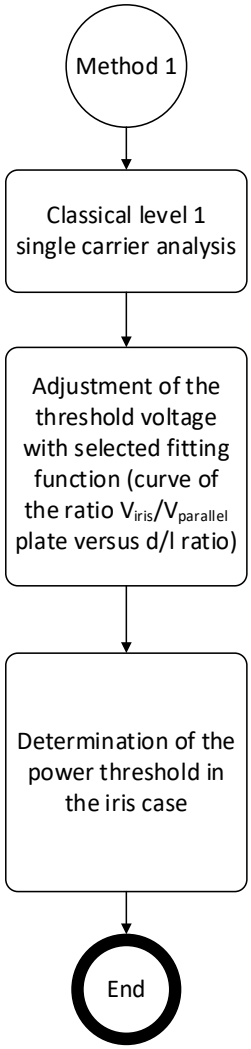


Figure 5-9: Fringing field analysis method 1 for L1 analysis type.

Method 2: Based on the theoretical aspects of the section A.1, 2 possibilities are offered:

a) Use any L1 analysis method with the effective SEY coming from electron losses models of section A.1. The multipactor charts can be computed accordingly with the height over width ratio (d/l) as parameter. For a given fxd product and a given d/l ratio, the threshold voltage will be determined at the lowest order.

b) Another possibility is to use the L1 analysis method with the effective SEY coming from electron losses models of section A.1 and apply the boundary function as in the section A.1.3. For a given fxd product and a given d/l ratio, the multipactor breakdown level will be determined by the corresponding value on the envelope.

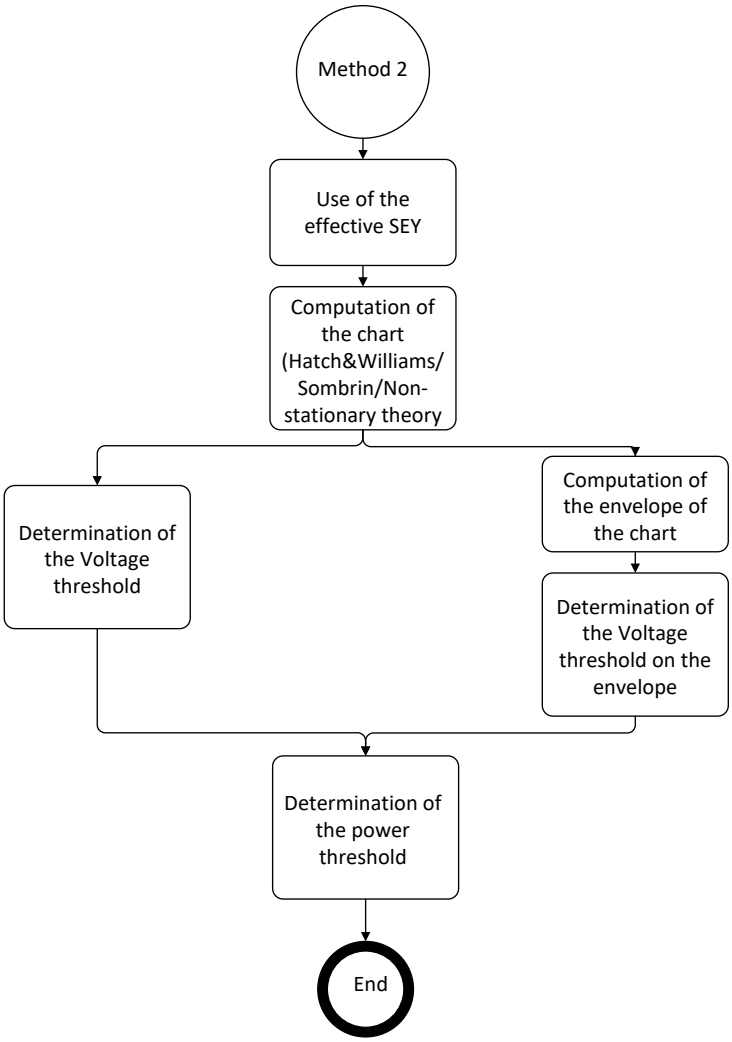


Figure 5-10: Fringing field analysis method 2 for L1 analysis type.

A.4.2. Fringing field analysis based on level 2 analysis level

Method 3: Use numerical methods based on level 2 analysis level.

Numerical software (method 3) is the most reliable prediction method and it is strongly recommended for irises and other complex geometries

5.3.2.2.3 Analysis methodology for single-carrier case

The level 1 analysis is based on analytical analysis or numerical 1D simulation of multipactor in infinite parallel-plate/coaxial geometry.

With respect to the theoretical analysis, it is based either on direct analysis, or the use of Multipactor charts, computed through multipactor analytical methods:

- The non-stationary (statistical) theory [5-13].
- Classical Hatch&Williams or Sombrin theory. Note that both Hatch&Williams and Sombrin charts are shifted towards lower breakdown threshold, for multipactor mode orders higher than

one. Such a shift is due to the simple assumption of deterministic emission velocity [5-7], and implies a systematic extra conservative margin. In those cases, it is typical to add some fitting parameters to the higher orders to make them match with experiments.

In order to obtain the Multipactor threshold voltage, fxd product of the DUT is known. The flow diagram for L1 analysis is depicted in Figure 5-11.

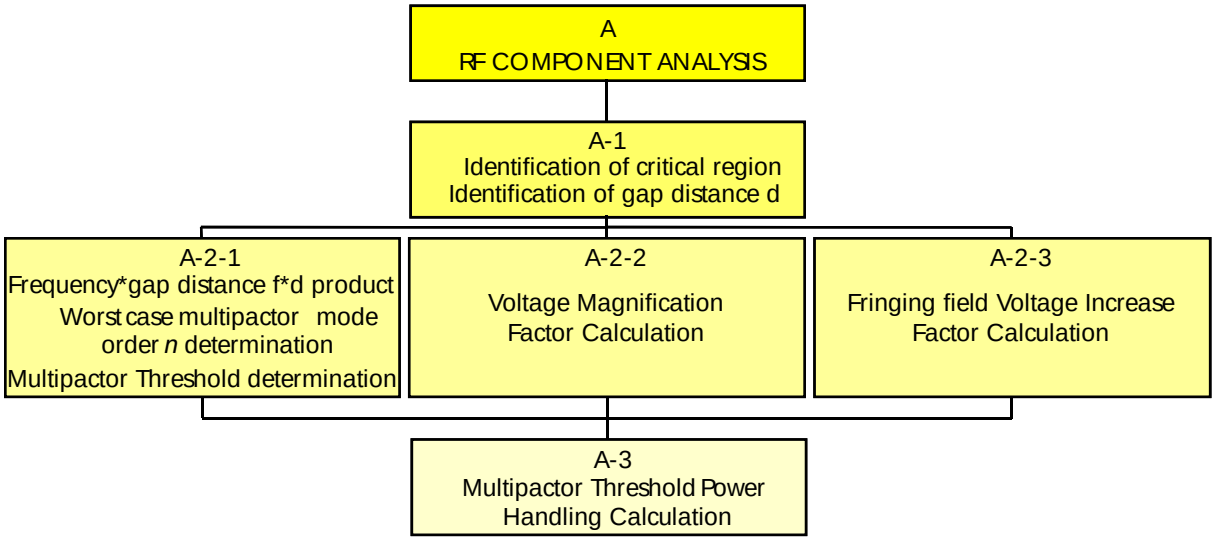


Figure 5-11: Single-carrier L1 analysis flow diagram.

A-1: Identification of critical multipactor region:

The component is analysed in terms of electromagnetic fields. Once the fields are obtained, the component is inspected finding the regions in which the combination of gap and fields potentially yield the lowest breakdown. As a rule of thumb, small gaps with high electric fields are potentially more dangerous. If more than one area is identified as having risk of discharge, multipactor analysis is done for all of them.

A-2.1: Multipactor voltage threshold determination:

For each gap, the fxd product is obtained and L1 analysis can be performed. The output is the threshold multipactor voltage at the critical gap.

A-2-2: Voltage to power conversion:

Once the voltage at the critical gap is obtained, it is necessary to convert it to the corresponding input power threshold.

In order to do so, the steps are:

Assuming an input power of P_{IN} and the corresponding electric field $\vec{E}(x)$, compute voltage V_{max} along the gap distance d as follows

$$V_{\max} = \int_0^d \vec{E}(x) \cdot \vec{t}(x)\, dx \qquad [5\text{-}4]$$

where $\vec{t}(x)$ is the tangential vector at point x. Practically, the gap is discretized in regular steps and the tangential component of the field is summed along the gap distance. If the electrical field is nearly constant, the voltage can be approximated by:

$$V_{\max} = d \cdot \left(\max_{x} \vec{E}(x) \cdot \vec{t}(x) \right) \quad [5\text{-}5]$$

The input power can be computed by either (a) or (b) shown below:

(a) Computing the voltage to power ratio.

If the electromagnetic fields, and hence V_{max}, have been obtained with an input power of Pin. The power ratio is equal to the squared voltage ratio between the breakdown voltage V_T and V_{max} as:

$$\frac{P_{T,IN}}{P_{IN}} = \left(\frac{V_T}{V_{\max}} \right)^2 \quad [5\text{-}6]$$

And therefore the breakdown power $P_{T,IN}$ is

$$P_{T,IN} = kV_T^{\,2} \quad [5\text{-}7]$$

where *k* is the voltage to power ratio defined as

$$k = \frac{P_{IN}}{(V_{\max})^2} \quad [5\text{-}8]$$

Note that if the input power Pin is equal to 1W, the above equation can be written as:

$$P_{T,IN} = \left(\frac{V_T}{V_{\max}} \right)^2 \quad [5\text{-}9]$$

In this case V_{max} as usually referred as "voltage at 1W" or $V_{@1w}$.

(b) Computing Voltage magnification factor as follows

Compute the input voltage V_{in} with similar procedure as V_{max}. Then, the Voltage magnification factor α is defined as follows:

$$\alpha(f) = \frac{V_{\max}(f)}{V_{in}(f)} \quad [5\text{-}10]$$

With the voltage magnification factor, the multipactor threshold $P_{T,IN}$ in the gap can be reported at the input port to determine the multipactor threshold power handling:

$$P_{T-IN} = \left(\frac{1}{\alpha} \right)^2 \cdot \frac{V_T^2}{2Z_0} \quad [5\text{-}11]$$

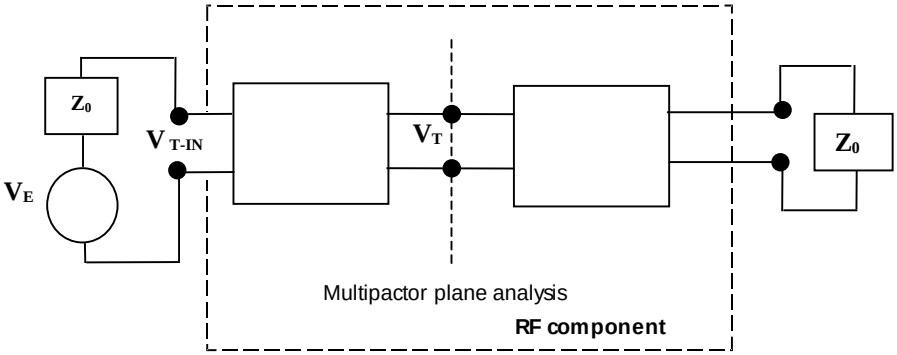


Figure 5-12: Schematic network used for multipactor analysis.

Z_0 is the characteristic impedance at RF component input port at the lowest frequency. For a rectangular waveguide:

$$Z_0 = \frac{2b}{a}\frac{120\pi\lambda_g}{\lambda_0} \qquad [5\text{-}12]$$

where λ_0 and λ_g are calculated for *f*, *a* and *b* are the dimensions of the waveguide at the input port.

A-2-3: Fringing field increase factor:

If applicable, a voltage increase factor due to fringing fields β can be applied. See Section 5.3.2.2.2.

$$P_{T,IN,F} = (\beta)^2 P_{T,IN} \qquad [5\text{-}13]$$

Where $P_{T,IN,F}$ is the input threshold power considering fringing fields correction.

5.3.2.2.4 Analysis methodology for multi-carrier case

B.1 Pulsed Model

B.1.a The pulsed model follows the "long-term multipactor" model as published in [5-14]. It approximates the multicarrier signal as single carrier signal with a frequency equal to the mean frequency of the carriers and a pulsed envelope with two intervals "on" and "off".

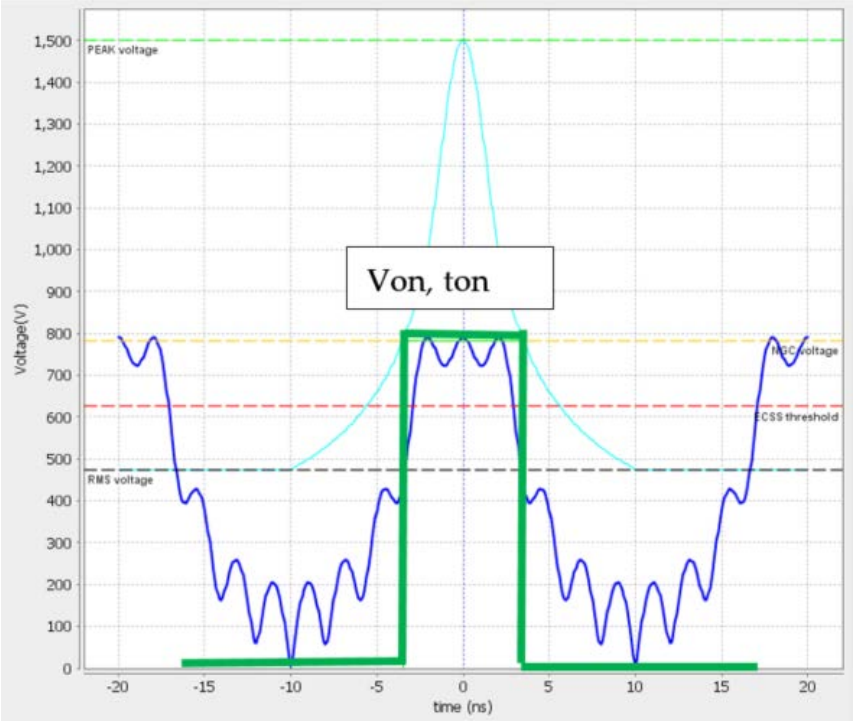


Figure 5-13: Example of multicarrier signal and corresponding pulse approximation.

B.1.b Since the amplitude V_{on} is constant during the t_{on} interval and the amplitude is zero during the t_{off} interval, the electron growth Γ_{ON} and absorption Γ_{OFF} can be analytically modelled with the classical single-carrier theory [5-14].

The long-term multipactor establishes that in order to produce a discharge the electron growth is higher than the electron absorption during a multicarrier signal envelope period. Therefore, the threshold for multipactor occurrence is

$$\Gamma_{ON}\Gamma_{OFF} = 1 \qquad [5\text{-}14]$$

The electron production factor is

$$\Gamma_{ON} = \sigma^{\frac{2f}{n}t_{on}} \qquad [5\text{-}15]$$

Where, σ is the SEY of the impacting electrons during resonance, n is the multipactor order and f is the frequency of the signal.

The absorption factor is [5-14]

$$\Gamma_{OFF} = exp\left(\frac{\pi}{2}\frac{\sigma_0 - 1}{\frac{d}{v_e} + \alpha t_{off}}t_{off}\right) \qquad [5\text{-}16]$$

where σ_0 is the SEY of the electron impacting at very low energies (since the field is zero electrons do not accelerate and impact with same emission energy which is typically around few electron volts), d is the gap size and v_e is the average electron emission velocity. Factor α models linear saturation of the electron absorption rate, as described in [5-15]. It can be numerically found to fit electron absorption with zero applied field. A reasonable value is

$$\alpha = 0{,}12(1 - \sigma_0) \qquad [5\text{-}17]$$

Figure below shows the motivation of introducing the α factor (Linear Saturation Model). When no field is applied the electrons impact with the opposite plate thanks to their initial velocity. Since it is a random process, high energetic electrons have a higher impact rate and are absorbed more quickly. Low energetic electrons have lower impact rates. This is the reason why after a certain time the absorption tends to stabilize with a non-exponential behaviour.

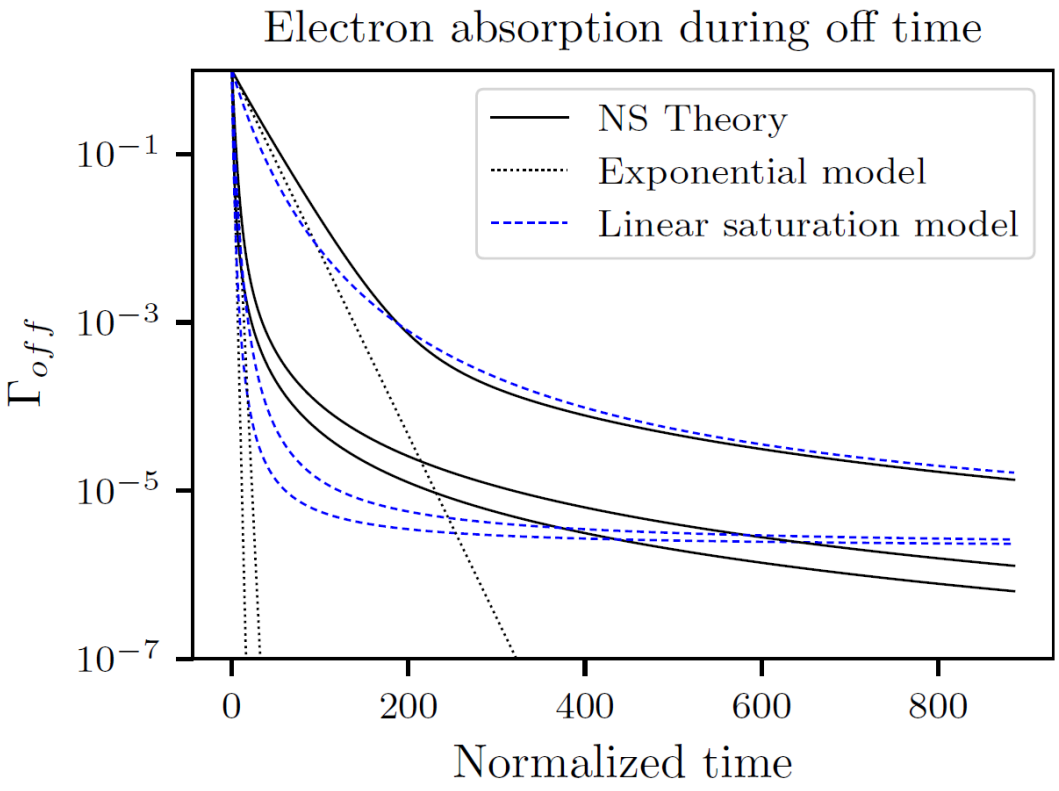


Figure 5-14: Electron absorption rate for zero applied voltage.

From these equations, and keeping in mind that $t_{on} + t_{off} = T_e$ (period of the envelope), we can work out the t_{on} interval as

$$\mathrm{t}_{on} = \frac{AB - C - \sqrt{(AB - C)^2 + 4AC\alpha T_e}}{2A\alpha} \qquad [5\text{-}18]$$

where

$$\mathrm{A} = \frac{2f}{n}\log(\sigma) \qquad [5\text{-}19]$$

[5-20]

$$B = \frac{\mathrm{d}}{\mathrm{v_e}} + \alpha T_e$$

$$\mathrm{C} = \frac{\pi}{2}(\sigma_0 - 1) \qquad [5\text{-}21]$$

All the parameters of the equations above are known except for the multipactor order, n, and the SEY at resonance, σ. Given a fxd product and an applied voltage V_{on}, these can be easily derived from classical multipactor theory [5-15].

b.1.c The above equation gives the relationship between V_{on} and t_{on}. Now it is necessary to derive the equivalent amplitude per carrier, V_c, of the multicarrier signal. In order to do so, there are mathematical approximations which give V_c in terms of V_{on} and t_{on}, and number of carriers N, like Wolk's curve [5-16], or Angevain's curve [5-17][5-18]. Both are equivalent, but Angevain's curve gives an approximation which is more general and valid for more situations than Wolk's.

Therefore, we now obtain the curve $V_c = f(t_{on})$. The worst-case voltage is the minimum of that function that will happen at a certain value of t_{on}.

To sum up, the pulsed model is generalization of the X-gap-crossing rule but instead of assuming X=20 for all cases, searches the right t_{on} which ensures the lowest breakdown voltage.

The whole procedure can be summarized as follows in Figure 5-15.

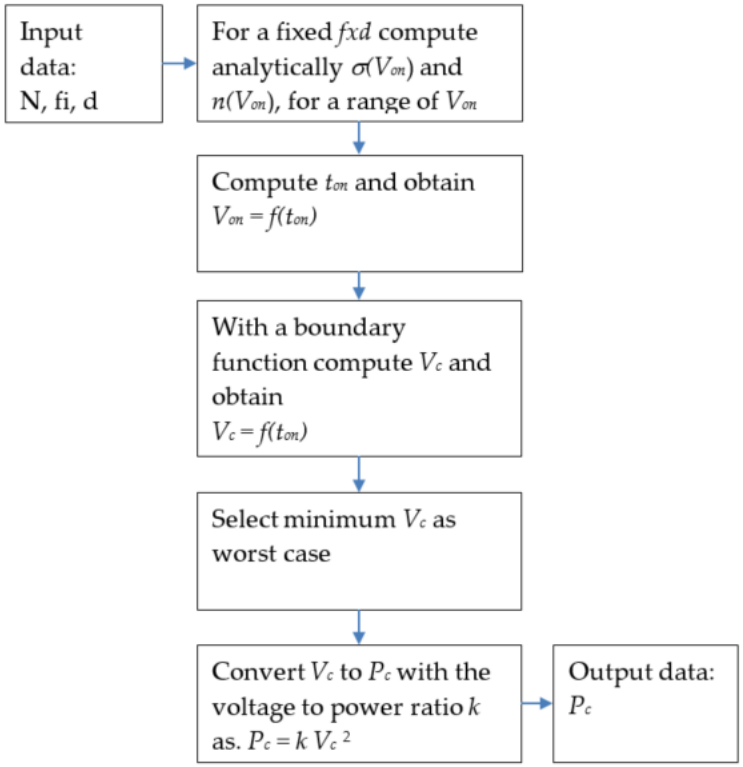


Figure 5-15: L1 analysis for multicarrier, Pulsed model flow chart

Example: Pulsed model prediction for a Ku-band transformer:

The Ku-band transformer of Figure 5-16, has been built and tested in the framework of an ESA TRP activity [5-19].

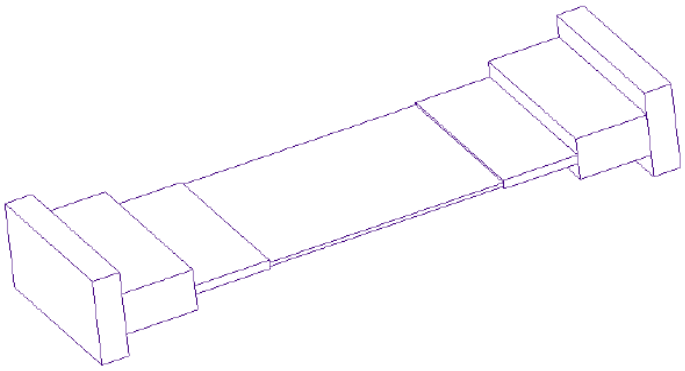


Figure 5-16: 3D view of Ku-band transformer of ESA TRP activity [5-19]

The transformer characteristics are given in Table 5-1.

Table 5-1: Characteristics Ku-band transformer of ESA TRP activity [5-19]

Gap (mm)	V@1W	Carriers	Freq (GHz)	fxd (GHz mm)	Order	Spacing (MHz)
0,42	8,88	6	11,9920	7,6749	3	38,3

The following parameters have been chosen for the pulse model method:

- SEY model: Modified Vaughan's curve [5-7]
- Silver plating with parameters, E_1 = 30 eV, E_{max} = 165 eV, SEY_{max} = 2,22, SEY0 = 0.5
- Electron emission energy 1.5 eV
- Boundary function: Angevain's modified sincsum [5-18]

The equation used to derive the boundary function is [5-18]

$$F_V(\tau) = \frac{\sqrt{\sum_{k=1}^{N} P_k + 2\sum_{k=1}^{N-1}\sum_{i=k+1}^{N}\sqrt{P_k P_i}\,\frac{\sin(\pi(f_k - f_i)\tau)}{\pi(f_k - f_i)\tau}}}{\frac{1}{N}\sum_{k=1}^{N}\sqrt{P_k}} \qquad [5\text{-}22]$$

Following the procedure described in Figure 5-15, the plots for $V_{on} = f(t_{on})$ and $V_c = f(t_{on})$ are obtained and shown in Figure 5-17.

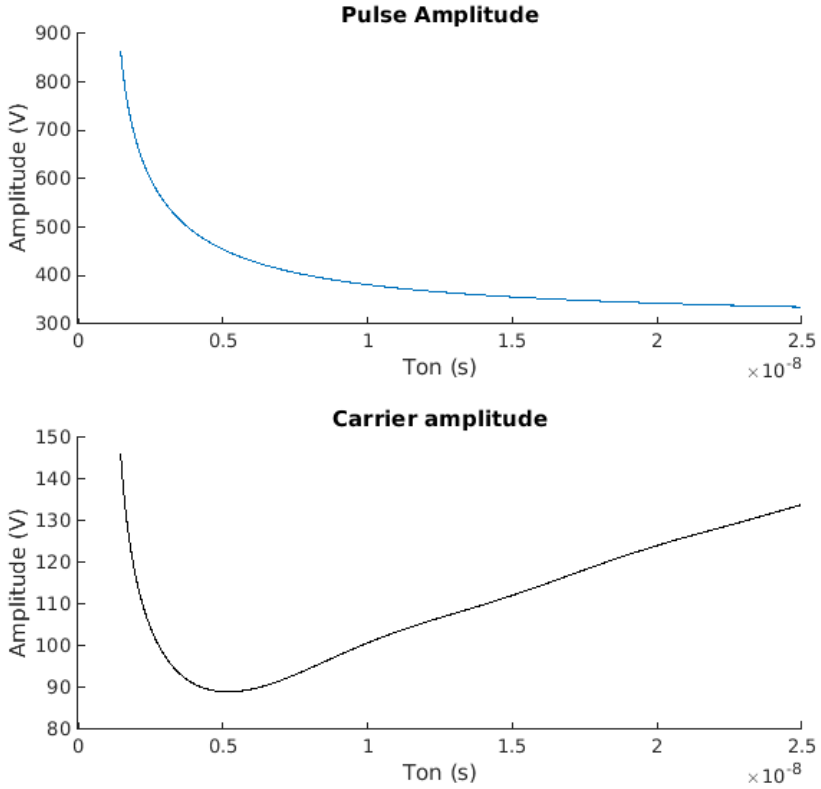


Figure 5-17: Pulse amplitude and carrier amplitude vs t_{on}

The minimum Voltage per carrier is of 89 V/carrier at a ton of 5.3 ns. Translated to power, this is a prediction of 100 W/carrier. The experimental result was 201 W/carrier. Therefore, the prediction is conservative with a margin of 3 dB.

The threshold computed with the 20-gap-crossing rule, following the preceding standard, is 45 W, which implies a margin of 6.5 dB.

It is important to remind that the outcome of the pulsed method is very dependent on the theory and parameters chosen. This requires justification and agreement with the customer.

B.2 Envelope sweep approach

The envelope sweep approach considers the full multicarrier signal without any simplification. This is, the envelope of the multicarrier signal is determined by the frequencies and the relative phases of the carriers.

In principle, the only way to ensure that the worst-case phase combination is found is by searching the minimum breakdown power within the whole domain of phase combinations. The complexity of the problem scales with (O^N). Analytical solutions, such as the non-stationary theory [5-7], the quasi-stationary theory [5-15] and similar ones [5-21], are less costly in terms of computational resources, and would allow for global optimization in the whole phase range for some simple cases. For numerical simulations, the problem is, by the time of speaking, completely unaffordable.

The envelope sweep proposes a reduction of the phase domain, based in the fact that what really affects the multipactor discharge is the envelope shape, regardless the phase combination. In other words, many different phase combinations that yields similar envelope shape will have similar breakdown

level. In addition, it has been seen that the envelope shape does not have significant changes for phase variations around +- 5 degrees.

Conceptually, the envelope sweep defines an envelope shape by the duration of the "on interval", ton, or the interval in which the envelope signal is above the threshold level. Then, a sweep of such duration is done for a certain number of points, and the phases are optimized in order to obtain the ton for each of the points. With those phases the breakdown power is obtained using any full multicarrier method, being analytical or numerical. Finally, the lowest threshold is selected.

More specifically, the envelope sweep method determines the worst case phase law for a large number of "on intervals", t_{on}, of the envelope period, e.g. 10%, 20%...100% of the envelope period, T_e. A common approach applied when finding these phases for each "on interval" is to use an optimization or genetic algorithm, which searches for the phases that will collect as much power as possible within the t_{on} time.

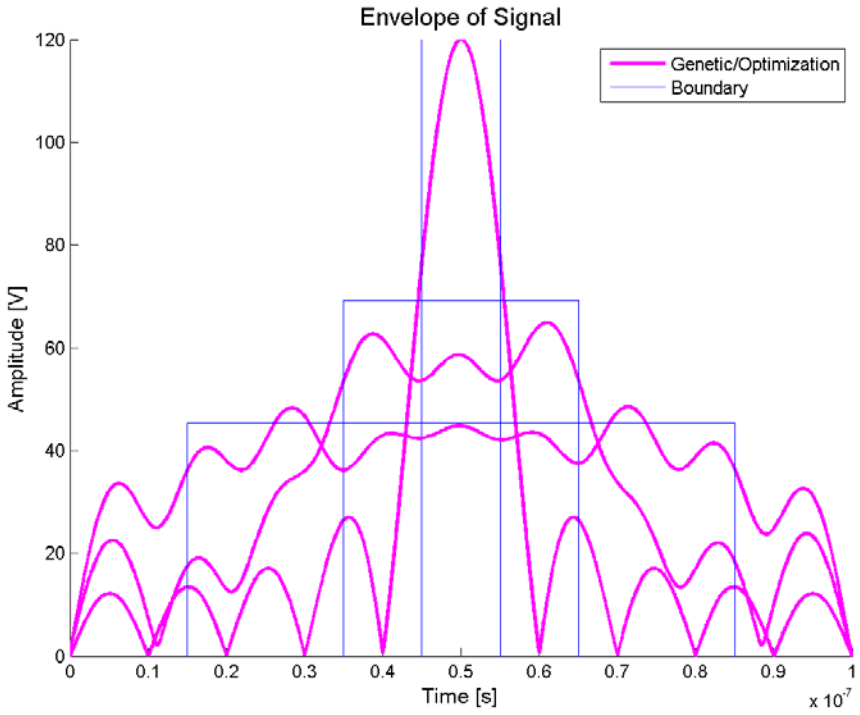


Figure 5-18: Example with 3 different "on intervals" corresponding to 10%, 30% and 70% of the envelope period together with the theoretical limit (boundary)

The relative amplitude between carriers is fixed and the amplitude of the envelope signal can be varied by a simple factor, "the amplitude factor", A_V. By starting with carriers with amplitude Ei, the envelope amplitude can be varied by multiplying each carrier with A_V, where $A_V = 1$ gives the start amplitudes and $A_V < 1$ reduces the envelope amplitude whereas $A_V > 1$ increases it. The total field can be written:

$$E(t) = A_V \sum_{i=1}^{N} E_i \sin(\omega_i t + \varphi_i) \qquad [5\text{-}23]$$

The precision of this method relies on the number of points of the sweep. There is also an error coming from the reduction of the phase domain, which according to latest studies, is well within the analysis margins.

See example given in 5.3.2.3.3.

5.3.2.3 Analysis level 2 (L2)

5.3.2.3.1 Criteria for geometry and material

No supporting material needed.

5.3.2.3.2 Analysis methodology for single-carrier case

See Reference [5-2].

5.3.2.3.3 Analysis methodology for multi-carrier case

Envelope sweep

See section 5.3.2.2.4 for a detailed explanation of the method.

Example: Envelope sweep with Ku bandpass filter

The sample of Figure 5-19: was designed, manufactured and tested in the framework of an ESA TRP activity [5-19].

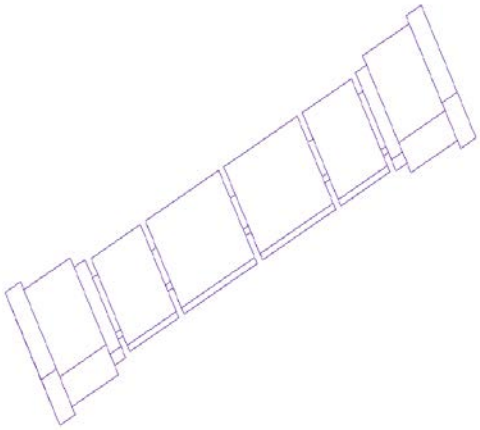


Figure 5-19: 3D of Ku band bandpass filter of ESA TRP activity [5-19]

Its characteristics are summarized in Table 5-2:

Table 5-2: Characteristics Ku-band transformer of ESA TRP activity [5-19]

Gap (mm)	**V@1W**	**Center frequency** (GHz)	**Fxd** (GHz mm)	**Multipactor order**
1,31	32,1	11,99	15,71	7

A multi-carrier case with 8 carriers, with 38,3 MHz spacing, was considered as Table 5-3

Table 5-3: Multicarrier signal characteristics

Carrier	1	2	3	4	5	6	7	8
Freq. (GHz)	11,8600	11,8983	11,9366	11,9749	12,0132	12,0515	12,0898	12,1281

Different analysis methodologies were performed such as:

- The 20 gap crossing rule of the preceding standard [5-22].
- The envelope sweep, with the non-stationary theory [5-7].
- The envelope sweep, with a numerical software (Full 3D EM solver) [5-2].
- The global optimization of the worst case phase with the non-stationary theory [5-13].

They were compared with the test, employing free-running phases. The results are summed up in Table 5-4:

Table 5-4: Predicted and testes multipactor breakdown levels

	Breakdown power per carrier (W)	Margin (dB)
20GCR	76	4,9
Optim NS	121	2,9
ES NS Theo.	123	2,8
ES FEST3D	181	1,1
Test	234	
ES = envelope sweep NS = non-stationary theory 20GCR = 20-gap-crossing rule		

The envelope sweep with non-stationary theory has obtained a breakdown which is almost equal to the global optimization with the non-stationary theory. The latter provides the worst-case for a parallel-plate geometry. Therefore, these results show that, in this case, the envelope sweep has obtained a result which is very close to the worst-case one. The margin of almost 3 dB with the test results comes from the inherent conservativeness of the parallel plate approach which can also be seen in single-carrier.

The best results are obtained with the envelope sweep combined with the numerical software, which is able to model accurately the 3D fields and trajectories of the electrons inside the device.

The 20 gap crossing rule obtains in this case the most conservative result with almost 5 dB margin. The Envelope sweep shows a better performance yet being still conservative.

Hybrid L1/L2 multi-carrier analysis

This method is proposed as an alternative for the full multicarrier analysis proposed above.

A 3D multipactor software is a general tool for assessment of the multipactor threshold for most microwave devices, which cannot be simplified in such a way that a parallel plate model is a useful approximation of the device from a multipactor point of view. Among the drawbacks of the 3D software

is the time of computation to determine a reliable and accurate threshold. The time needed depends among other things on the electrical size and complexity of the device. For a single carrier scenario, the time required is often tolerable, but when going to the multicarrier scenario, the computation time can increase many times, as each "envelope sweep" is analyzed separately.

In cases when the time of computation becomes intolerably long or the 3D software does not support multicarrier multipactor analysis, the method described in this chapter can be an alternative.

The basic idea of this method is that the 3D-problem and multicarrier analysis are separated. The geometrical aspects are managed using a single carrier 3D multipactor software and the multicarrier complication is solved as a parallel plate problem. The results are then combined to yield a 3D multicarrier multipactor solution.

Justification of the method is that the multicarrier signal behaves much like a single carrier signal with a frequency corresponding to the average frequency of all the carriers, but with varying amplitude.

When analyzing multicarrier multipactor over many periods, the quality of the SEY-data used is very important. In particular, the representativity of SEY at low impact velocities is important. As for multicarrier multipactor, this is the regime where electron losses occur and it will have a significant impact on the multipactor threshold.

When looking at electron growth over several envelope periods, it is also important to consider the case of short but quick electron growth, which can occur for an envelope with high amplitude during a time corresponding to many gap crossings.

Flow chart

Figure 5-20 describes the main steps of the method.

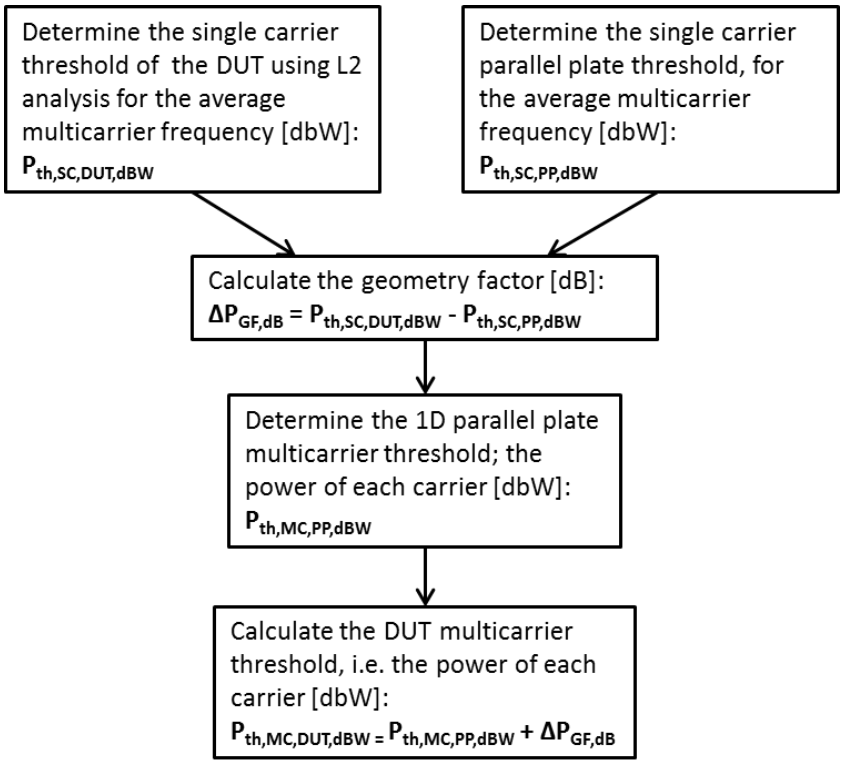


Figure 5-20: Hybrid L1/L2 multi-carrier analysis steps.

When assessing the multipactor threshold in the steps below, make sure the same SEY-data is used in each relevant step. When possible, use the same 3D software to carry out the L2 single carrier analysis, the parallel plate multicarrier, and the single carrier parallel plate problems. Solving the multicarrier parallel plate problem with 3D software is much less time consuming than when using it to solve it in a complex 3D geometry. When 3D multicarrier capability is not available, it is recommended to determine both the multicarrier and single carrier parallel plate thresholds using the same software.

Detailed method description

1. Single carrier L2 (3D) threshold for the DUT

   As a first step, for the DUT use L2 analysis to find the single carrier multipactor threshold and the critical gap, d, using the average frequency of the multicarrier signal. The threshold in dBW is designated $\mathbf{P}_{th,SC,DUT,dBW}$.

2. Single carrier L1 (parallel plate) threshold

   For a parallel plate geometry with a gap distance d, i.e. the size of the critical gap, find the single carrier threshold using the average frequency of the multicarrier signal. The parallel plate threshold in dBW is designated $\mathbf{P}_{th,SC,PP,dBW}$.

3. Geometry factor

   The geometry factor in dB is then calculated as the difference between the single carrier threshold of the L2-analysis and the parallel plate threshold:

   $$\Delta P_{GF,dB} = P_{th,SC,DUT,dBW} - P_{th,SC,PP,dBW} \quad [5\text{-}24]$$

4. Multicarrier parallel plate threshold

   Use the envelope sweep method to determine the worst case phase law as specified in 5.3.2.3.3. The theoretical limit F_V (boundary), which can be used as a target by an optimization/genetic algorithm can be obtained by the following approximation:

   $$F_V(t_{on}) = \sqrt{\frac{T_e}{t_{on}} \sum_{i=1}^{N} E_i^2} \quad [5\text{-}25]$$

   Where E_i is the amplitude of carrier i and N is the total number of carriers. The boundary, F_V, is then limited by the sum of all amplitudes, i.e. it cannot be larger than:

   $$F_{V,Max} = \sum_{i=1}^{N} E_i \quad [5\text{-}26]$$

   Furthermore, it has also a lower limit, when $t_{on} = T_e$, i.e.:

   $$F_{V,Min} = \sqrt{\sum_{i=1}^{N} E_i^2} \quad [5\text{-}27]$$

   Use a 1D PIC-software or similar tool to find the envelope that gives the lowest parallel plate multicarrier threshold. Figure 5-21, and Figure 5-22 show an example of an implementation

where each "on interval" is tested to find the lowest amplitude factor which gives a Γ = 1 over several envelope periods for any of the "on intervals".

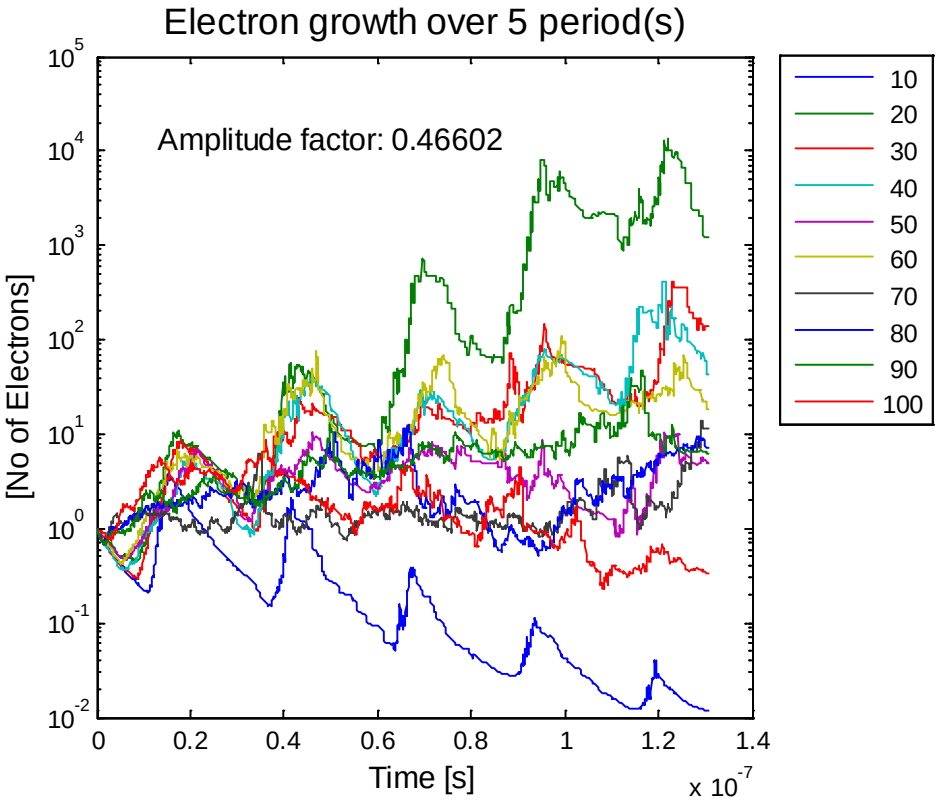


Figure 5-21: Electron growth over 10 envelope periods for 10 different "on intervals" for one amplitude factor

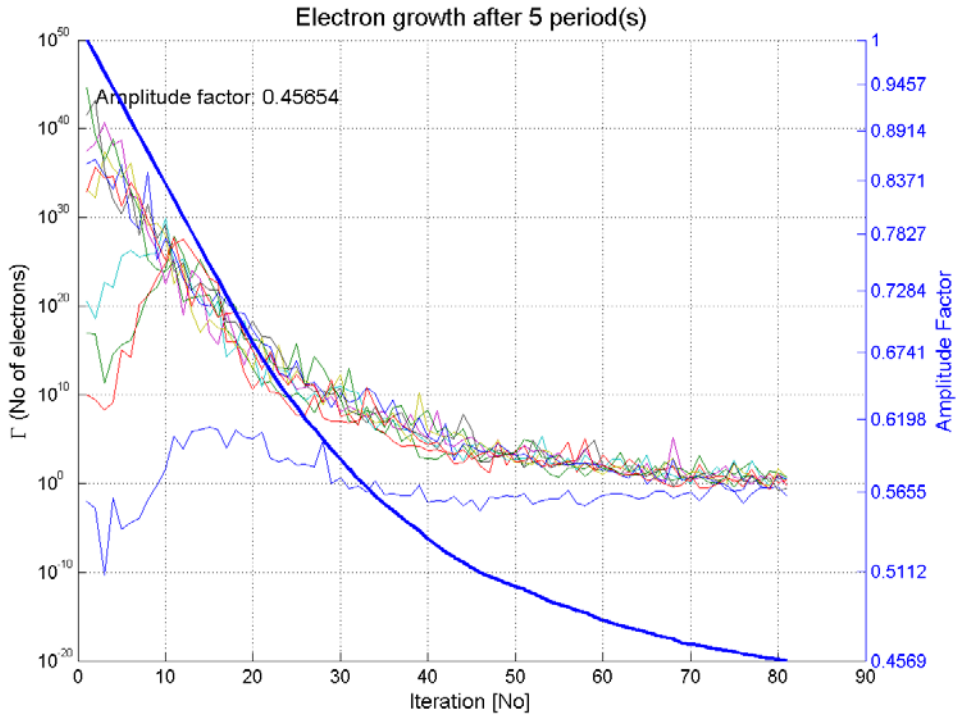


Figure 5-22: Convergence of the amplitude factor, showing also how Γ converges towards one electron

As the resulting amplitudes of each carrier for the multicarrier threshold is found, this can be converted to a power for each carrier in dBW, $\mathbf{P}_{th,MC,PP,dBW}$.

As a comparison with the parallel plate case, one can also plot the sum of all amplitudes in a Hatch & Williams or Sombrin chart for the material in question.

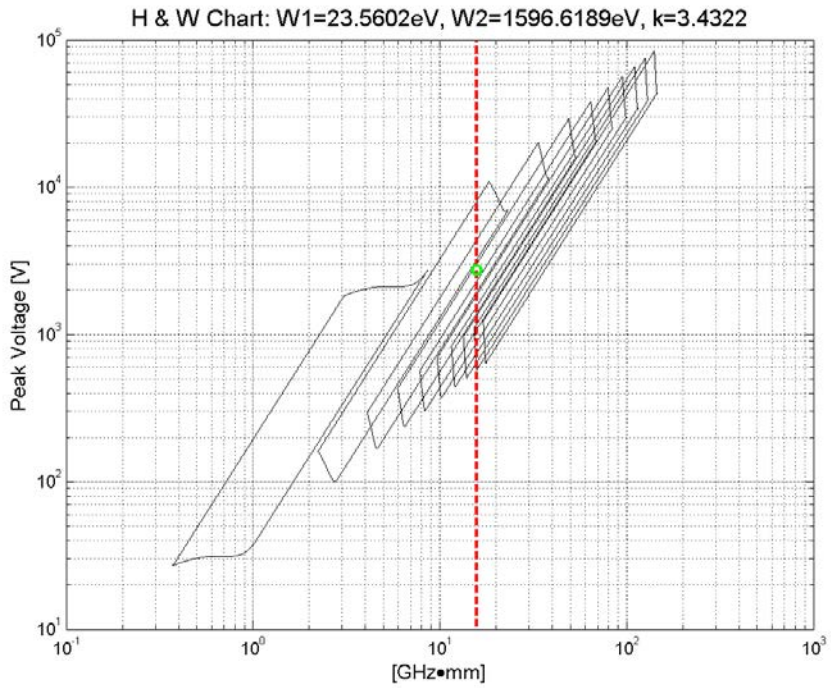


Figure 5-23: Hatch and William chart with the multicarrier in-phase amplitude indicated by a green circle. The red dashed line is the fd-product of the average multicarrier frequency and the critical gap size

5. Multicarrier threshold of the DUT

   The multicarrier threshold can now be determined as the sum of the multicarrier parallel plate threshold power of each carrier plus the geometry factor:

$$P_{th,MC,DUT,dBW} = P_{th,MC,PP,dBW} + \Delta P_{GF,dB} \qquad [5\text{-}28]$$

5.3.2.4 Validation of theory and software

The validation process for a software would consist in taking the definition of the RF component, in computing fields and/or multipactor breakdown, in computing the error with respect the reference and in checking that such error is below the acceptable one.

The definition of the RF component is based on:

- Exact geometry and dimensions
- Electrical properties of materials in the structure
- Operation frequency for EM field and multipactor breakdown computation.
- Integration line (across the critical gap) for voltage computation.
- SEY properties of the materials.

Reference results include:

- Multipactor breakdown power at operation frequency.

Acceptable error for validation is defined for the 2 following quantities:

- Multipactor breakdown power
- Maximum acceptable error (with respect to reference).

5.3.2.4.1 Example of KS3 coming from EVEREST

An example of Multipactor analysis can be given through the EVEREST project [5-12] results in Ku band. The RF component is a transformer with following dimensions:

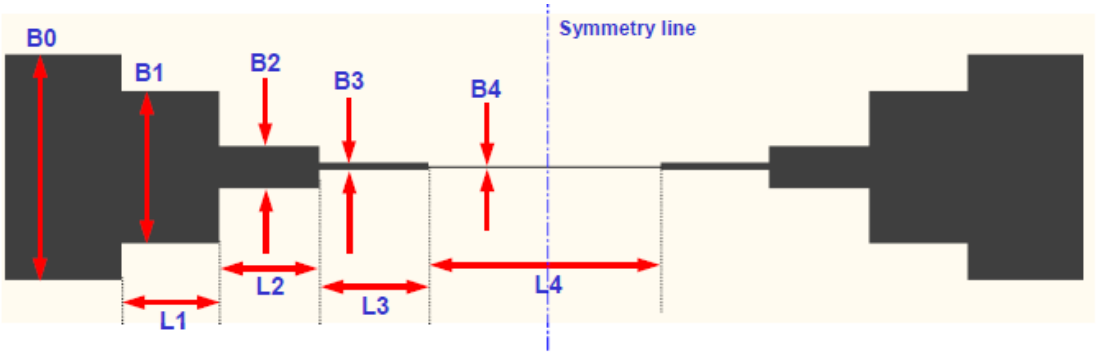


Figure 20: Broadband Reference Sample Dimensions

Parameter	A0	L1	L2	L3	L4
Dimension (mm)	19.05	8.48	8.58	9.37	20
Parameter	**B0**	**B1**	**B2**	**B3**	**B4**
Dimension (mm)	9.525	6.4	1.8	0.32	0.1

Figure 5-24: KS3 sample geometry.

The simulated RF performances are presented in Figure 5-25:

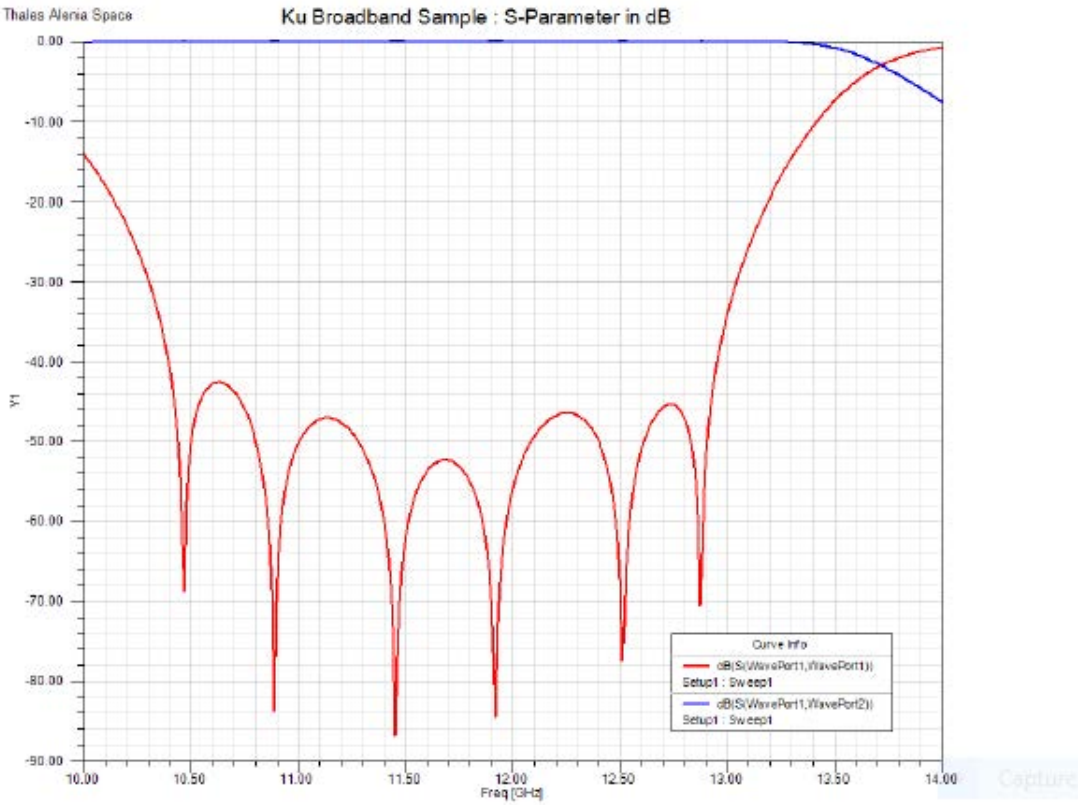


Figure 5-25: KS3 sample simulated RF performance

All the Multipactor simulation results presented hereafter were carefully performed, with enough accuracy.

In each case, four simulations were performed with four different SEY datasets. These four SEY datasets come from the one given in the ECSS, and three measured on SEY samples from three institutions: UAM, CSIC and ONERA. Only silver surfaces have been measured.

We have fitted the SEY model in FEST3D/SPARK3D to the measured data. The fit cannot be perfect and this can add some additional error which cannot be perfectly estimated. However, this error is small since the main characteristics of the SEY are preserved.

In total, it can be stated that the simulations can have an error of ±0,5 dB. Here, we include additional sources of error such as device losses or manufacturing tolerances.

Apart from this purely numerical error, the error arising from the fact that the SEY has not been measured on the actual devices (at the time of the high power test) but on separated plates (at times different to each high power test) cannot be assessed and adds, possibly, the main source of error between measurement and simulation.

The SEY main characteristics are summed up in Table 5-5, knowing that the SEY value at zero energy is 0,5.

Table 5-5: SEY characteristics of KS3 sample

Silver ECSS			CSIC			UAM			ONERA			CSIC (Revised)		
E1 (eV)	Emax (eV)	σmax	E1 (eV)	Emax (eV)	σmax	E1 (eV)	Emax (eV)	σmax	E1 (eV)	Emax (eV)	σmax	E1 (eV)	Emax (eV)	σmax
30	165	2,22	29,3	363,7	2,32	20,5	314,1	2,34	21	330,5	2,227	24,1	338	2,15

Table 5-6 sums up the Multipactor threshold values coming from both simulations with different SEY measurements and from the Multipactor test.

Table 5-6: Multipactor thresholds for KS3 sample

Sample	Freq. / GHz	Silver ECSS	CSIC	UAM	ONERA	CSIC (Revised)	ECSS MTool	Measurement
K-S3	12,5	370	400	312	308	350	408	251

The sensitivity of the Multipactor threshold to the SEY data and among all the parameter E1 is quite important.

5.3.2.4.2 Example of L band filter of EVEREST

An example of Multipactor analysis results in L band can be given through the EVEREST project [5-12].

Initially a 3rd degree bandpass filter structure designed by COM DEV and used for multipactor verification was proposed as a suitable device design, see Figure 5-26. This device consists of 3 cavities containing coaxial resonator structures, where the input and output resonators are magnetically coupled to the input and output TNC connectors and the central resonator couples to these via irises. The input and output resonators are based on previous designs as these have very high multipactor thresholds – this complete resonator structure consists of a top-hat resonator tuned by a disc tuner above it. The central resonator was designed to also be a top-hat resonator where it is known from experience that there are significant fringing fields, as the multipactor thresholds are significantly higher than an

equivalent parallel-plate geometry (see 5.3.2.2.2). This basic design had to be progressed through several more iterations of modifying the resonator heights and tuner-resonator spacers in order to provide a breakdown threshold (by increasing the voltage in the critical gap) that was achievable in the participating test facilities and at the frequencies that are available there. It was finally decided to provide a single device where either centre frequency can be achieved in the device simply by tuning the filter appropriately.

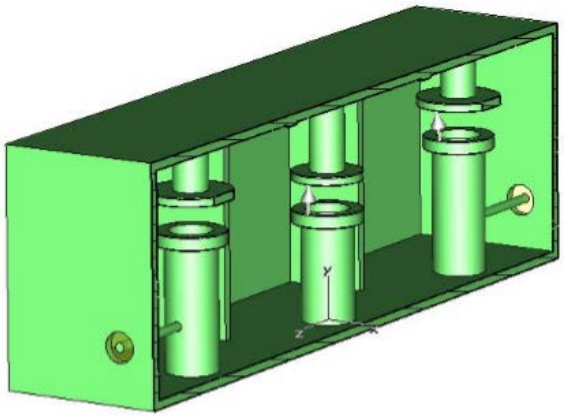


Figure 5-26: 3D view of L-band sample

After several iterations, the resonators and cavity heights have been reduced in size and the diameters of the input and output tuners have been increased in order to reduce the breakdown threshold for the central resonator (where the voltage is largest) and to increase the threshold of the input and output resonators relative to the central one. The heights of the input/output tap wires (which control the input/output coupling bandwidths) have also been increased slightly in order to allow tuning over a larger frequency range, so that sufficient performance can be achieved from 1525 MHz to 1400 MHz.

The filter is readily tuneable over the frequency range of 1400 MHz to 1525 MHz, maintaining a return loss of > 23 dB. Breakdown is designed to occur preferentially between the central resonator and central tuner disc, where the gap is expected to be approximately 6,5 mm, for a centre frequency of 1525 MHz and 5,0 mm for a centre frequency of 1400 MHz. The gaps between the input and output resonators-tuners are slightly larger and the voltages are also somewhat lower – this helps to ensure the breakdown occurs at the central resonator. The input and output tuners have also been deliberately increased in diameter to maximise this gap, although this does also reduce the fringing effect slightly with a consequent lowering of the threshold.

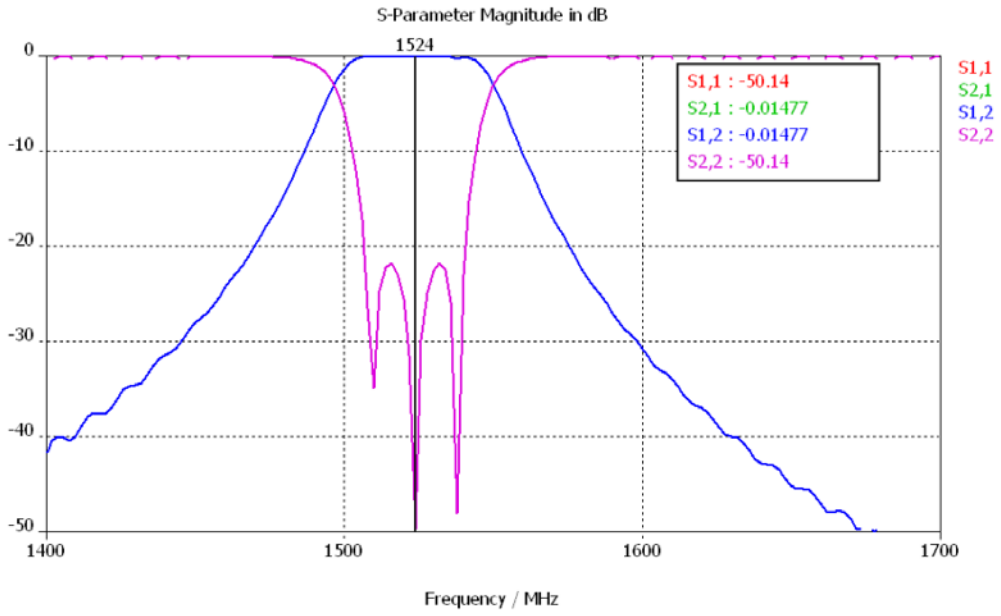


Figure 5-27: Predicted S-parameter Performance of Preliminary L-band RF Device Design

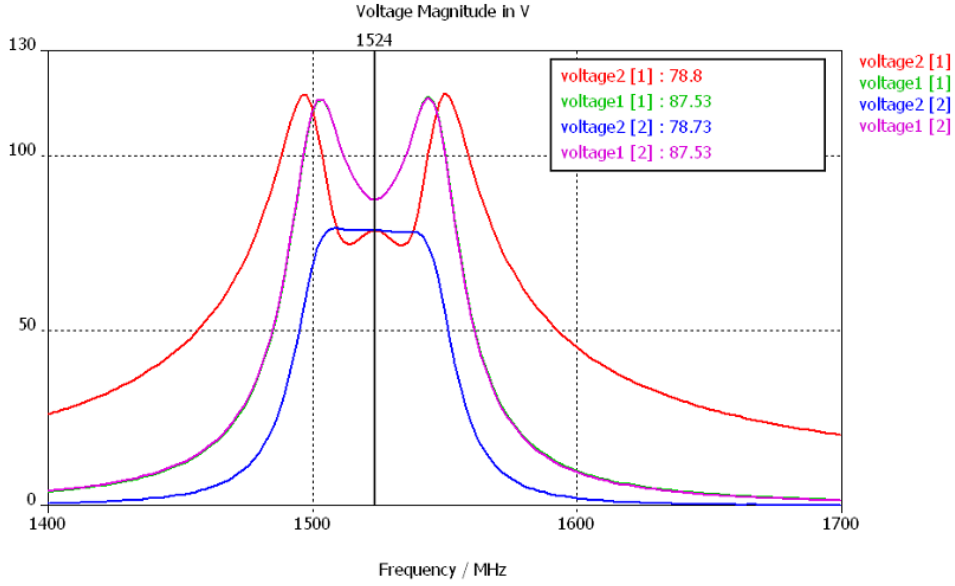


Figure 5-28: Predicted Voltage Distribution in Preliminary L-band RF Device Design

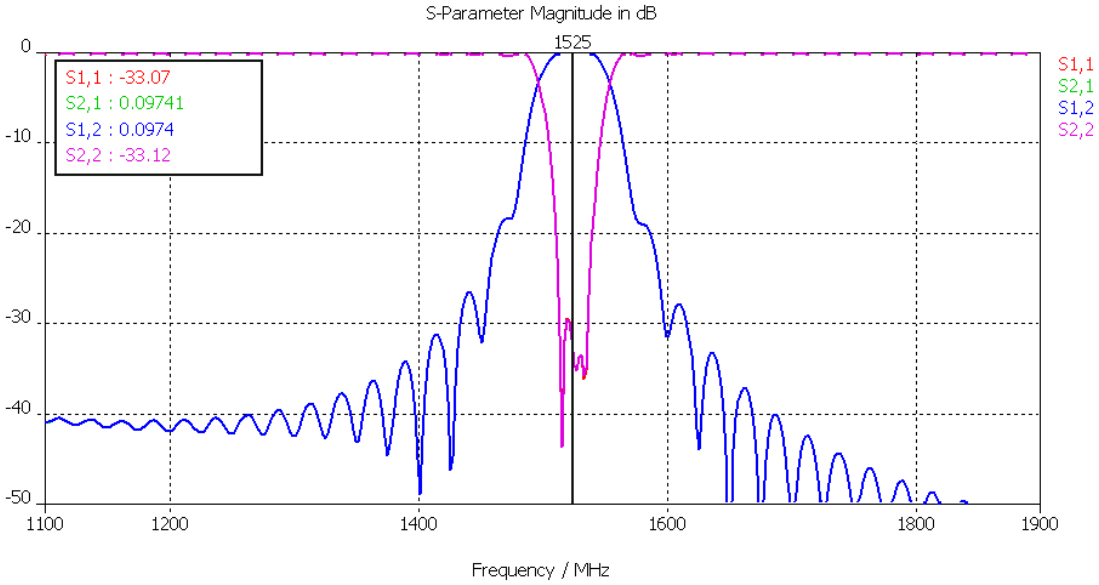


Figure 5-29: Predicted S-parameter Performance of Finalised L-band RF Device (1525 MHz)

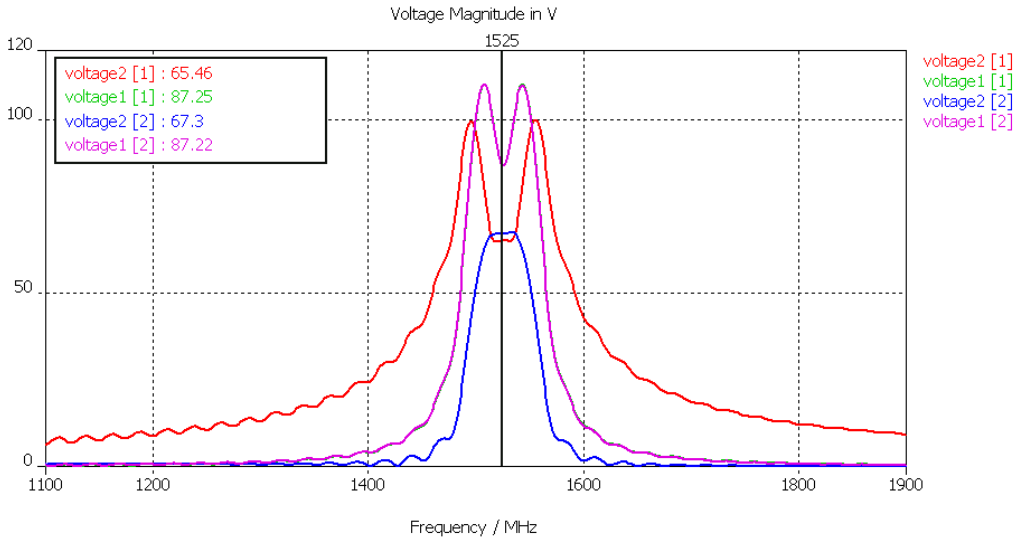


Figure 5-30: Predicted Voltage Distribution in Finalised L-band RF Device (1525 MHz)

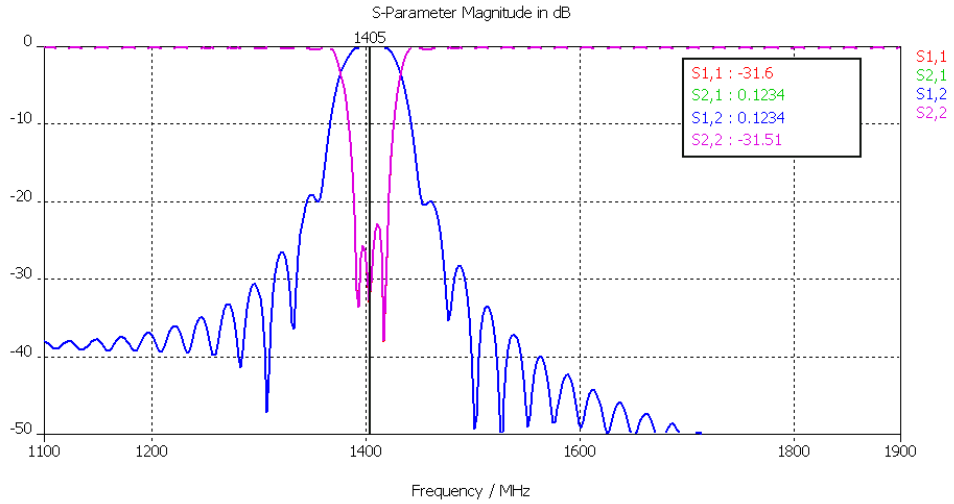


Figure 5-31: Predicted S-parameter Performance of Finalised L-band RF Device (1405 MHz)

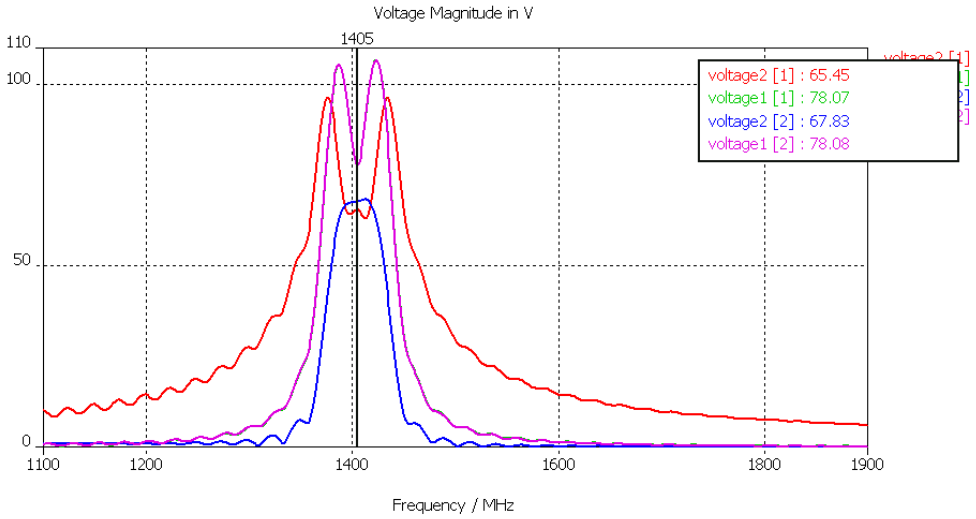


Figure 5-32: Predicted Voltage Distribution in Finalised L-band RF Device (1405 MHz)

A short investigation has been made to demonstrate how the voltage on the central resonator varies with change in bandwidth of the filter. A circuit theory modelling technique (proprietary to COM DEV) has been used to predict the voltage variation on each resonator, across a frequency span that is larger than the filter design bandwidth for 5 different design bandwidths. The return loss and center frequency of the filter have been fixed for all plots, so that only the effect of the bandwidth change can be observed. This situation does not correspond directly to the case of re-tuning the proposed filter design as a change in its bandwidth is accompanied by a change in return loss, due to the fact that the input/output couplings are not physically optimized during that re-tuning process (only the resonators and iris couplings can be externally tuned).

Example plots of the voltage variation for the 3 resonators over a wide frequency span are shown for the largest and smallest bandwidths investigated – these can be seen in Figure 5-33 and Figure 5-34.

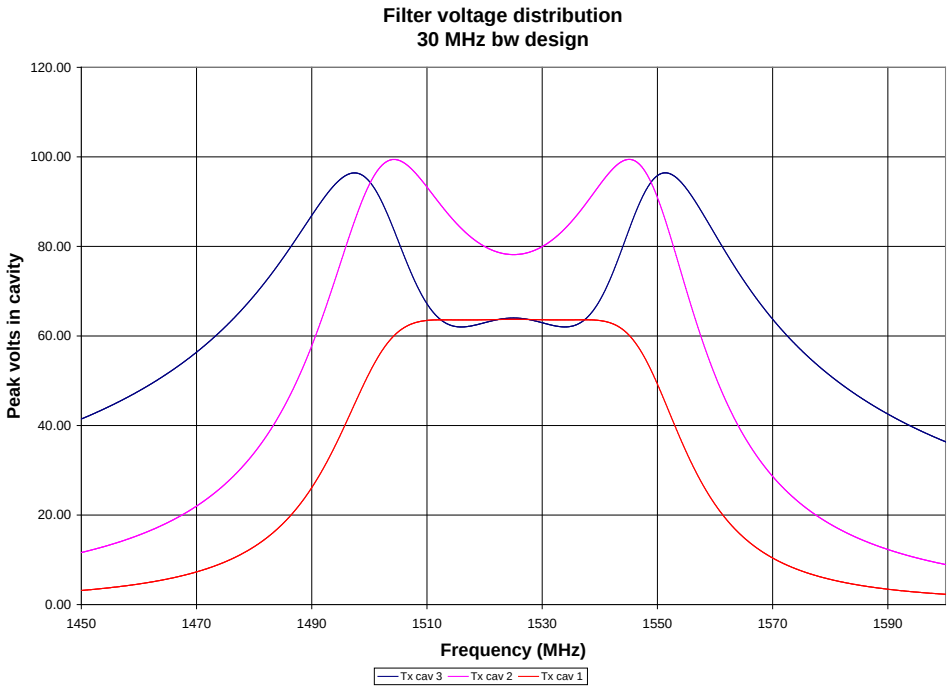


Figure 5-33: Variation of peak voltage on each resonator with frequency – 30 MHz design bandwidth

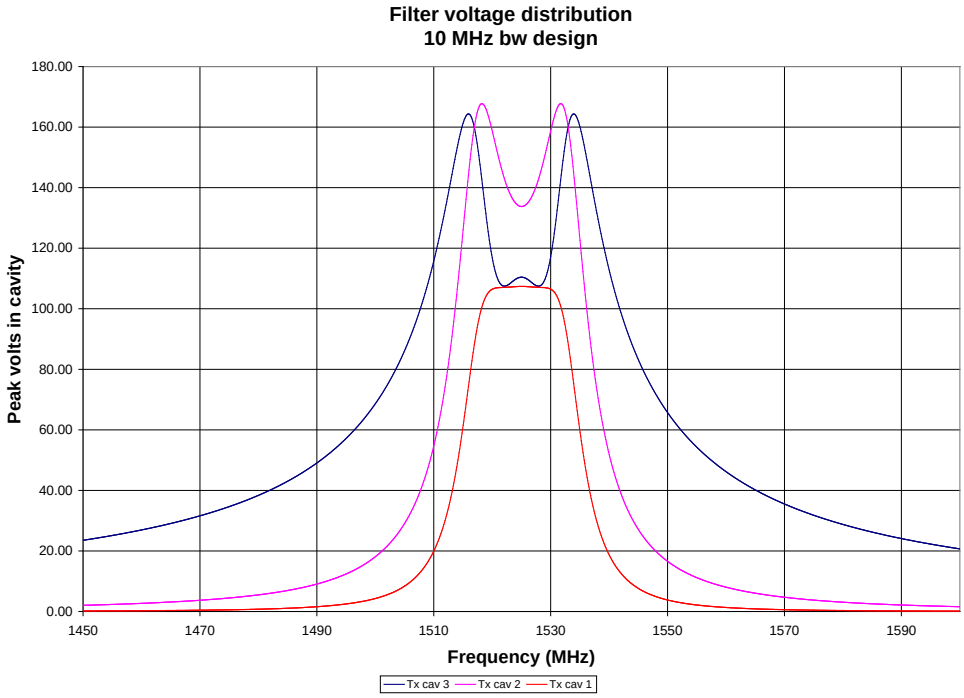


Figure 5-34: Variation of peak voltage on each resonator with frequency – 10 MHz design bandwidth

Figure 5-35 presents a summary plot showing how the peak voltage varies on the central resonator as the design bandwidth is changed, for a set return loss (25 dB) and center frequency of operation (1525 MHz).

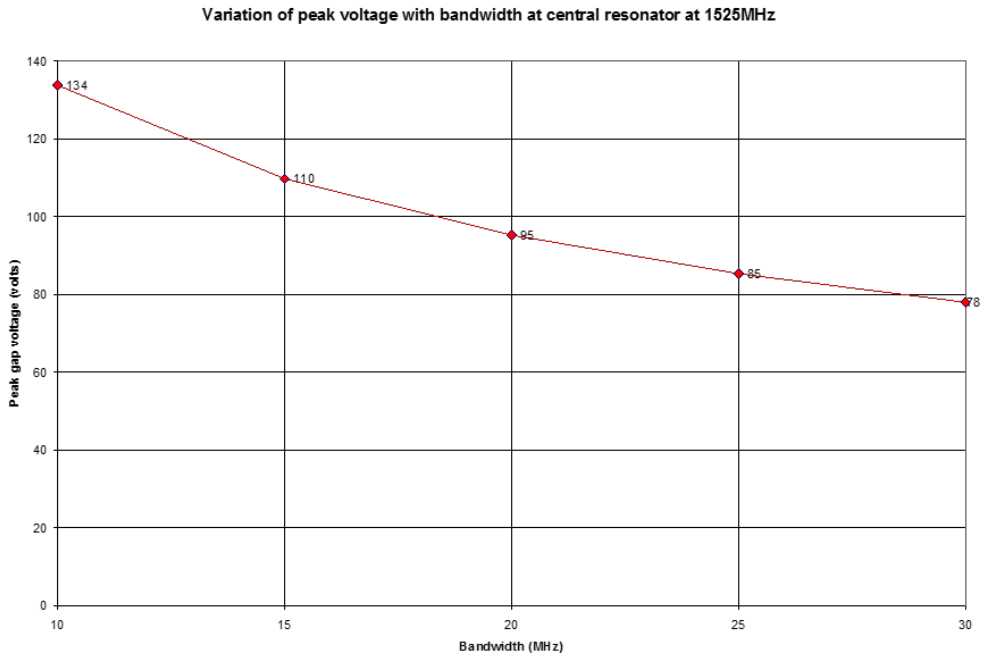


Figure 5-35: Variation of peak voltage on central resonator with bandwidth change (Fc = 1525 MHz)

It will be noted that there is a substantial increase in peak voltage at the central resonator when decreasing the design bandwidth from 30 MHz to 10 MHz, with the voltage increasing from 78 volts to 134 volts. It is important to note however, that achieving such a narrow bandwidth might not always be possible due to the construction of the input/output couplings of this particular filter design. The bandwidth that has been selected in the final test device design allows a good degree of variation of peak voltage whilst enabling practical input/output couplings to be readily realized.

Table 5-7: SEY data for L-band sample

Sample	Silver ECSS			CSIC			UAM			ONERA			CSIC (Revised)		
	E1 (eV)	Emax (eV)	σmax	E1 (eV)	Emax (eV)	σmax	E1 (eV)	Emax (eV)	σmax	E1 (eV)	Emax (eV)	σmax	E1 (eV)	Emax (eV)	σmax
L-D1	30	165	2,22	25,5	303	2,02	24	325	2,06	20	250	1,985	27,9	319	2,07
L-D2	30	165	2,22	29,3	371,1	2,07	23	324,1	2,24	20	300	2,123	27,9	319	2,07
L-D3	30	165	2,22	29,3	371,1	2,07	23	324,1	2,24	20	300	2,123	27,9	319	2,07
L-D5	30	165	2,22	19,5	361,3	2,51	25	354	2,62	17	364	2,67	18,5	372	2,81
L-D6	30	165	2,22	14	240	2,64	15	300	2,13	16	275	2,575	14,4	241	2,49

Table 5-8: Multipactor thresholds for L-band sample

Sample	Freq. / GHz	Silver ECSS	CSIC	UAM	ONERA	CSIC (Revised)	ECSS MTool	Measurement
L-D1	1,525	100	114	112	109	117	22	112
L-D2	1,525	104	125	104	106	118	22	90
L-D3	1,4	31	40	34	34	38	22	38
L-D5	1,525	81	70	73	42	56	18	141
L-D6	1,4	27	15,5	27	21	19	10	32

The results, in this case, show clearly the impact of the fringing effect on the breakdown power level. Interestingly, this difference is somehow reduced for L-D3 and LD-6. The reason for this can be that these two samples have the smallest gap and operate at the lowest frequency, so the impact of the fringing effect is mitigated. However, for L-D1, L-D2 and L-D5, the impact is more important: the difference between the parallel plate approach and some numerical calculations is as high as 9 dB.

5.3.3 Available data for Multipactor analysis

5.3.3.1 General

No supporting material needed.

5.3.3.2 Dimensional accuracy and stability

Several analyses have been performed to evaluate the impact of machining tolerances on RF performances. Standard error is +/- 0.04 mm except for the critical gap: +/- 0,02 mm.

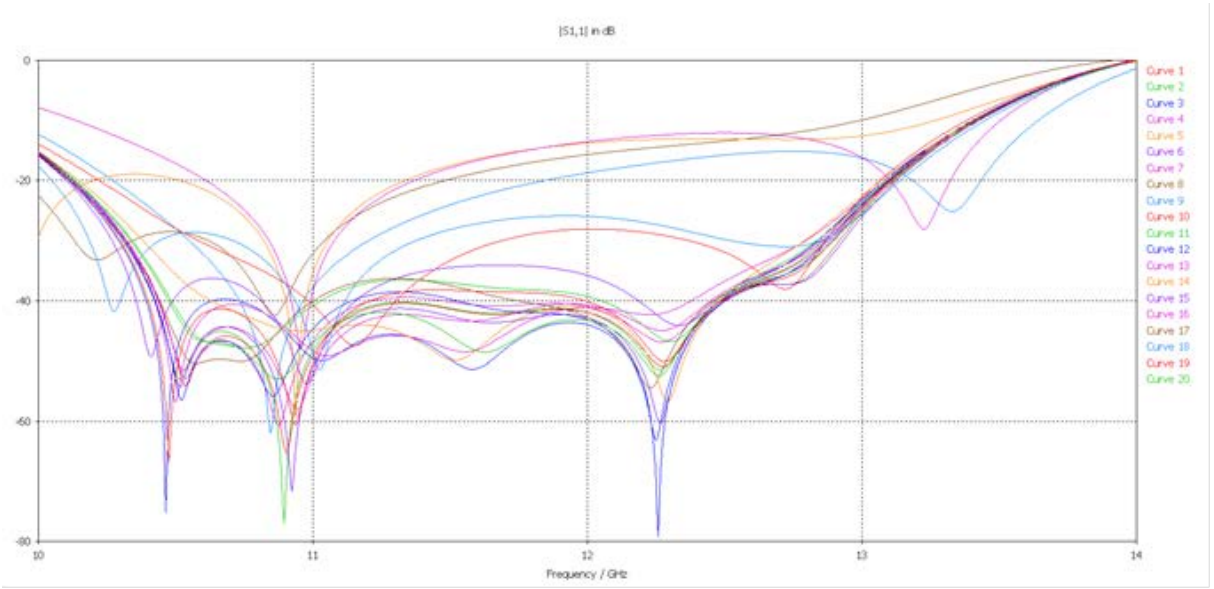


Figure 5-36: RF performances with machining tolerances (Resonant reference sample S-3 and S-4)

Electric field analysis

An analysis of the electric field variation has been performed. Several locations are taken into account to calculate the voltages in the middle of the sample section (Figure 5-37).

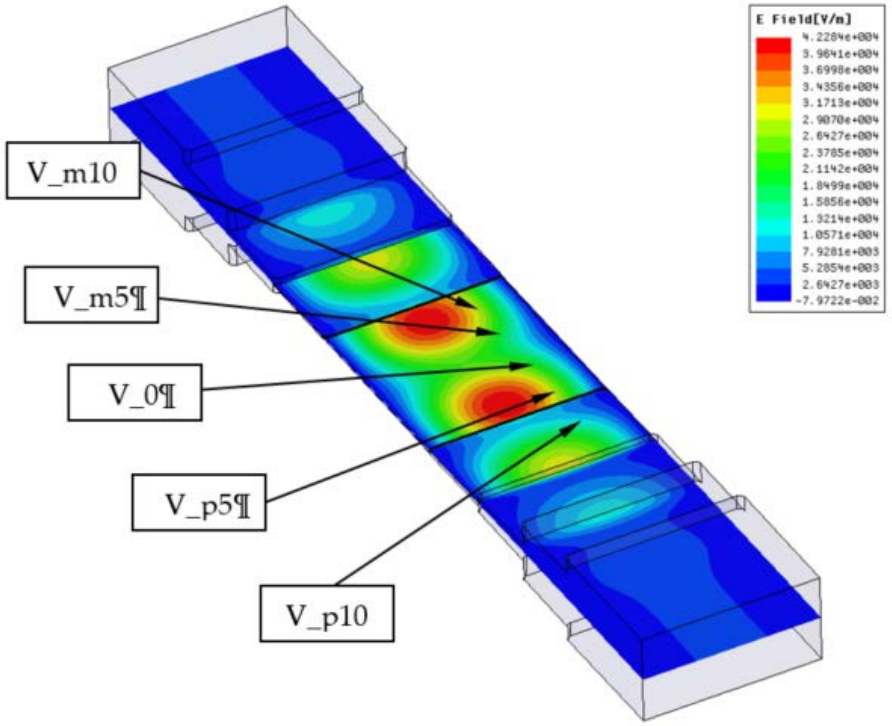


Figure 5-37: Electric field (12,75 GHz – samples S-3 and S-4)

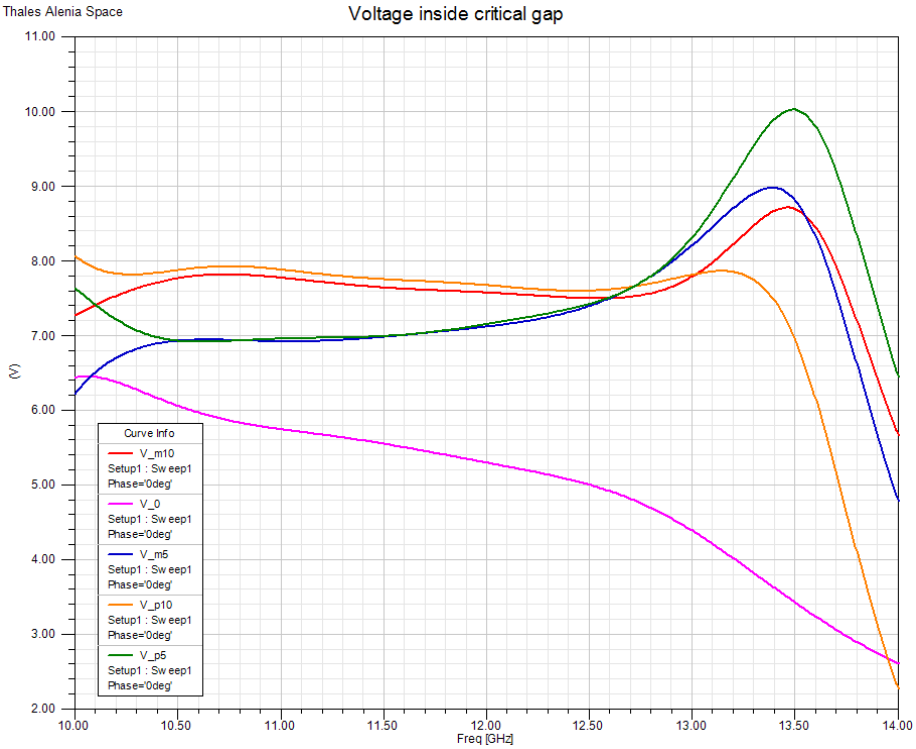


Figure 5-38: Voltage inside critical gap (samples S-3 and S-4)

The critical gap dimension is 0,1 mm. To calculate the multipactor threshold, an analysis of the central zone of the component has been done using FEST3D. Simulations have been also performed with a variation of +/- 0,02 mm to predict the threshold variations due to manufacturing errors.

Table 5-9: Multipactor threshold vs. manufacturing errors (samples S-3 and S-4)

Gap	10,5 GHz	13 GHz
0,1 mm	**160 W**	**230 W**
0,1 – 0,02 mm	125 W	145 W
0,1 + 0,02 mm	275 W	405 W

For the critical gap, the multipactor theoretical threshold is about 160 – 230 W over the [10,5 – 13] GHz bandwidth.

Component with RF tuning element

Manufacturing tolerances lead to deviation between the simulated RF-performance and measured one. To minimize this deviation, tuning screws are used. The tuning screws are located in suitable places to reduce this discrepancy. Furthermore, tuning screws are used to couple electromagnetic fields or to adjust the coupling between resonant structures.

In modern RF FEM models tuning screws are part of the simulated component. This approach allows manufacturing of hardware with similar performance with respect to the simulated one. This is achieved by tuning the hardware by means of changing the tuning screw penetration depth. The goal of the tuning is to recover the simulated RF performance. It can happen that the penetration depth differs between the hardware and the FEM model. It is observed that, in general, the influence of the tuning screws on the Multipactor threshold is negligible as long as the post-tuning RF performance complies with the predicted one and the tuning screw is not part of the critical gap.

The next filter examples demonstrate the statement. Simulated is a filter with tuning screws located in the middle side of the resonators. One filter shows the nominal model. The length of the third resonator of the second filter is extended of 0,03 mm, what corresponds to the current mechanical tolerance. This resonator is re-tuned to minimize the effect of the larger volume. Therefore, the penetration depth of the tuning screws is increased by 1,36 mm. In this particular case, the tuning screws are not located in the critical area from multipactor point of view. The next 3D views clarify the situation:

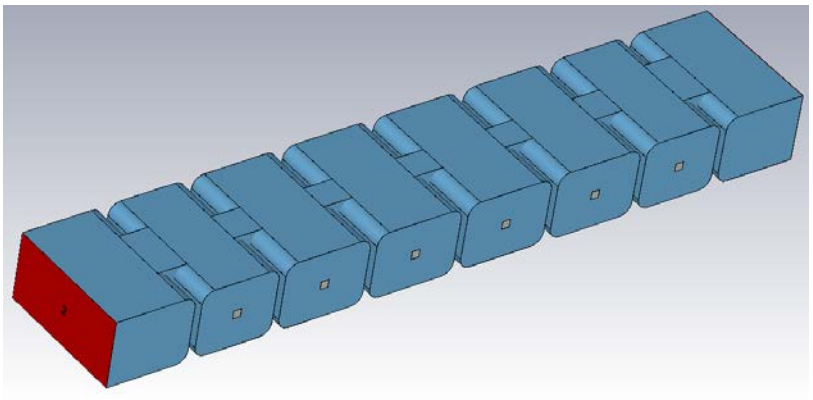


Figure 5-39: Nominal model

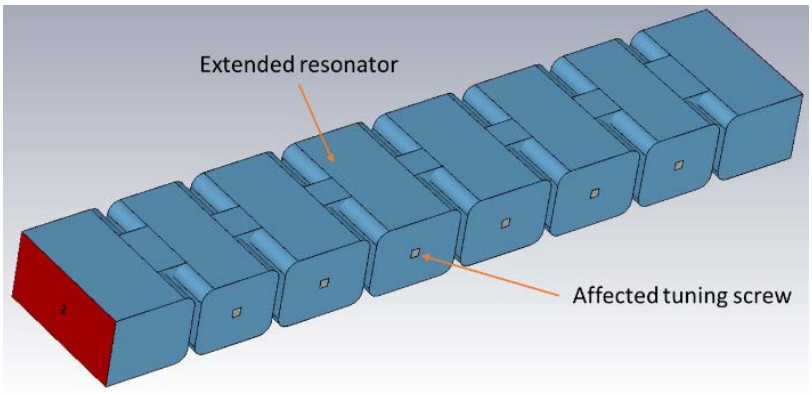


Figure 5-40: Re-tuned model

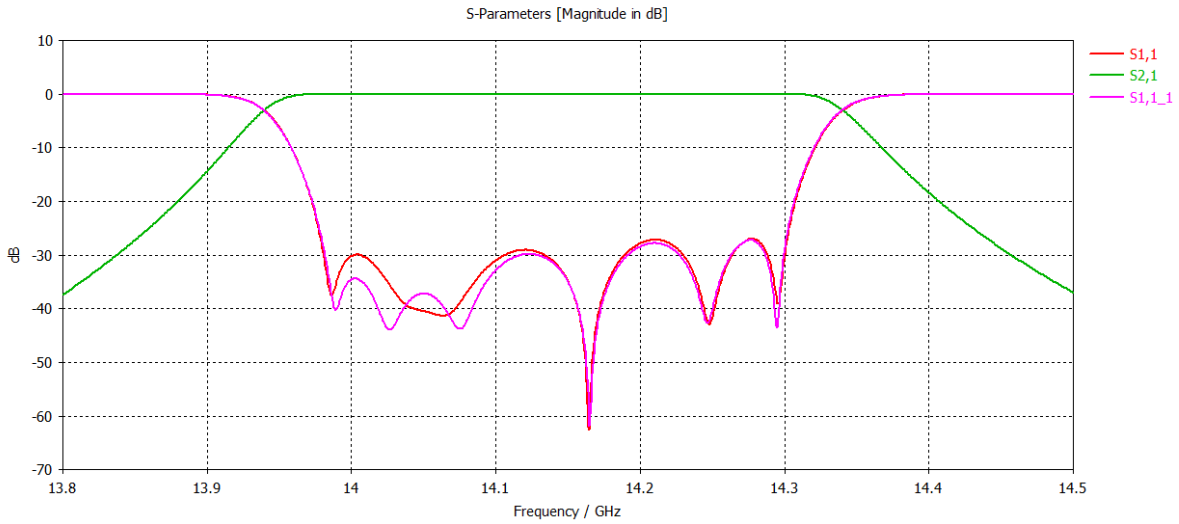


Figure 5-41: Return Loss nominal (red) and tuned (pink)

The multipactor analysis was performed with Spark3D 2019. The conditions and settings for the FEM simulation and the multipactor analysis for both models are identical. The expected multipactor occurs first in resonator 3 and 4, counting from the left side to the right side.

The predicted threshold of the nominal model is 930W and of the re-tuned model is 960W.

The difference is less than 0,137dB.

In the case of OMUX filters with coupled cylindrical cavities, the multiple tuning screws per cavity are in general not in the multipactor critical area. The critical area is in general located in the iris.

5.3.3.3 SEY available data

No supporting material needed.

5.3.3.4 ECSS Multipactor charts

No supporting material needed.

5.4 Bibliography for clause 5

[5-1] ”Microwave filters for communications systems” R. Cameron, C. Kudsia, R. Mansour, 2nd Edition, Wiley 2018.

[5-2] Sergio Anza, Carlos Vicente, David Raboso, Jordi Gil, Benito Gimeno, and Vicente E. Boria. Enhanced Prediction of Multipactor Breakdown in Passive Waveguide Components including Space Charge effects. In IEEE International Microwave Symposium, pages 1095{1098, Atlanta, USA, Jun 2008.

[5-3] J. Vague et al., "Multipactor Effect Characterization of Dielectric Materials for Space Applications," in IEEE Transactions on Microwave Theory and Techniques, vol. 66, no. 8, pp. 3644-3655, Aug. 2018.

[5-4] Y. Li, D. Wang, M. Yu, Y. He and W. Cui, "Experimental Verification of Multipactor Discharge Dynamics Between Ferrite Dielectric and Metal," in IEEE Transactions on Electron Devices, vol. 65, no. 10, pp. 4592-4599, Oct. 2018.

[5-5] R. Udiljak, D. Anderson, M. Lisak, J. Puech, and V. Semenov, “Multipactor in a waveguide iris,” Plasma Science, IEEE Transactions on, vol. 35, pp. 388 –395, April 2007.

[5-6] V. E. Semenov, E. Rakova, R. Udiljak, D. Anderson, M. Lisak, and J. Puech, “Conformal mapping analysis of multipactor breakdown in waveguide irises,” Physics of Plasmas, vol. 15, no. 3, p. 033501, 2008.

[5-7] S. Anza, C. Vicente, J. Gil, V. E. Boria, B. Gimeno, and D. Raboso, “Nonstationary statistical theory for multipactor,” Physics of Plasmas, vol. 17, p. 062110, June 2010.

[5-8] “The Study of Multipactor Breakdown in Space Electronic Systems,” Tech. Rep. CR-448, contract. NAS 5-3916, NASA report, July 1966.

[5-9] P. Mader, J. Puech, D. Anderson, F. Gizard, P. Lepeltier, M. Lisak, J. Lopez, E. Rakova, V. Semenov, and J. Sinigaglia, “Highlights of the Fringing Field Effect at C-band on Waveguide Components,” in Proceedings of the 7th International Workshop on Multipactor, RF and DC Corona and Passive Intermodulation in Space RF Hardware, Valencia, Spain, Sept. 21-23 2011.

[5-10] “Multipactor and Corona Discharge: Prediction, Simulation and Design,” Final report ESA/ESTEC No.16827/02/NL/EC, Technical University of Darmstadt (Prime Contractor), Laboratoire d’Electromagnetisme et d’Acoustique (Subcontractor) and TESAT Spacecom GmbH & Co KG (Subcontractor), March 2006.

[5-11] "Study of High Order Modes and Fringing Fields in Multipactor Effect". Final Report ESA-ESTEC AO/1-5918/NL/GLC.

[5-12] J. Puech et al, “Synthesis of the results of the EVEREST project,” MULCOPIM Workshop, 2014.

[5-13] Multipactor in Multicarrier Systems. Theory and Prediction, S. Anza, PhD 2018.

[5-14] S. Anza, C. Vicente, B. Gimeno, V. E. Boria, J. Armendáriz, Long-term multipactor discharge in multicarrier systems, Physics of Plasmas, pg. 082112, vol. 14(8), 2007.

[5-15] S. Anza et al., "Prediction of Multipactor Breakdown for Multicarrier Applications: The Quasi-Stationary Method," in IEEE Transactions on Microwave Theory and Techniques, vol. 60, no. 7, pp. 2093-2105, July 2012.

[5-16] D. Wolk, D. Schmitt, and T. Schlipf. A novel approach for calculating the multipactor threshold in multicarrier operation. In Proceedings of the 3rd International Workshop on Multipactor, RF and DC Corona and Passive Intermodulation in Space RF Hardware, pages 85-91. ESTEC, Noordwijk, The Netherlands, Sept. 4-6. 2000.

[5-17] J.C. Angevain, L.S. Drioli, P.S. Delgado, and C. Mangenot. A boundary function for multicarrier multipactor analysis. In Antennas and Propagation, 2009. EuCAP 2009. 3rd European Conference on, pages 2158 -2161, March 2009.

[5-18] J.C. Angevain, A boundary function for multicarrier multipactor analysis, MULCOPIM 2008 24-26 September 2008, Valencia, Spain.

[5-19] “RF Breakdown in Multicarrier Systems" (1-9918/06/NL/GLC).

[5-20] C. Vicente, M. Mattes, D. Wolk, H. L. Hartnagel, J. R. Mosig, and D. Raboso. Multipactor breakdown prediction in rectangular waveguide based components. In Microwave Symposium Digest, 2005 IEEE MTT-S International, volume 2, pages 1055{1058. Long Beach, California, USA, edited by Institute of Electrical and Electronics Engineers, IEEE, New-York, Jun. 12-17 2005.

[5-21] D. González-Iglesias, Ó. Monerris, B. G. Martínez, M. E. Díaz, V. E. Boria and P. M. Iglesias, "Multipactor RF Breakdown in Coaxial Transmission Lines With Digitally Modulated Signals," in IEEE Transactions on Electron Devices, vol. 63, no. 10, pp. 4096-4103, Oct. 2016.

[5-22] ECSS Multipactor Tool, ESA 2018

6 Multipactor - Test conditions

6.1 Cleanliness

Examples of clean room work and conditions are shown below.



Figure 6-1: Work in a clean room environment.

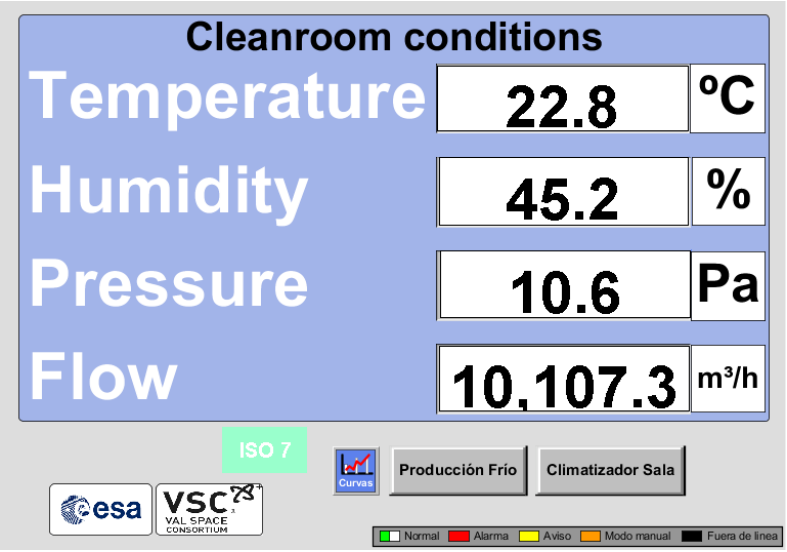


Figure 6-2: Screenshot of clean room monitoring. The pressure reading corresponds to the overpressure delta in the clean room.

6.2 Pressure

Prior to multipactor testing, the component or equipment under test is exposed to normal environmental conditions. A good rationale is provided in [6-1], where it is stated that: "*The majority of RF components are exposed to ambient, atmospheric (air) conditions prior to on-orbit operation; as such, some degree of recontamination of water vapour and other species present in ambient air will occur. Once on-orbit, these gases can persist for many months given low component temperatures prior to RF operation. This requirement exists to provide a test-like-you-fly condition for the multipactor test, providing a realistic surface condition and outgassing scenario similar to the first application of power for the component on-orbit.*"

Multipactor tests are performed under high vacuum conditions. Before testing, a simple bake out is performed at +65 °C to +85 °C during 8 hours to 12 hours. For RF cables, a typical temperature is +110°C.

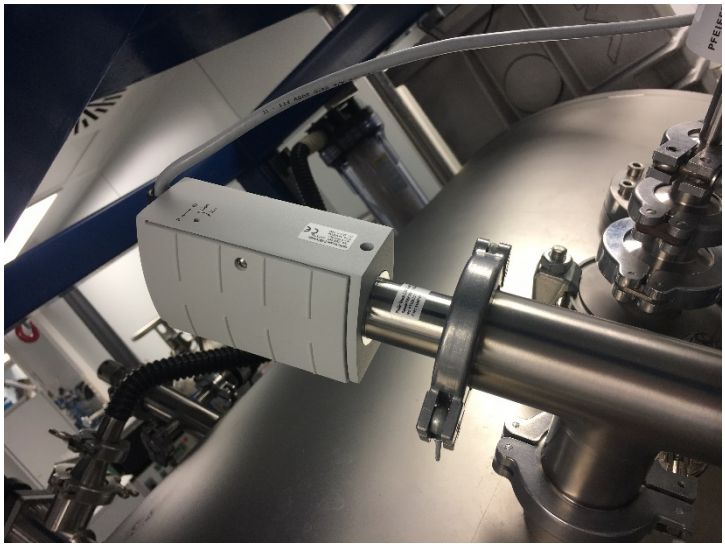


Figure 6-3: A pressure gauge.

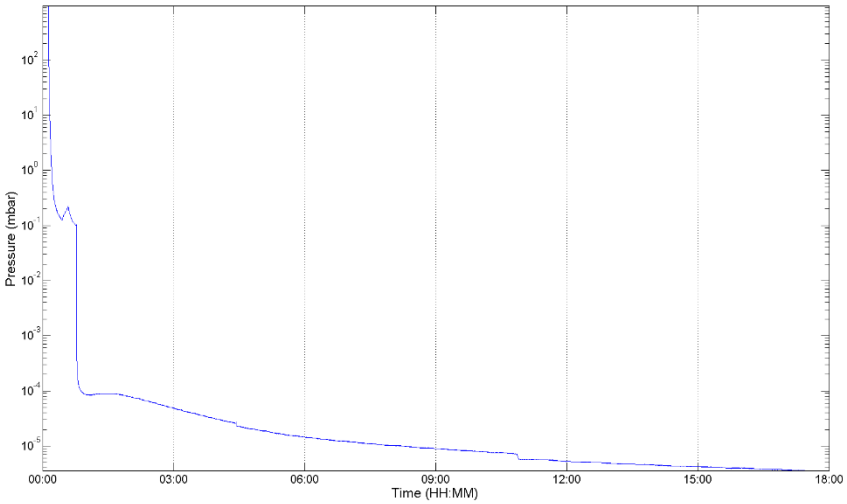


Figure 6-4: Picture of a typical pressure profile for a P1 component or equipment.

Figure 6-5 shows an example of a pressure profile for a P2/P3 component with pressure spikes related to outgassing. In this example, additional bake out is needed, possibly at higher temperatures, before starting the multipactor test.

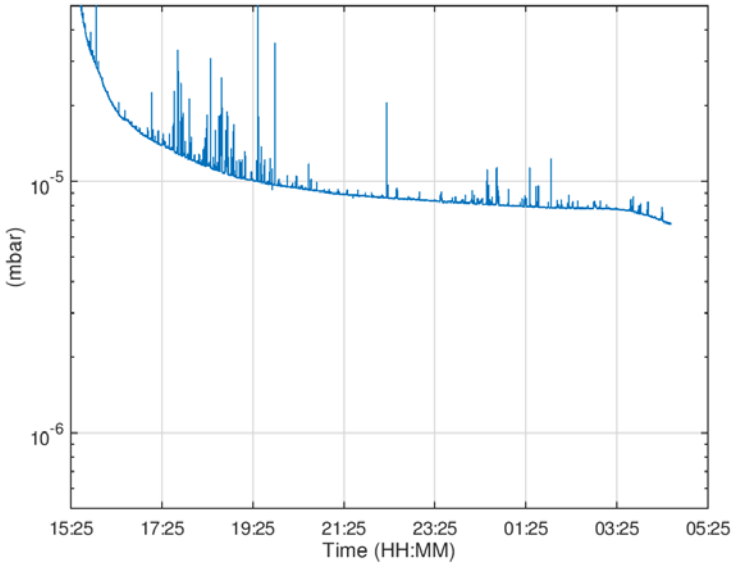


Figure 6-5: Picture of a typical pressure profile for a P2/P3 component or equipment with pressure spikes related to outgassing.

6.3 Temperature

Figure 6-6 shows an example of an RF cable with the temperature monitored by thermocouples during the multipactor test.

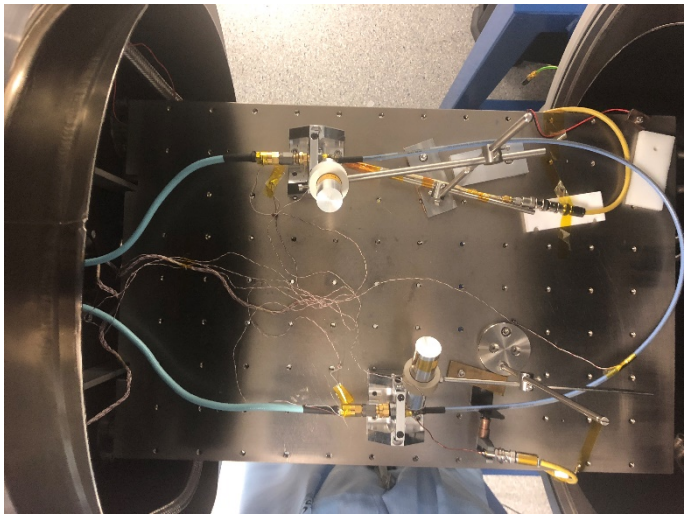


Figure 6-6: RF cable with thermocouples.

During the multipactor test, the component or equipment temperature is monitored continuously. The temperatures measured during the cable test in Figure 6-6 are shown in Figure 6-7 as an example.

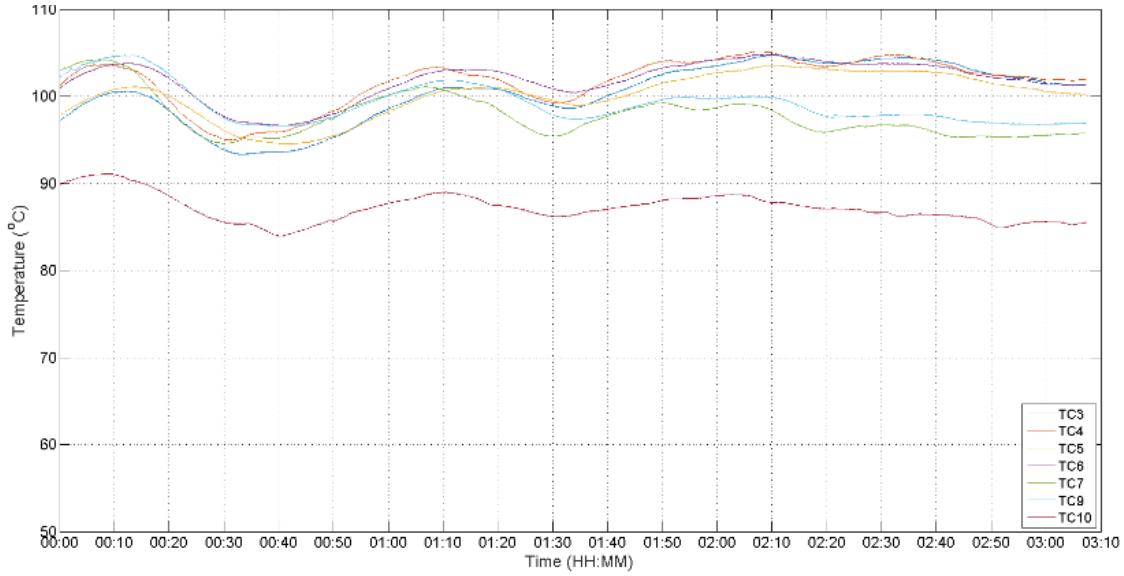


Figure 6-7: RF cable with thermocouples.

For a discussion related to test in ambient temperature, see 4.6.3.

6.4 Signal characteristics

6.4.1 Applicable bandwidth

No supporting material needed.

6.4.2 Single-frequency test case

No supporting material needed.

6.4.3 Multi-frequency test case

6.4.3.1 General

a) Multicarrier test setup examples



Figure 6-8: A multicarrier test facility

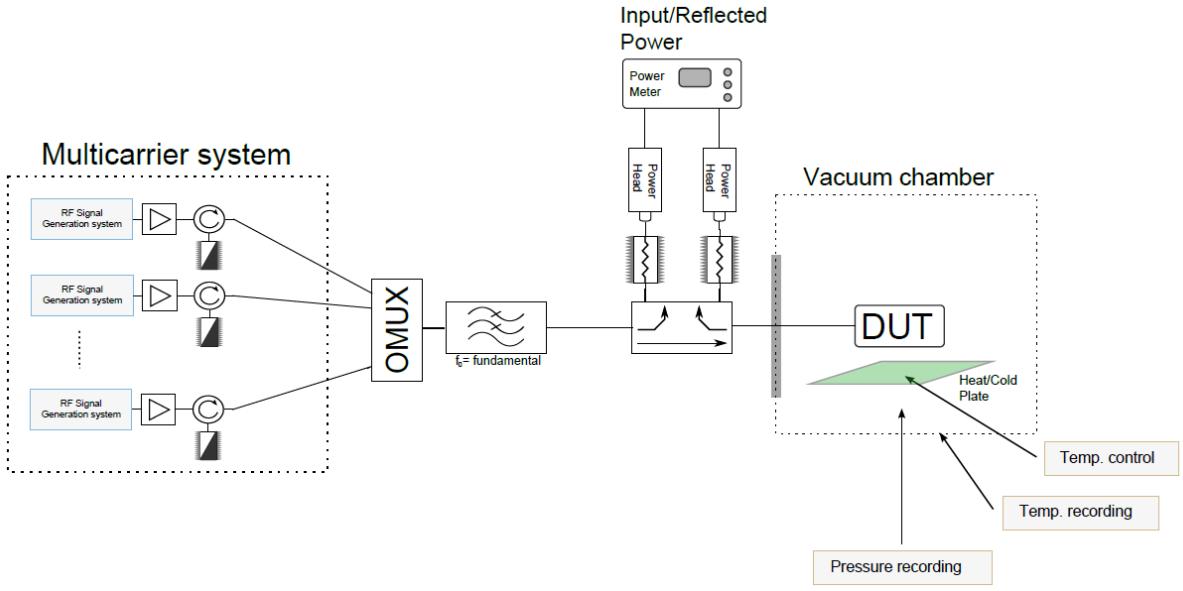


Figure 6-9: Schematic of a three-carrier multipactor test bed

b) Free-running case margin justification

In order to determine the multicarrier test margin with the free-running phase test operations, it is necessary to establish the impact of the multi-carrier phase distribution in the multipactor breakdown.

A statistical study was performed with different parameters to set up rule of thumbs based on the different parameters such as frequency or number of carriers, applicable to the normative document.

For the statistical study, a 1D parallel plate was considered using the non-stationary theory. 1000 random phase cases were simulated.

In each case, different *f·d* products, materials and number of carriers were taken into account. Each phase distribution is kept constant for each iteration.

For example, in the case below, 10 carriers were simulated with f_{mean}=11 GHz, Δf=50 MHz, using material parameters of silver and aluminium.

The two following graphs shown in Figure 6-10 were computed for two typical *f·d* products. The graphs represent the probability density distributions of the errors between the worst case thresholds and the simulated thresholds for all phase distributions.

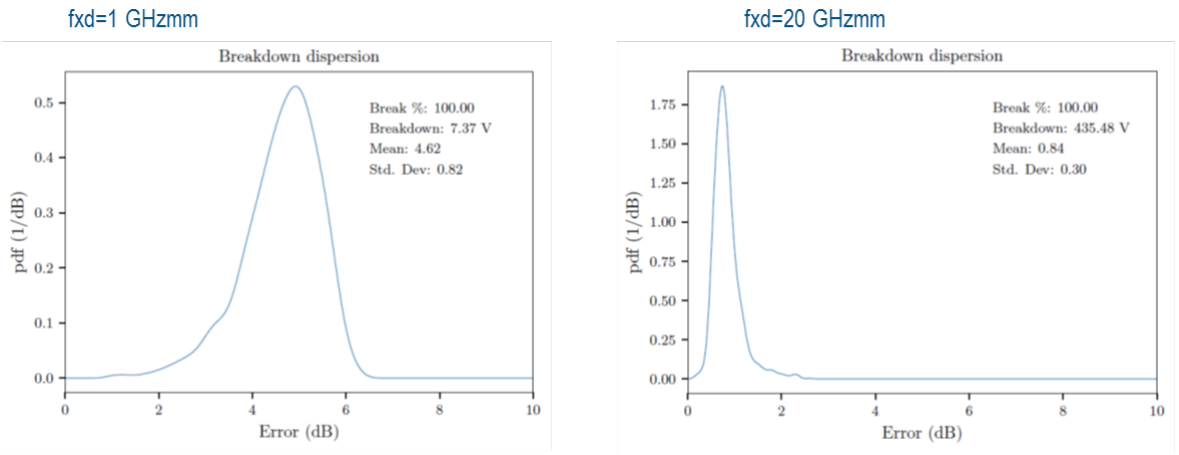


Figure 6-10: Error probability distributions for different *f·d*

From the distribution to the left, we can conclude that, on average, the error for random phase is around 5 dB whereas in the right case, the error is about 1 dB.

The two tables shown in Table 6-1 below summarize the statistics (mean and standard deviation values) of the error between the worst case and the simulated thresholds for all the considered parameters for silver and aluminium.

Table 6-1: Error statistics in dB for silver and aluminium, and different values of carriers, frequency band and fxd product

Material	ECSS Ag	ECSS Ag	ECSS Ag	ECSS Ag	ECSS Ag	ECSS Ag	ECSS Ag	ECSS Ag	ECSS Ag	ECSS Ag
Band	Ku	Ku	Ku	Ku	Ku	Ku	C	C	C	C
Carriers	4	4	10	10	10	10	10	10	10	10
fxd	1.1	22.2	1	1	20	20	1	1	20	20
Deltaf	50	50	50	100	50	100	50	100	50	100
Mean	1.92	0.37	4.62	3.11	0.84	0.68	3.02	2.28	0.69	1.29
StdDev	1.03	0.18	0.82	0.9	0.3	0.34	1.39	3.2	0.35	0.51

Material	ECSS Al	ECSS Al	ECSS Al	ECSS Al	ECSS Al	ECSS Al	ECSS Al	ECSS Al	ECSS Al	ECSS Al
Band	Ku	Ku	Ku	Ku	Ku	Ku	C	C	C	C
Carriers	4	4	10	10	10	10	10	10	10	10
fxd	1.1	22.2	1	1	20	20	1	1	20	20
Deltaf	50	50	50	100	50	100	50	100	50	100
Mean			4.59	4.19	1.17	0.93	3.48	2.12	0.7	1.24
StdDev			0.93	0.67	0.2	0.21	0.53	0.49	0.23	0.41

Table 6-1 shows that there is a general dependence with the *f·d* product.

The median value of the error is related to a factor called "similarity" which is formulated as follows:

Similarity coefficient = $\frac{fd}{T_e f N}$ GHz mm

Where f is given in GHz, Te in ns, d in mm and N is the number of carriers,

The dependency on the similarity degree is illustrated in the graph below:

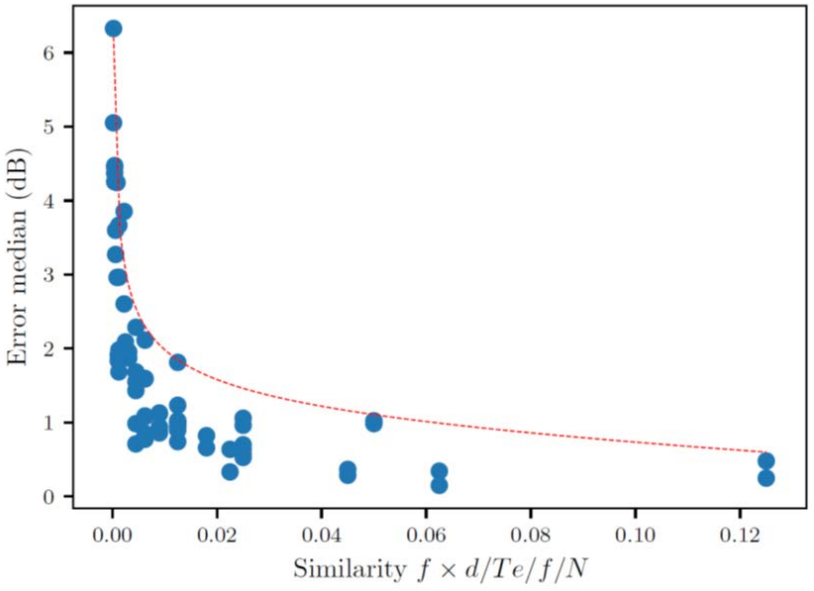


Figure 6-11: Error dependency on the similarity degree

From these data, we can apply the following approximation for the error:

$$y = ax^b + cx \qquad [6\text{-}1]$$

with the following parameter values:

a = 0,51

b = -0,29

c = -2,80

At this stage, the curve was produced by a specific study and is therefore used with relevant justification.

6.4.3.2 Multi-frequency test with a single carrier applying an equivalent power

The equivalent CW power definition enables to perform single carrier CW test in a representative manner compared to the multi-carrier realistic case.

The multi-carrier signal can be approximated in the time domain as a pulsed signal of duration T_{on} and amplitude V_{on}. The worst case (V_{on}, T_{on}) that yields the lowest Multipactor threshold voltage V_{mc} can be determined according to [6-2]. A summary is provided below.

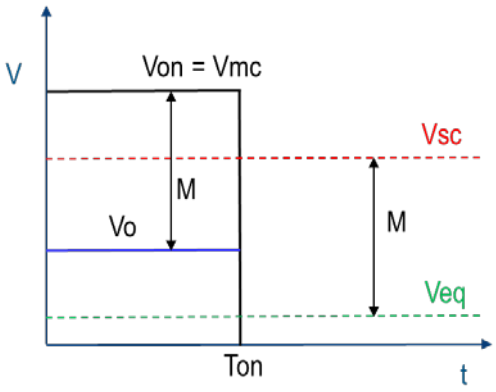


Figure 6-12: Margin definition with respect pulsed model and CW operation

The parameters in the figure are:

T_{on} = worst case pulse duration

V_{on} = multipactor threshold for the multi-carrier signal during ON time T_{on}.

V_0 = operational multi-carrier voltage

V_{eq} = equivalent single carrier voltage

V_{sc} = single carrier threshold voltage

M = margin between the operational voltage and the multi-carrier threshold

The equivalent single carrier voltage is the applied voltage V_{eq} in single carrier regime which yields the same margin M with respect to the single carrier threshold V_{sc}.

$$\frac{V_{sc}}{V_{eq}} = \frac{V_{mc}}{V_0} \qquad [6\text{-}2]$$

$$V_{eq} = V_0 \frac{V_{sc}}{V_{mc}} \qquad [6\text{-}3]$$

In terms of power, this translates to:

$$P_{eq,sc} = P_0 \frac{P_{th,sc}}{P_{th,mc}} \qquad [6\text{-}4]$$

where:

$P_{eq,sc}$ = equivalent CW power

$P_{th,sc}$ = single carrier threshold

P_0 = multi-carrier average operational power (sum of all carrier power values)

$P_{th,mc}$ = multi-carrier average threshold (sum of all carrier power values)

Note that for computing the equivalent CW power, it is needed to perform both single carrier and multi-carrier analysis.

Theoretically the multicarrier threshold power is bounded by:

$$\frac{P_{th,sc}}{N} \leq P_{th,mc} \leq P_{th,sc} \qquad [6\text{-}5]$$

This imposes a limit to the equivalent CW power:

$$P_0 \leq P_{eq,sc} \leq NP_0 \quad [6\text{-}6]$$

This boundary is imposed when computing the equivalent CW power.

Using [6-4] we can define an alternative to [6-6].

$$P_0 \leq P_0 \frac{P_{th,sc}}{P_{th,mc}} \leq NP_0 \quad [6\text{-}7]$$

obtaining:

$$P_{th,mc} < P_{th,sc} < NP_{th,mc} \quad [6\text{-}8]$$

This ends up in the following boundary definitions:

$$if\ P_{th,sc} < P_{th,mc}\ then\ P_{eq,sc} = P_0 \quad [6\text{-}9]$$

$$if\ P_{th,sc} > NP_{th,mc}\ then\ P_{eq,sc} = NP_0 \quad [6\text{-}10]$$

$$if\ P_{th,mc} \leq P_{th,sc} \leq NP_{th,mc}\ then\ use [6\text{-}4] \quad [6\text{-}11]$$

As an illustration, the example of the 5.3.3.2 can be used.

A numerical L2 analysis results in a single carrier threshold of:

$P_{th,sc}$ = 1421 W

The multi-carrier threshold obtained by the numerical analysis is:

$P_{th,MC}$ = 8 carrier x 181 W/carrier = 1448 W

Average operational power per carrier:

P_0 = 8 carrier x 45 W/carrier = 360 W

Option 1: The equivalent CW power is:

$P_{eq,sc}$ = 353 W

Since this value is lower than P_0 using [6-6] the resulting equivalent CW power is:

$P_{eq,sc}$ = 360 W

Option 2: in the illustration, the inequality [6-8] is not fulfilled. Consequently:

$P_{eq,sc}$ = 360 W

A margin is applied afterwards as required by the standard. For example, for an EQM component of P1 type, the margin would be of 6 dB.

6.4.3.3 Multi-frequency test with reduced number of carriers applying an equivalent power

With a reduced number of carriers, n, an equivalent scenario can be described as follows:

m is the operational number of carriers

and

n is the reduced number of carriers

It is now possible to define an equivalent CW single carrier power with [6-4] using m as well as n carriers. Since the equivalent CW power must be the same for both cases, the two calculations using [6-4] can be combined. The result is the following expression:

$$P_{0,mc,n} = P_{0,mc,m} \frac{P_{th,mc,n}}{P_{th,mc,m}} \qquad [6\text{-}12]$$

In other words, the margin for the operational case is defined as:

$$M = \frac{P_{0,mc,n}}{P_{th,mc,n}} = \frac{P_{0,mc,m}}{P_{th,mc,m}} \qquad [6\text{-}13]$$

Which after working out yields to the same equation as [6-12].

6.4.4 Pulsed testing

Multipactor tests are typically conducted using RF signals with adequate pulse width and repetition frequency. The pulse duration is selected to ensure sufficient electron seeding. The use of pulse widths shorter than 20 microseconds can mislead the results obtaining unrealistic higher multipactor thresholds [6-3].

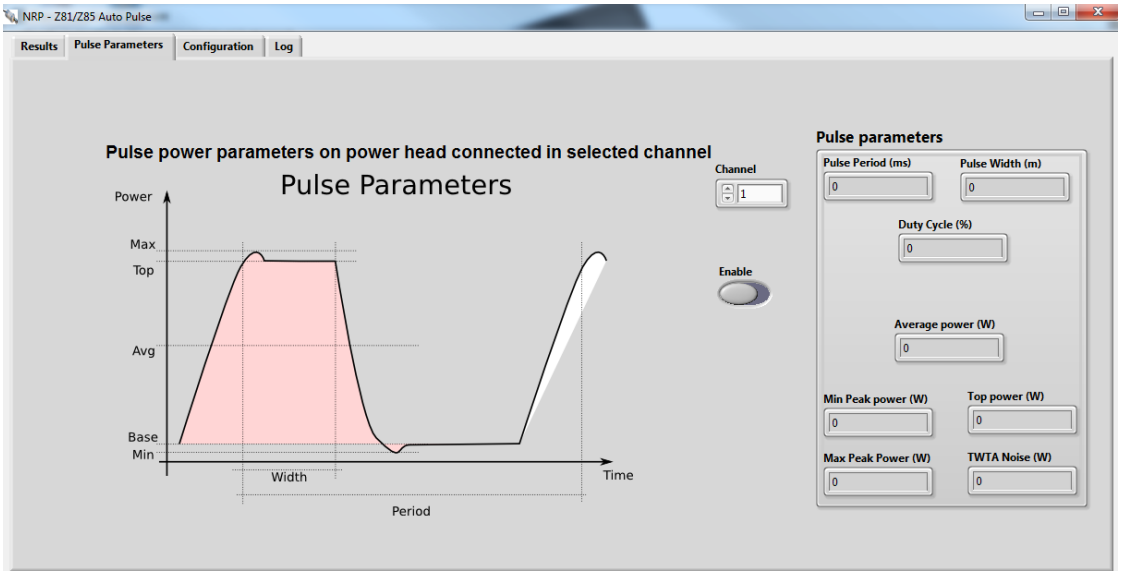


Figure 6-13: Typical pulse parameters during multipactor test

6.5 Electron seeding

6.5.1 General

No supporting material needed.

6.5.2 Multipactor test in CW operation

No supporting material needed.

6.5.3 Multipactor test in pulsed operation

No supporting material needed.

6.5.4 Multipactor test in multi-carrier operation

No supporting material needed.

6.5.5 Seeding sources

The importance of electron seeding depends upon the nature of the test (signal characteristics and Device Under Test).

6.5.5.1 Introduction

Electron seeding consists of introducing or producing a given electron population in the vicinity of the area of interest. These electrons simulate the actual contribution from the space radiations when the device is operating in real conditions. Diagnostic tests performed within ESA have shown that the number of initial electrons and their energy characteristics are decisive to obtain reliable data on the Multipactor threshold.

The purpose of this chapter is to summarize the most common techniques used for electron seeding during Multipactor tests. There are basically four methods to achieve a given electron population in the area of interest: radioactivity, photo-electric effect, controlled electron beam and electron probe. Depending on the topology of the device, one method can be more effective than the others. In any case, these techniques can be combined in order to improve the electron density in the area of interest. It is worth mentioning that once the minimum population of electrons is guaranteed inside the critical gap, an excess of electron population will not affect the breakdown threshold level.

6.5.5.2 Radioactive Source

6.5.5.2.1 Description

In nuclear physics, beta decay is a type of radioactive decay in which a proton is transformed into a neutron, or vice versa, inside an atomic nucleus. As a result of this transformation, the nucleus emits a beta particle, which is an electron or positron. The beta spectrum is a continuous spectrum.

For electron seeding purposes, radioactive beta sources which emit electrons are employed. The most popular isotope is Strontium-90.

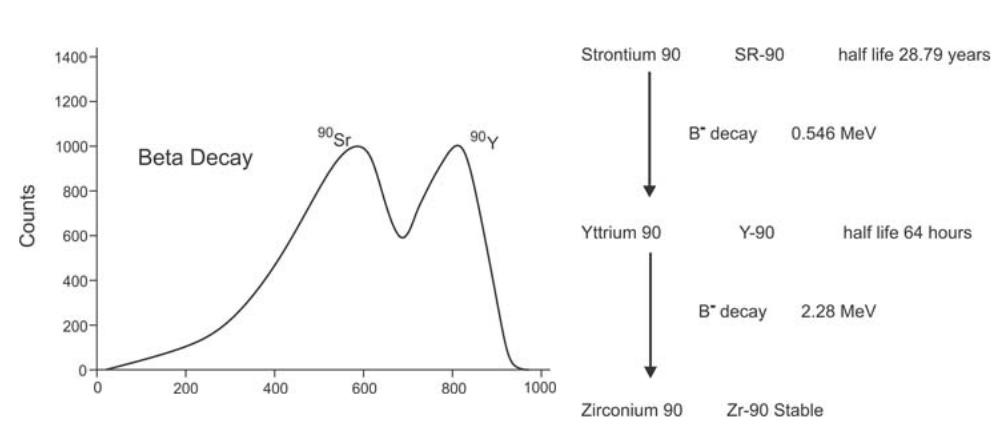


Figure 6-14: Decay of Strontium-90.

The radioactive sources used for testing purposes are encapsulated. They consist of an Aluminium cylinder with thick walls and a centered window, in order to focus the electron beam. They are constructed in such a manner that contamination of devices under test is not possible.



Figure 6-15: Picture of an encapsulated radioactive source.

6.5.5.2.2 Limitations

The use of radioactive sources is limited by two factors: the kind of material in which a device under test is manufactured and the wall thickness. The electrons coming from the source need to go through the component walls to reach the critical gap. Due to the interaction with matter, the electron population is reduced or even totally extinguished in the area of interest. For example, the activity measured from 37 MBq Sr90 source through a 2 mm thick Aluminum sheet decreases roughly 70 % with respect to the same configuration without the Aluminum sheet. This issue can be resolved if the device has direct access to the critical gaps through, for example, venting holes.

Table 6-2: Rate and energy of injected electrons going through a particular aluminium wall [6-4].

Wall thickness (mm)	Rate (electrons/s)	Energy (MeV)
0,1	$4{,}24 \times 10^5$	2,6
0,5	$2{,}46 \times 10^5$	1,95
1	$1{,}75 \times 10^5$	1,7
4	9×10^3	0,48
6	0	0

The recommendation is not to use thickness beyond 1 mm as the electron seeding will not be effective.

6.5.5.2.3 Advantages

- A radioactive source can be used with any type of component. If there is any obstacle, the electrons can pass through, provided it is not too thick [6-4]. If possible, it is advisable to reduce its thickness.
- The source acts directly on the critical gap.
- It can also be used in the intermediate pressure range (for Corona applications).

6.5.5.2.4 Disadvantages

- The maximum energy of the injected electrons is in the order of MeV. The secondary electron yield of most materials at such energies is quite below unity, and therefore a vast number of injected electrons are absorbed.
- The electron flux and energy are not regulated.
- The rate of electron seeding is poor compared to other methods, such as the REG or the UV lamps.
- The radioactive nature of the source makes it dangerous and difficult to manipulate. It needs to be stored in a special fire-resistant container. Only trained operators are allowed to use it.
- The solid angle characteristic of the source is known in order to ensure that the source is sufficiently close to the DUT to assure proper seeding of the critical areas.
- The radioactive source used needs to be within its half-life period of maximum activity to become effective.

6.5.5.3 UV Lamps

6.5.5.3.1 Description

The photoelectric effect is produced when light (photons) illuminates a metallic surface, and electrons from this surface are extracted as consequence electrons emitted in this manner are called photoelectrons.

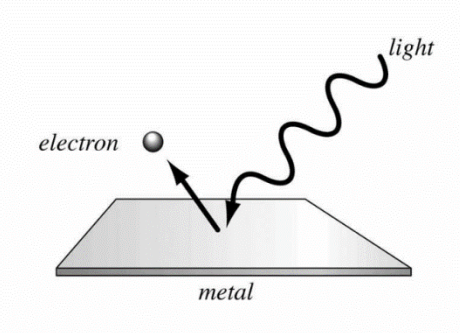


Figure 6-16: Sketch of the photoelectric effect.

The production of photoelectrons depends on the type of illuminated material. For a given metal, there exists a minimum frequency of incident radiation below which no photoelectrons are emitted.

The UV (ultraviolet) light is introduced in the vicinity of the critical gap by means of an adequate optical fibre. If the device is enclosed, venting holes or any other access way are required. The inner walls of the device are then illuminated, producing photoelectrons in the area of interest.



Figure 6-17: Picture of the UV lamp as part of a test bed.

There are several types of lamps that can be used. When choosing a lamp, it is important to consider the wavelength, light intensity, stability level, and life expectancy needed in the application. The required wavelength range often narrows down the lamp choices. This range matches the work function of the illuminated material.

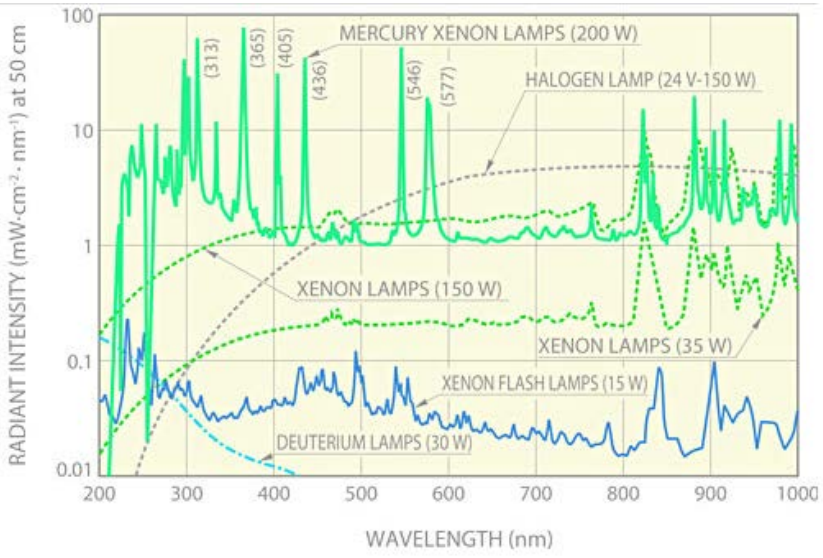


Figure 6-18: Spectrum of the typical lamps used for electron seeding.

6.5.5.3.2 Advantages

- The UV source can be used with any type of component with adequate access to the critical gap.
- High electron production are created directly from the inner walls at the right electron energies.
- The rate of electron seeding can be easily controlled (varying the light beam intensity).
- It can be switched on and off without opening the vacuum chamber.
- Multiple optical fibres system allows simultaneous electron generation over several areas of a large component.
- It is not dangerous and is easy to set-up. However, adequate eye protection is necessary.

6.5.5.3.3 Disadvantages

- It is an invasive method. It needs to penetrate into the device. In closed components, existing venting holes can be used.
- Depending on the point of insertion, if the optical fibre does not illuminate directly the critical gap region, the electrons can be produced outside of the multipactor region. In such cases, the seeding is only effective if the electrons spread towards the critical gap.
- A certain UV lamp is valid only for materials with work-function below its photon energy (electrons are generated only if the photon energy is higher than the work function of the material).

6.5.5.4 Electron Gun

6.5.5.4.1 Description

Electron guns produce a collimated electron beam of a precise kinetic energy. With this seeding method, a good control of the electron flux and energy is achieved.

Basically, the electron gun consists of a tungsten filament, a Wehnelt cylinder, electrostatic lenses, an iris and an anode.

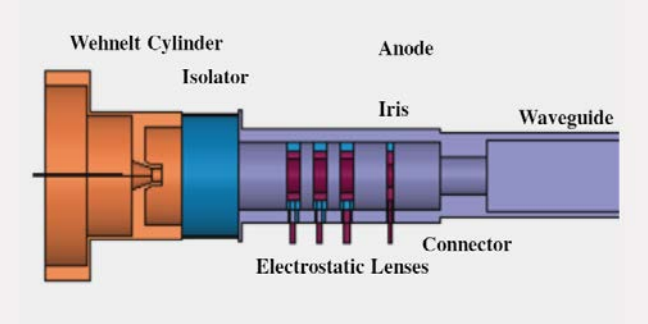


Figure 6-19: Diagram of an electron gun.

When a piece of metal is heated by the Tungsten filament wire connected to a low voltage (produced by the Wehnelt cylinder), electrons escape from its surface. Some electrons (the conduction electrons) are free to move in the metal, thus they gain kinetic energy. Some of them gain enough kinetic energy to escape from the metal surface, forming an "electron cloud".

If the hot metal plate is under vacuum conditions, then the evaporated electrons are free to move. The electrons can be pulled away from the hot surface of the plate by putting a positive electrode (anode) nearby. The anode is created by connecting an electrode to the positive terminal of a power supply, and the hot plate is connected to its negative terminal. The hot plate is then the cathode.

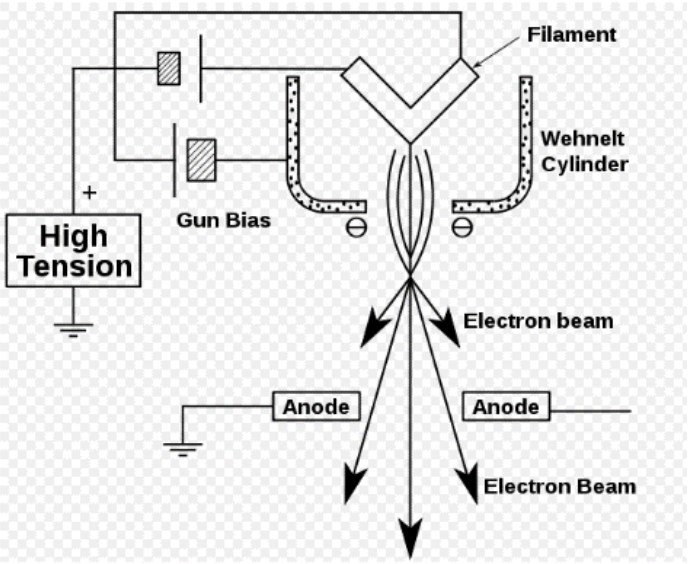


Figure 6-20: Sketch of the functioning of an electron gun.

As soon as the electrons evaporate from the surface of the hot plate, they are pulled towards the anode. They accelerate and crash into the anode. However, if there is a small hole in the anode, some electrons will pass through, forming a beam of electrons that came from the cathode. This cathode ray can be focused and deflected. It carries small currents.

Using the electron gun, it is possible to select the energy of individual electrons (typically from 20 eV to 1000 eV) and the electron density inside the gap.

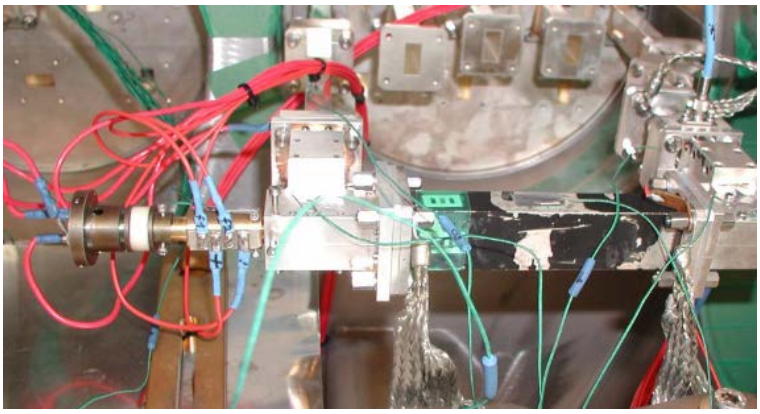


Figure 6-21: Picture of an electron gun installed into a test bed.

The electron gun is installed close to the DUT, focusing the critical gap, but it is not always easy or even possible. The gun points directly to the critical gap in order to generate a proper seeding. In fact, it is difficult to achieve a proper alignment of the electron beam, especially for very small gaps. A pointing laser beam can be used to fine-tune the position of the electron gun.

6.5.5.4.2 Advantages

- Good control on electron flux and energy.
- Its manipulation is not dangerous.
- If a Faraday cup is mounted at the other side of the beam, it can be used as an extra multipactor detection method.

6.5.5.4.3 Disadvantages

- The electron gun is bulky and its access to DUT can be complex. Thus, it can be far away from the critical gap or misaligned. In waveguides it is only possible to seed from the ports.
- It can be used only in devices with direct line of sight to the critical gap.
- It is difficult to install close to the Device Under Test (DUT).
- For calibration and operation purposes, high vacuum is needed.
- In waveguides, it requires RF compensated bends and extra elements in the set-up, which implies extra complexity and difficulty.
- The calibration process can be tedious, particularly for very small gaps.
- In coaxial structure, it cannot be used.

6.5.5.5 Guidelines for the use of seeding sources

6.5.5.5.1 General recommendations

The use of combined seeding methods where at least one of them provides low energy electrons (for example UV light source) is recommended in order to achieve the lowest Multipactor threshold [6-5].

6.5.5.5.2 Use of Radioactive β source

- Determination of the electron seed rate is performed by measuring the source activity and then computing the low energy yield rate.

NOTE The thickness and nature of the material between the electron source and the critical areas is relevant. The electrons can have insufficient energy to penetrate the material.

- In the presence of any obstacle between the RS and the critical gap, due to the loss of energy and electron seeding flux, the obstacle thickness is reduced to at least 1 mm (depending on the material characteristics).

  NOTE Smaller thicknesses increase the electron flux at the critical gap.

- The radioactive source is placed not more than 5 cm far from the critical gap of the DUT where multipactor is expected to occur.

  NOTE This is in order to radiate the walls with maximum field.

  NOTE It depends on the solid angle of the electron emission.

- The radioactive source incorporates a method to block the radiation by switch on and off the source.

  NOTE This is for safety reasons, since it is desirable to have a radioactive source with an activity as high as possible (at least 1 mcurie, i.e. 37 MBeq).

6.5.5.5.3 Use of UV light

- When using UV light as seeding source, photons have direct access inside the component under test in the vicinity of the critical gap.
- When using UV light as seeding source, in waveguides and other closed devices, if there is a direct line of sight from the port to the critical gap, the optical fibre is inserted at the input ports, oriented along the direction of propagation (typically referred as z-axis).
- When using UV light as seeding source, the lamp intensity is regulated to ensure the maximum electron seeding flux.

6.5.5.5.4 Use of regulated electron gun (REG)

- When using a REG as seeding source, ensure access inside the component under test and used only in circuits with direct line of sight to the critical gap.

  NOTE If there is any obstacle the electron beam does not reach the gap.

- When using a REG as seeding source, it is calibrated so that the solid angle of the beam covers the whole critical gap.
- When using a REG as seeding source, calibration of the beam energy is as follows:

  1. If the electron beam impinges directly on the critical gap surface, set the energy of the electrons to maximize the secondary emission yield (SEY) at the gap surfaces.
  2. If the electron beam passes through the gap, parallel to the surfaces, calibrate the energy of the electron beam to maximize the number of electrons impinging the critical gap.

  NOTE One of the above mentioned two cases can occur depending on the geometry, as explained below:

  - The first case is common in open components, such as planar structures, where the beam can access directly the gap. This guaranties that the maximum number of electrons is generated. The energy necessary depends on the SEY properties of the gap material.
  - The second case occurs for example in waveguide based structures, where the beam is fed from the ports. In this case, only the electrons

deflected from the straight line will impact with the gap surfaces. This is necessary because if the electron energy is too low, electrons can be unable to reach the critical gap. If it is too high, they can pass through the critical gap with no interaction.

- When calibrating the REG energy, it is increased in successive steps during the test until the optimum beam energy which minimizes the breakdown threshold is obtained.

6.5.5.5.5 Use of a charged wire probe

- When using a charged wire probe as seeding source, ensure direct access to the critical gap inside the device under test.
- When using a charged wire probe as seeding source, the pressure in the vacuum chamber is below 10^{-4} Pa.

NOTE 1 This is to ensure constant emission of electrons from the wire.

NOTE 2 The lower the pressure in the chamber the higher is the emission stability.

6.5.6 Seeding verification

See section 8.3.1 for examples of reference samples.

6.6 Bibliography for clause 6

[6-1] Standard/Handbook for Radio Frequency (RF) Breakdown. Aerospace report No. TOR-2014-02198.

[6-2] Long-term multipactor discharge in multicarrier systems. Sergio Anza, Carlos Vicente, Benito Gimeno, Vicente E. Boria, and Jaime Armendariz. Physics of Plasmas, Aug. 2007.

[6-3] Experimental Analysis of the Multipactor Effect With RF Pulsed Signals, D. González-Iglesias, O. Monerris Belda, M. E. Díaz, B. Gimeno, V. E. Boria and D. Raboso. IEEE Electron Device Letters, Vol. 46, No 10, October 2015.

[6-4] Influence of RF component wall thickness in electron seeding in multipactor testing. L. laura, J.J. Garcia-garrigos, D. Raboso, B. Gimeno, C. Belver-Aguilar, V. Boria and A. Faus, MULCOPIM Workshop 2011.

[6-5] Effect of free electrons in Multipactor threshold, D. Raboso, C. Miquel-Espanya, A. Allstaff, B. Gimeno, M. Baumann, U. Wochner and M. Taroncher, MULCOPIM Workshop 2008.

7
Multipactor - Methods of detection

7.1 General

7.2 Detection methods

7.2.1 Introduction

This chapter describes the detecting methods that can be used for Multipactor testing. The last clause of this Annex specifically addresses the techniques used for the detection of transient Multipactor, as can be produced in a multi-carrier environment.

The test methods included in this chapter rely on the effect that Multipactor has the following characteristics:

- Close-to-carrier noise;
- Phase nulling;
- harmonic noise.

The above are global methods in the sense that the effects can be detected at convenient locations remote from the Multipactor region. In addition to these, two local methods of detection, namely optical and electron density, are considered in the chapter.

The global methods have been proven to be effective in single carrier CW/pulsed operation. However, in those test scenarios, where broadband signals and modulated signals both for single and multicarrier schemes are used, additional precautions are taken for the suitability of the detecting methods.

7.2.2 Global detection methods

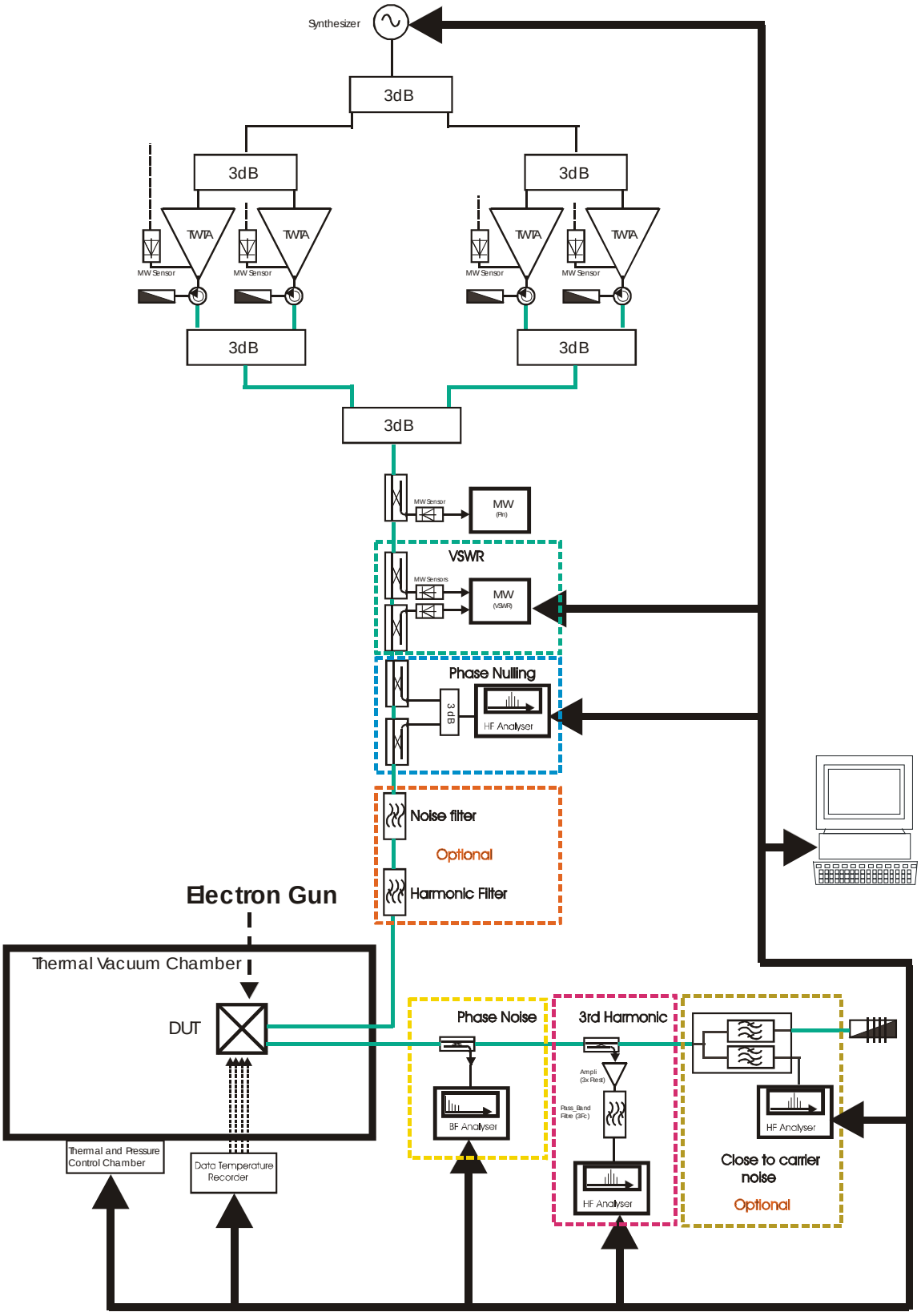


Figure 7-1: Schematic of global detection systems implemented in a typical test bed.

7.2.2.1 Close to carrier noise

This detection method consists in observing changes on the spectrum at a frequency close to the carrier, that is to say 100 or 150 MHz far from the signal. This method requires a high sensitivity level of the sub-assembly, composed of the rejection filter, the LNA and the spectrum analyzer.

The advantages of this method are the following ones:

- In certain circumstances, this method can be characterized by a high sensitivity level

The disadvantages of this method are the following ones:

- The rejection filter of the nominal carrier is specified, designed and manufactured for each test, depending on the frequency of the nominal carrier,
- The LNA and the spectrum analyzer are compatible in order to guarantee a minimum of sensitivity.

7.2.2.2 Phase nulling

In this detection system a proportion of transmitted and reflected power is coupled into a phase- and amplitude-matching network. Once the system is balanced the two signals produce a null, which is very sensitive to amplitude and phase variations within the system.

A multipactor discharge creates an imbalance and a loss of the null.

A reference signal is coupled from the incident power and applied to the nulling hybrid. The reflected power from the DUT is coupled and also applied to the hybrid. A nulling condition is adjusted with a phase-shifter and a variable attenuator. The null-depth can be monitored on the spectrum analyser.

The spectrum analyser span and resolution bandwidth settings depend on the signal characteristics.

When performing a multi-carrier Multipactor test, at first the phase conditions of all carriers are adjusted until the well-known peak-voltage envelope signal is obtained.

In a second step the spectrum analyser is tuned to the centre channel of all applied channels. Then the nulling can be performed, starting with the phase adjustment, until the maximum null-depth is obtained.

NOTE A disadvantage of this method is that, due to changes in temperature of the DUT and the test bed, an optimum null can be achieved only by frequently retuning the system.

7.2.2.3 Harmonic noise

The detection of noise at the third harmonic of the carrier frequency has often been used for Multipactor testing.

This detection method is one of the most reliable detection methods in use and works because a discharge spreads energy over the spectrum, resulting in increased power in the harmonics.

For optimum operation, the harmonics generated by the HPA need to be filtered out. Good coupling of the generated harmonic components is also required.

If the DUT is filtering the signal at the third harmonic frequency, the sensitivity of this method can be degraded.

NOTE The use of second harmonic as detection method is not always recommended due to the high level of residual harmonics along the RF path coming from the microwave amplifier and other non-linear components. This reduces the sensitivity of the detecting method.

7.2.3 Local detection methods

7.2.3.1 Optical Method

The optical detector consists of a UV-transmissive quartz fibre optic mounted in the centre of the sidewall of a waveguide bend. The bend is directly attached to the test piece so that the fibre's field of view is along the length of the test piece, monitoring the reduced height centre section. The light generated by the discharge is predominantly UV; this is detected by means of a photomultiplier tube located outside the chamber operating in the UV region.

The tube and its housing are placed inside a metal box to reduce the light leakage into the tube itself and increase the sensitivity by reducing the dark current.

Although the tube itself has a fairly fast rise time of approximately 4,5 ns, it has a slow initial response time (delay); the difference in response time between the tunnel diode detectors and the optical detector is of the order of hundreds of ns, depending upon the loading of the tube output.

For this reason, the global detecting methods are used as the principal discharge intensity diagnostics and the optical emissions are used as an auxiliary indication.

7.2.3.2 Electron probe

The rapid increase in the charge density at the onset of Multipactor can be used to provide diagnostic information. To monitor the electron density within the wave guide, a small probe biased at 60 V is introduced into the waveguide on the centreline of the narrow wall. An electronmeter is then used to monitor the current as an indication of the electron density. This form of detector is inherently slow because of the rise time associated with the amplifier circuit.

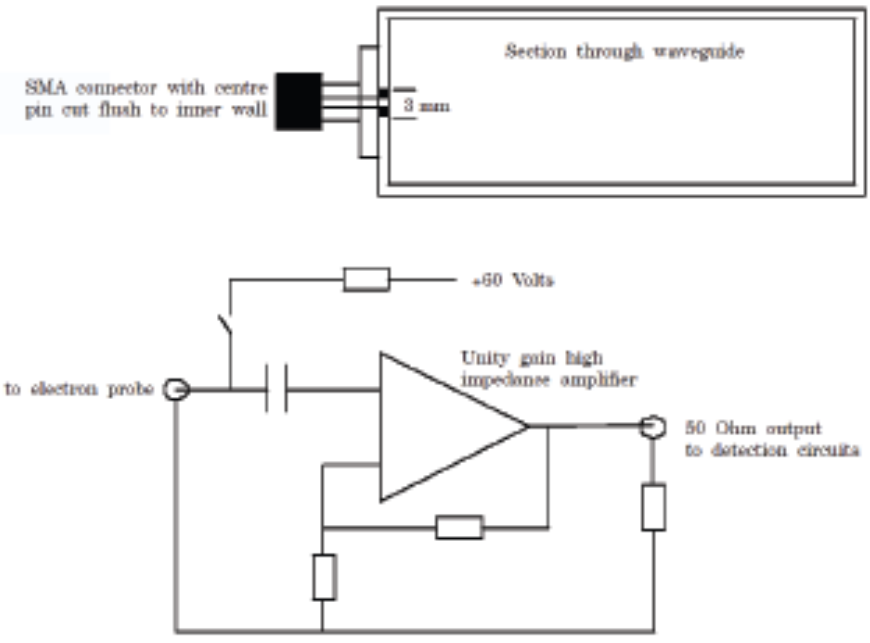


Figure 7-2: Electron probe circuit diagram.

7.2.3.3 Mass spectrometer

A mass spectrometer is sometimes used as a diagnostic tool rather than a detector for Multipactor due to its slow response time.

7.3 Detection method parameters

7.3.1 Verification

See 7.2 and 8.3.1for descriptions of detection methods and reference samples respectively.

7.3.2 Sensitivity

No supporting material needed.

7.3.3 Rise time

No supporting material needed.

8
Multipactor - test procedure

8.1 General

Table 8-1: Example of Multipactor Test Specification Sheet

DUT description	
DUT type of component	L band bandpass filter
Reference/Model/Serial number	E3.2/UVR, SN001
Manufacturer	XXXX
Plating	Silver
Operating frequency band	1,4-1,6 GHz
DUT handling precaution	BB, EM, EQM, PFM, FM
DUT overall dimensions	20x20x35 cm
DUT overall weight	200 g
DUT port interfaces	Female TNC connectors
Test requirements/information	
S-parameter measurements	Full port analysis to make sure that the upper frequencies measurements of S parameters cover the third harmonic frequency. Measurement of the complex S parameters over the frequency range[XX].
Test frequency	1,4 GHz
Expected Multipactor critical area	Between stripline and outer conductor immediately above and below stripline
Maximum power (W)	Test to maximum available test power
Pulse width	20 µs
Duty cycle	2%
Thermal vacuum requirements	
Bake-out (T°C, duration h)	80°, 12h
Temperature during test (at TRP)	-40°/+90°
Aborting temperature at TRP	+110°
Thermocouple locations	reference figure of the DUT
Maximum pressure	10^{-5} hPa
Minimum time under vacuum (including bake-out) prior test	14h

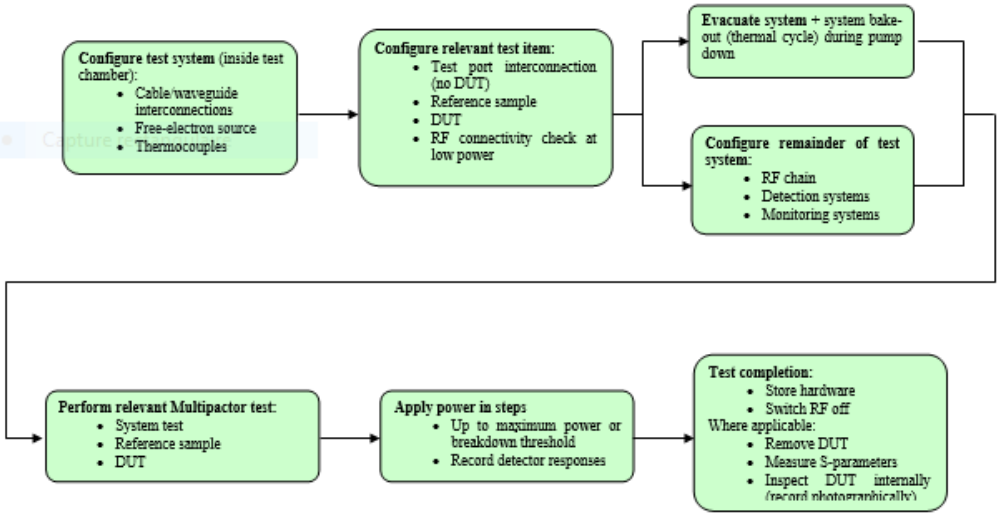


Figure 8-1: Multipactor test procedure overview.

8.2 Test bed configuration

No supporting material needed.

8.3 Test bed validation

8.3.1 Reference multipactor test

8.3.1.1 Example of L- and S-band reference sample

The design presented in this section is a broadband coaxial stripline design, based on samples designed and successfully tested. The multipactor region extends over the length of a 50 ohm coaxial line that consists of a relatively wide strip line centre conductor, symmetrically positioned between the ground planes which are the main body of the sample - refer to Figure 8-2. The stripline-cavity dimensions approximate sufficiently well to represent a parallel-plate geometry, consequently allowing a relatively simple calculation of the multipactor threshold for a known test frequency and gap size.

This type of sample has been measured and shown to have a broadband response from 1 GHz – 4 GHz, thus potentially allowing multipactor measurements to be made over a frequency-gap product of about 1,18 GHz·mm to 4,74 GHz·mm, allowing a wide coverage of the 1st and 3rd mode order multipactor zones. This sample is also of interest as it covers this intermediary zone between the 1st and the 3rd mode order zones.

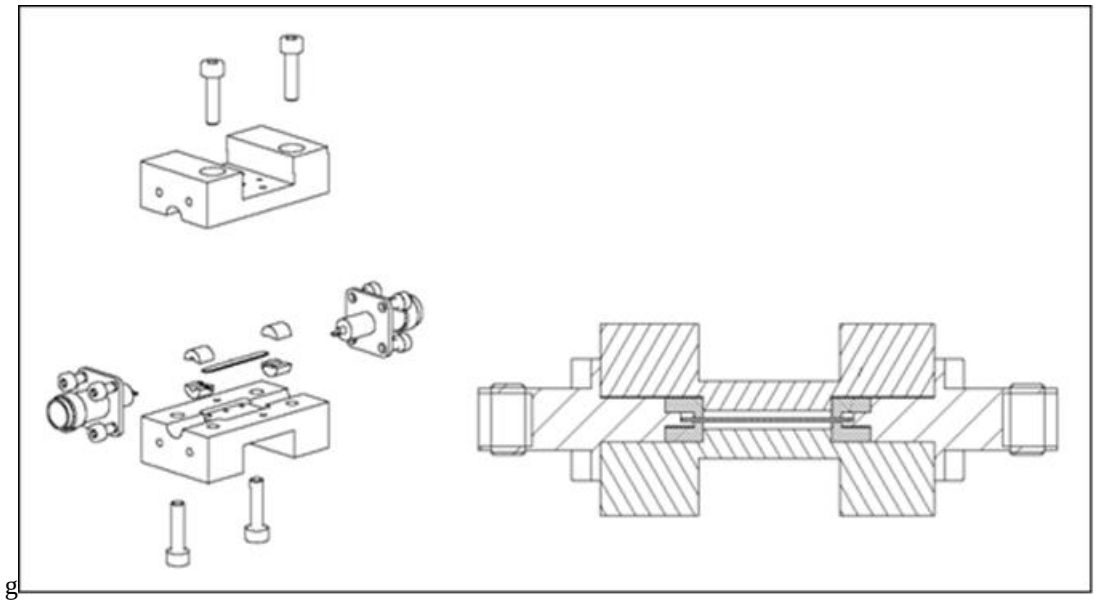


Figure 8-2: Example of an L- and S-band reference sample.

For a frequency gap of 1,8 GHz·mm, it can be seen that the threshold is situated between mode orders 1 and 3. Consequently, it is of interest to determine the threshold by measurement and simulation to determine whether hybrid modes are present or not depending on their stability.

The sample has a simple construction, consisting of two identical body halves that enclose the central strip line length, which has a 50 Ω impedance. The strip line is soldered at each end to the centre pins of the input and output TNC connectors. At the junction of the TNC pin and the strip line, the outer conductor has been stepped to compensate the discontinuity and provide a wideband match at this transition. This region is also filled with PTFE to avoid any multipactor breakdown at the corner discontinuities. The central strip line also has chamfered edges to reduce any field enhancement which can lower the multipactor threshold compared to the parallel plate predictions.

Venting holes are provided in both halves of the body to ensure that the pressure inside the sample is very similar to the vacuum chamber environment and also to allow seed electrons to enter the discharge region from the chamber environment (i.e. from a radioactive or free-electron source). The design has been modified to have a reduced thickness of sample wall which acts as a “window” for beta particle radiation penetration – the “window” is of the order of 0,5 mm to 0,8mm thick.
The sample body and strip line conductors can be plated as required.

Figure 8-3 shows the measured S-parameter performance of the current baseline design up to 6 GHz.

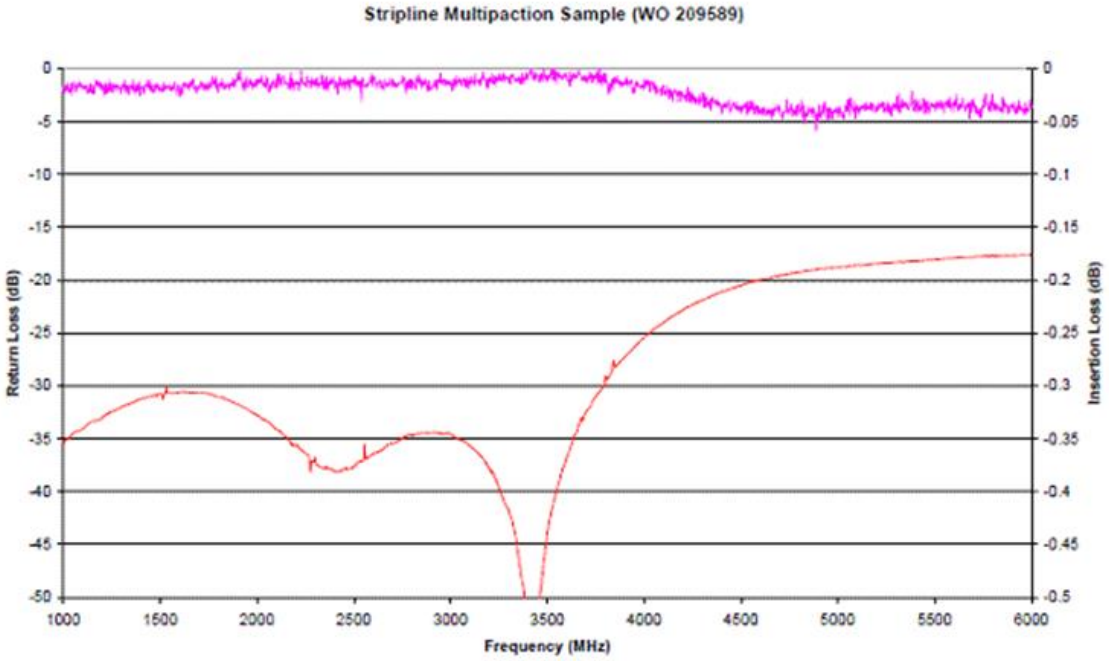


Figure 8-3: Measured S-parameter performance of broadband multipactor sample.

8.3.1.2 Example of Ku-band reference sample

The broadband reference sample design is based on well-known multipactor samples, composed of symmetric cascaded waveguide transitions. Using a stepped profile, the waveguide section is changed from a standard cross section at the sample interfaces, to a reduced cross section (with respect to the smaller waveguide dimension) in the middle. With a sufficient thin dimension, the multipactor phenomenon is likely to occur for lower power in the central zone.

This geometry allows a good return loss over a wide bandwidth. Figure 8-4 shows the outline of the component:

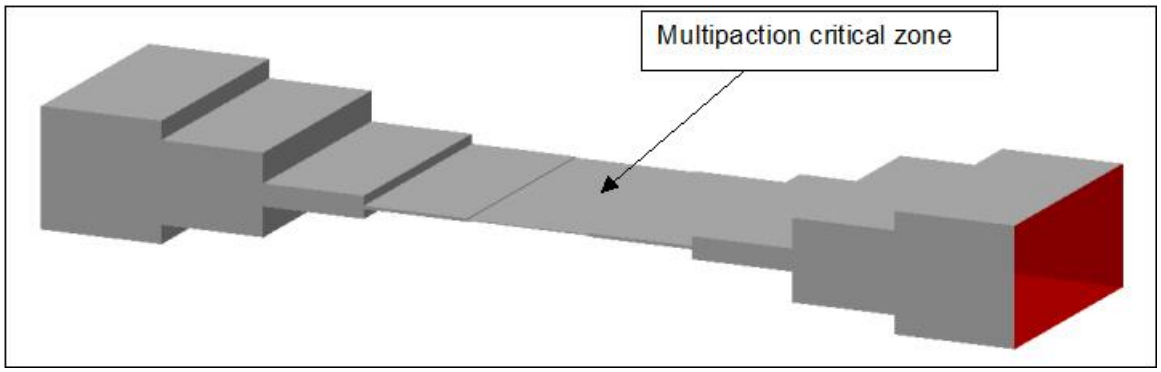


Figure 8-4: Ku-band Broadband Multipactor Sample.

Ensure that the critical gap determination is compliant with the maximum power available of the test bed in order to have a component with an achievable Multipactor threshold.

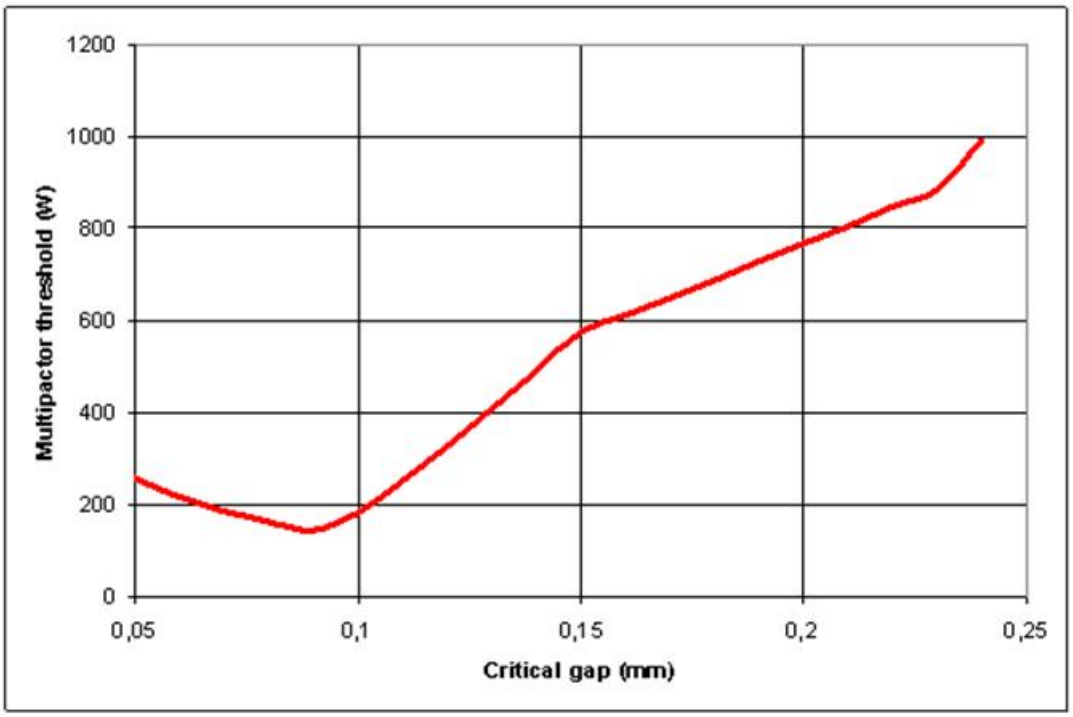


Figure 8-5: Multipactor threshold variation vs. gap height.

As machining tolerances have a more pronounced effect on small dimensions, the critical gap is not to be too small. The choice of 0,1 mm is a good compromise.

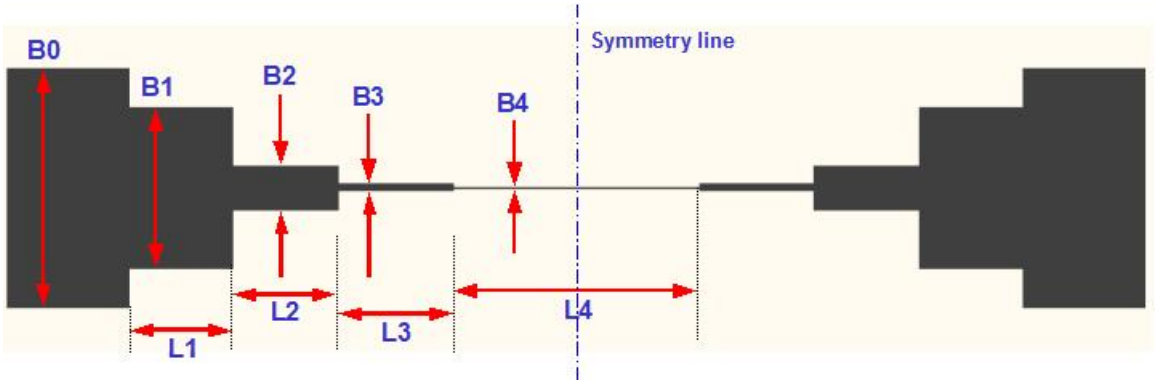


Figure 8-6: Ku-band reference sample dimensions.

For radioactive seeding effectiveness, the Ku band design includes a "window" with a reduced metal wall thickness. In the case of the Ku band transformer, the wall thickness at the level of the gap (B4 section in the figure above) is of 0,8 mm. In that case, the radioactive source is effective.

8.4 Test sequence

8.4.1 Power profile

Typically, if the electron seeding has proven effective, the dwell time is set to 10 minutes per step, as minimum, regardless the duty cycle or pulse width. The power is increased in 1 dB steps from the start of the test to the RF power corresponding to Pmax-3 dB. Then, the power is increased in 0.5 dB steps from Pmax-3 dB until the maximum RF power is reached.

It is also recommended to increase the dwell time at critical power levels such as the nominal operational power and the maximum applied power. These new dwell times are typically in the order of one hour.

8.5 Acceptance criteria

8.5.1 Definitions

No supporting material needed.

8.5.2 Multipactor Free Equipment or component

No supporting material needed.

8.5.3 Steps in case of Discharges or Events during test

No supporting material needed.

8.5.4 Investigation of Test Anomalies

During the Multipactor test, any unusual variation observed in the environmental monitoring results such as sudden spikes in the pressure curve or/and unexpected temperature changes will have to be investigated during the post-validation exercise of the test bed to determine the cause of these anomalies and possibly discriminate them from the actual DUT.

8.6 Test procedure

8.6.1 Test procedure for high power loads

8.6.1.1 Introduction

This chapter proposes a testing procedure for high RF power loads to be operated in high vacuum. Two verification processes are described depending on the cooling system used in the load.

8.6.1.2 High power load description

Designing a high RF power load to be operated in high vacuum presents two major challenges. This first one consists in choosing the right RF absorbent with low outgassing properties [8-2] high RF attenuation [8-3] and low VSWR. The second one is related to the way in which the heat is removed

from the load. Two approaches exist: liquid cooling and conduction cooling. Because of the vacuum conditions, only conduction and radiation can be used to transfer the heat away from the load's core.



Figure 8-7: Heat pipe.

The non-liquid cooled loads used inside the satellite are design to be operated up to 300 W CW and are typically cooled by means of conduction with other satellite parts which are cooler, such as heat pipes filled with ammonia or the case of the satellite. These loads are constrained by the fact that cooling is achieved by means of passive methods with no electric power consumption. The heat pipes (Figure 8-7) operate with no electric power, nearly isothermally, and transfer heat all along is route. By spreading the heat and increasing the radiation area it is possible to sufficiently cool down the load. These loads are not -usually- suitable to replace the antennas on a satellite TVAC test as the total power is much higher.

The liquid cooled loads withstand RF power levels in the range of thousands of watts per load. These loads are design assuming that there is no electric power constrains in order to dissipate the heat on the load. The coolant might be water or any other liquid with better thermal conductivity at high and low temperatures. The satellite TVAC test temperature range is taken into account when selection the coolant if the loads are not thermally isolated from the satellite inside the TVAC.

Any of the two types of loads is provided with enough venting holes to allow the interior of the device to reach high vacuum in a reasonable time (a few hours). Additionally, the outgassing of the materials, when the RF power is applied, is taken into account when designing the venting holes (number and size) to avoid the initiation of a corona discharge. Venting holes are designed to allow the venting of the unit by its own means.

Finally, damage on satellite RF path is prevented in case of a total destruction of the load during the TVAC. For this purpose, on waveguide loads, a pressure window at the input port of the load is highly recommended to keep the debris inside the load in case of deflagration. Note that this pressure window will retain the gas and debris inside the load.

8.6.1.3 Recommended RF power margins

The recommended power margins include two different ranges. The highest RF power is applied, at least, to one sample load out of the entire batch. The lowest RF power can be applied to the other loads on the batch. A batch of loads is considered to be all the units made from the same materials produced at the same time using the same manufacturing process. Do not select two loads of the same model and manufacturer of the same batch if they do not meet this parameter.

With P_{nom} being the TVAC RF power in dBm, the test maximum RF power level is any level between the minimum and maximum RF power levels defined in Table 8-2.

Table 8-2: Maximum RF power applied to the load range (margin in bold).

	Max. RF power (minimum)	Max. RF power (recommended)
Sample load (One load per batch)	P_{nom} (dBm) + **2 dB**	P_{nom} (dBm) + **3 dB**
Rest of the batch	P_{nom} (dBm) + **0,8 dB**	P_{nom} (dBm) + **2 dB**

8.6.1.4 Test bed

The test bed used for the validation of the high RF power loads is as representative as possible of the frequencies and number of carriers on the DUT operation or TVAC test. Single carrier testing is accepted although multicarrier testing is preferred as it is most representative from the RF field distribution point of view. The RF power for all the RF channels is similar to each other unless its final test procedure in the TVAC states it otherwise.

The measurement of the RF power is accurately done by means of calibrated RF equipment. Wideband power sensors covering all the channels are used (typically thermal power sensors). Arc detectors are used to prevent damage on the test bed in case of failure in the DUT.

The RF power generation is tripped out in case of a failure on the load or failure in the external cooling unit.

8.6.1.5 Test procedure for liquid cooled loads

8.6.1.5.1 Test sequence

The test sequence for a high RF power load includes:

1. Measurement of the scattering parameter before and after the power tests.
2. Preliminary bake-out of the units in an oven (ambient pressure).
3. Coolant over pressure test.
4. Leak test on the liquid connections.
5. Verification of the security systems: ARC detector, cooling system monitoring...
6. Temperature measurement devices installation (thermocouples, pt-100, fibres...).
7. Ambient test up to the maximum RF power.
8. RF Power test at high vacuum.
9. Tap test.

8.6.1.5.2 Scattering parameters

The scattering parameter (S11) of the load is verified before and after the test to ensure no degradation on its RF performance due to high RF power testing.

8.6.1.5.3 Preliminary bake out

When the loads have been stored for a long period of time in non-controlled conditions it is recommended to perform an ambient pressure bake-out before installing them in the TVAC. The loads are placed inside an oven and heated for more than 60 minutes at a temperature above 80 °C. This will remove most of the water content in the RF absorbent. This process is done in a clean room.

8.6.1.5.4 Overpressure test

The coolant compartment is filled up with a higher pressure gas (air, nitrogen or helium) than under nominal operation. No deformation on the cooling liquid compartments is observed.

8.6.1.5.5 Leak test

Once the coolant connection is set up, a leak test is carried out. The most convenient approach is to use a He leak detector and fill the pipes with helium. No leak is detected at any join of the circuit.

8.6.1.5.6 Temperature measurement

Temperature data in several points of the load is recorded during the RF test sequence. The measurement points cover, at least, the more critical areas of the load (to be provided by the manufacturer), the temperature of the coolant at the input and output connections and the pressure window.

8.6.1.5.7 Verification of the security systems

Once the load has been installed in the vacuum chamber the security systems are manually triggered in order to verify its correct performance. A failure of the DUT during the test represents a high risk for the test bed.

8.6.1.5.8 Ambient pressure RF power test

Prior starting the vacuum system the load has to be properly connected inside the vacuum chamber. An ambient test up to the maximum RF power is conducted in order to verify all the parameters. The RF power is applied progressively for no less than 15 minutes. Once in the maximum RF power a plateau of 15 minutes is maintained to ensure thermal stabilization.

8.6.1.5.9 RF power test at high vacuum

The test sequence in high vacuum vary according to the TVAC specifications nevertheless, in any case, a first power ramp up to maximum RF power is conducted starting from very low RF power. This active out-gassing stage lasts as long as needed in order to avoid excessive pressure increase due to outgassing and excessive temperature on the load.

Temperature cycling is adjusted, if required, to cover the temperatures that the load will reach during the TVAC test. The temperature in the coolant is kept at the set temperature and temperature cycles are achieved by means of an independent thermal bath. It is most likely that the load will remain at a constant temperature, despite of the effect of the thermal profile, while its main cooling unit is running.

Several power ON and OFF sequences are applied to each load, being the number of cycles and power higher in the case of the sample load. The length of the ON interval allows the load to reach thermal stability (30 to 60 minutes). The length of the OFF internal allows the load to cool down.

8.6.1.5.10 Tap test

On waveguide high RF power loads a final tap test is conducted to ensure no degradation on the absorbent. Once the load is removed from the vacuum chamber a piece of Kapton® tape is placed to cover the full waveguide void. Then, the load is place upside down and the load is tapped several times. If the material has burnt during the test the falling parts will be trapped by the tape. This test can include a visual inspection of the absorbent using an endoscope.

8.6.1.6 Test procedure for non-liquid cooled loads

8.6.1.6.1 Test sequence

The test sequence for a high RF power load includes:

1. Measurement of the scattering parameter before and after the power tests.
2. Preliminary bake-out of the units in an oven (ambient pressure).
3. Temperature measurement devices installation (thermocouples, pt-100, fibres...).
4. Verification of the security systems.
5. Ambient test up to the maximum RF power.
6. RF Power test at high vacuum.
7. Tap test.

Testing non liquid cooled loads is very similar to liquid cooled loads testing. In this case several steps do not longer apply.

8.6.1.7 Validity of the results

The loads are stored in a temperature and humidity controlled environment in order to ensure the validity of the tests between the RF test and the satellite TVAC test. After long periods of storage (> 1 or 2 year) the loads are retested to ensure its performance before they are used for a new satellite TVAC test.

8.7 Test reporting

The tables below provide a recommended list of information to include in the test report.

Table 8-3: Multipactor test report summary

Test site name	
Test sample description	
Operator name	
General parameters:	
S-parameter measurements (before and after)	attach s-parameter plots + data (in complex format)
Thermocouple locations	reference figure of sample
Temperature records	attach plots
Pressure records	attach plots
Power records	attach plots
Spectrum analyzer settings	
Detection systems used	
Seeding source type	provide source description/details
	provide information on positioning of source during tests
Clean room class	
Measurement accuracies for power	
Measurement accuracies for temperature	
Measurement accuracies for pressure	

Table 8-4: Test setup validation without sample

Test reference	
Start of the test (Date + time)	
End of the test	
Test frequency	
Maximum power applied without breakdown	
Power applied / power profile	attach file with power versus time
Pulse width	
Duty cycle	
Pressure readings (start, end, discharge)	
Thermal cycling parameters:	
Tmax	
Tmin	
Ramp rate (increase of temperature)	
Ramp rate (decrease of temperature)	
Dwell times (plateaus)	
Detection system responses	attach response plots + data file
Time under vacuum	
Observation summary	

Table 8-5: Test setup validation with reference sample

Test reference	
Start of the test (Date + time)	
End of the test	
Test frequency	
Power applied / power profile	attach file with power versus time
Expected threshold power	
Breakdown threshold power (first discharge)	
Breakdown threshold power (second discharge)	
Detection system responses	attach response plots + data file
Pulse width	
Duty cycle	
Pressure readings (start, end, discharge)	
Thermal cycling parameters:	
Tmax	
Tmin	
Ramp rate (increase of temperature)	
Ramp rate (decrease of temperature)	
Dwell times (plateaus)	
Time under vacuum	
Observation summary	

Table 8-6: Test of DUT at reduced power level at ambient pressure just before closing the vacuum chamber (RECOMMENDED

Performed/Not performed	
Power level	
Final test with RF Sample/Device	
Test reference	
Start of the test (Date + time)	
End of the test	
Test frequency	
Breakdown threshold power (first discharge)	
Breakdown threshold power (second discharge)	
Detection system responses	attach response plots
Pulse width	
Duty cycle	
Pressure readings (start, end, discharge)	
Power steps	attach file with power versus time
Thermal cycling parameters:	
Tmax	
Tmin	
Ramp rate (increase of temperature)	
Ramp rate (decrease of temperature)	
Dwell times (plateaus)	
Time under vacuum	
Observation summary	

8.8 Bibliography for clause 8

[8-1] ECSS-E-ST-10-03

[8-2] ECSS-Q-ST-70-01.

[8-3] A modified method for producing carbon-loaded vacuum-compatible microwave absorbers from a porous ceramic, Calame, J.P.; Lawson, W.G., in IEEE Transactions on Electron Devices, vol.38, no.6, pp.1538-1543, Jun 1991.

9 Secondary electron emission yield requirements

9.1 General

9.1.1 SEY definition and properties

When an electron of sufficient energy impacts on the surface of a material (primary electron) it can produce the emission of more electrons; this physical process is called secondary electron emission (SEE).

The secondary electron emission coefficient or yield (SEY) of a material surface, usually symbolized as σ, is the ratio of the number of emitted electrons to the number of incident electrons of defined incident energy and angle, in field-free conditions and under vacuum conditions. The secondary electrons can be true secondaries or backscattered electrons:

- The true secondaries are electrons emitted from the materials with energies, conventionally less of 50 eV, with an emission coefficient δ
- The backscattered electrons are assumed to be primary electrons backscattered again into vacuum by collisions with the material. These emitted electrons have energies up to the impacting or primary energy, with a coefficient η. Then $\sigma = \delta + \eta$.

The emitted electrons with low energies, conventionally less of 50 eV, are considered as true secondary electrons. For very low primary energies (<100 eV) δ might become of the same order of σ.

A typical dependence of these coefficients on primary electron energy is shown in Figure 9-1. Nowadays, the limit of SEY, as primary energy approaches 0 eV, is being studied.

A spectrum showing the energy distribution of the emitted electrons has more detailed information and is known as Energy Distribution Curve (EDC), see Figure 9-2.

True electrons have an emission angle distribution close to the cosine or Lambert's law. Backscattered electrons can have a complicated angle distribution law.

All these properties, σ, δ, η, EDC, and emission angle distribution, depend on the incident primary electron energy and angle. These functions are necessary for a detailed and accurate simulation of the multipactor effect. However, the experimental measurements dependence $\sigma(Ep)$ of the total secondary emission on the primary energy Ep for normal incidence of $\sigma(Ep)$, for normal incidence, usually named SEY, is considered the most relevant important for multipactor simulations, and the others can be estimated approximately from general empirical laws.

$\sigma(Ep)$ SEY-primary-energy curves can be usually characterized by a few parameters: σ_m (> 1, usually) and E_m for the maximum, and the cross-over energies E1 and E2 where $\sigma = 1$, i.e., $\sigma(E1 < Ep < E2) > 1$, see Figure 9-1.

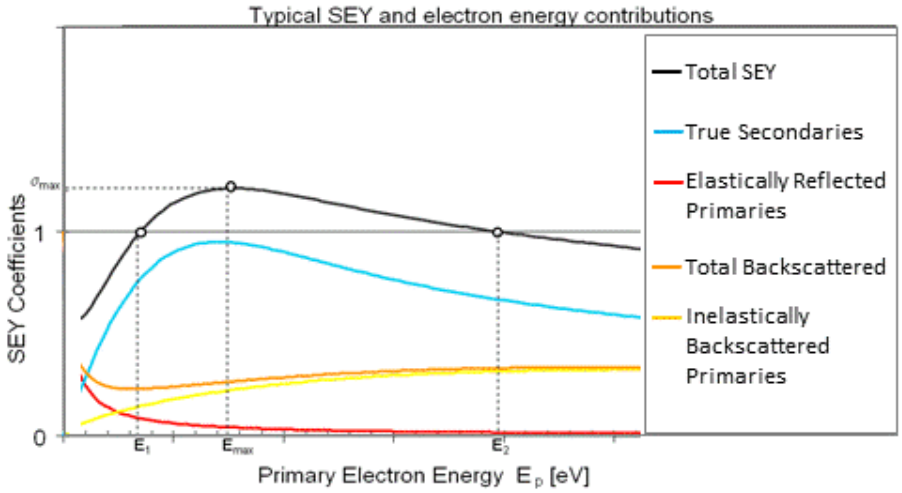


Figure 9-1: Typical dependence of SEY coefficients on primary electron energy.

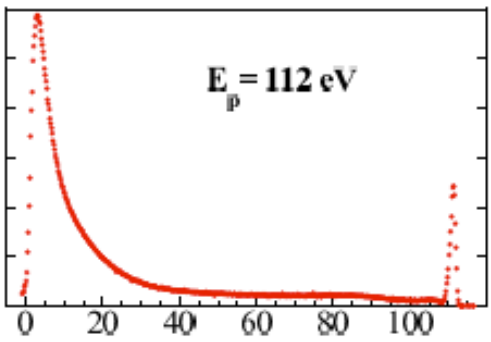


Figure 9-2: Energy distribution curve of emitted electron from gold target surface submitted to 112 eV electron irradiation [9-1]

9.1.2 SEY and Multipactor

Secondary electron emission plays an essential role in multipactor breakdown being the main trigger and sustaining mechanism of the discharge [9-2]. For example, a change of SEY for a non-standard silver coating varying from E1 = 40 eV, σm = 1,71, Em = 265 eV to E1 = 30 eV, σm= 2,01, Em = 218 eV, which is due to air [9-3], decreases the multipactor threshold in about 2,5 dB as predicted by a typical simulation tool.

The secondary electron emission is a surface process and, as such, is often not well characterized. It depends on the type of material but also on the surface finish: surface contaminants and surface morphology. It is strongly influenced by interactions with environment: exposure to the air, humidity, air contaminants, temperature … In space, it can also be influenced by irradiation with electrons, ions or photons. The uncertainty on the secondary electron emission properties is one of the reasons for the use of safety margins in multipactor analysis.

As stated in 9.1.1, multipactor is the resonant growth of an electron cloud in RF components by secondary electron emission from exposed surfaces. When electrons accelerated by the RF field impacts on a surface, secondary electrons are emitted from the surface. Main definitions and properties of secondary electron emission (SEE and SEY) are given above.

In multipactor, the electron avalanche is self-fed by secondary electron emission from the surfaces of the RF component exposed to electron impact. SEY is the electron multiplication origin and the RF field supplies the energy accelerating the electrons. This phenomenon occurs wherever some resonance conditions involving the RF electromagnetic field and the secondary electron emission properties of surface material are met.

The SEY for low primary or impacting energies has most influence on multipactor susceptibility, being E1 one of the most important parameters to predict Multipactor. If vacuum level inside the device is not very high, free electrons might impact on gas molecules and produce the emission of some of their electrons and also induce gas desorption from the wall of the device. The electron trajectories are thus truncated or twisted, and the free electron population increased. Also free gas ions are produced forming plasma. At higher pressures a Corona discharge might evolve.

9.1.3 Factors affecting SEY

For most materials used in critical parts of RF space devices or in particle accelerators, SEY mainly depends on the following factors:

- Surface composition:

  SEY depends on the chemical composition of the materials. However, secondary electron emission is a surface process occurring in a depth range of a few nm, where the top atomic layers of the surface have an important influence. Very often the surface composition is different from the bulk (base material) and unknown. It can be affected by gentle treatments which do not modify the bulk and thus remaining unnoticed.

- Temperature:

  The on-board equipment temperature can also modify the SEY values. High temperature conditions under vacuum causes mainly desorption of surface contaminants or even modification of surface oxides, thus, often modifying values of SEY [9-4] [9-5] [9-6].

- Electron conditioning:

  When electron bombarding of a surface with relatively low energies (hundreds of eV) and with high dose, processes occur which result in a modification of SEY [9-7].

- Photon conditioning:

  Irradiation with energetic photons (hundreds of eV) can cause desorption or chemical reactions thus modifying SEY.

- Ion conditioning:

  Bombarding a surface with noble gas ions of low energies (hundreds of eV) is more drastic than electron conditioning: produces also desorption of oxygen-containing molecules, but in addition decomposition of surface oxides and erosion of surface material. Surface carbon contamination is also eroded away. The result is a cleaner surface (in the sense of more representative of bulk composition). Some surface roughening can also be created. Ion conditioning usually results in a significant modification of SEY.

- Surface roughness:

  Surface roughness can be used to decrease significantly SEY [9-8] [9-9]. The emitted electrons can be trapped in the wall of the protuberances of the surface. The final effect can be strong reduction of the SEY.

- Air exposure:

In most metals, exposure to the air produces formation of surface oxides (chemical oxygen absorption) and physical adsorption of oxygen and carbon containing molecules-and radicals: e.g. O2, H2O, OH, CHx [9-2].

Also the sulphidation reactions due to the hydrogen sulphide gas in air for instance: the formation of silver sulphide. These processes induce secondary electron yield variation. Long term variations (ageing) of the SEY in the scale of months or even years cannot be discarded.

- Storage method:

  Significant differences in SEY parameters of RF samples can happen for the different storage methods, except for samples stored in inert atmosphere. Samples stored in air can show most instability in SEY, thereby yielding the highest SEY values. For this reason, it is recommended to store samples in inert atmosphere or vacuum.

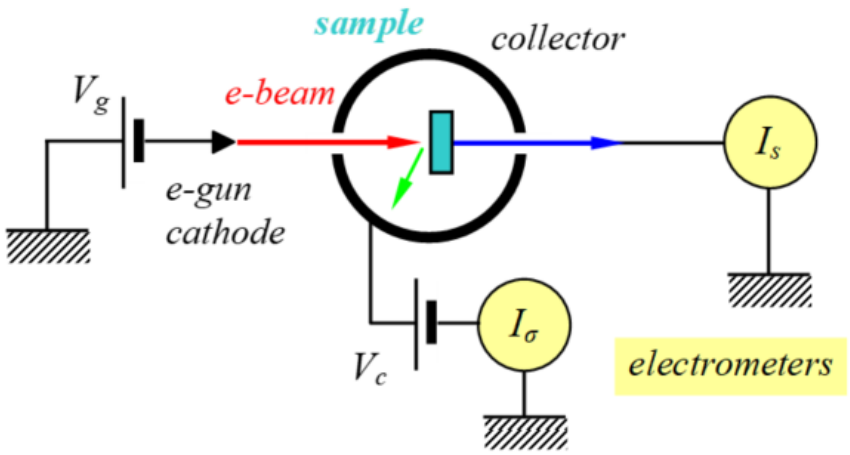
  SEY for low primary energies originates closer to the surface and thus it is most affected by the above mentioned factors, implying a strong influence on multipactor susceptibility.

  For all these effects, SEY can be modified. The fact that this evolution can be an increase or a decrease needs to be proven through measurements on different materials in different test facilities.

9.1.4 SEY testing

For measuring the emitted current, a weak electrostatic field is set in order to avoid both low-energy secondary electrons returning back to the surface and 2nd-generation secondary electrons from surrounding surfaces (e.g., collector or vacuum chamber walls) generated by energetic secondary electrons (backscattered electrons). This is achieved by a small negative bias (-10 V to -50 V) to the sample with respect to the surroundings, or by positive bias of the surrounding. Ideally, this field is spherically symmetrical respect to the emitting spot, i.e., created by a semi-spherical electron collector

In more complex testing arrangements, spherical grids and collectors (and several electrometers) are used for obtaining field free conditions around the sample to be tested, avoiding 2nd-generation secondary electrons from surrounding surfaces, and measuring both primary and secondary electron currents, all together and simultaneously. However, the usual simpler arrangement described here has sufficient accuracy [9-11], see Figure 9-3.



The red, green, and blue arrows correspond to the primary, secondary, and sample electron currents.

Figure 9-3: Experimental arrangement for SEY test with emission collector

An electron gun supplies the primary electrons or electron beam to irradiate the sample. The primary electron energy Ep is determined by the potential difference between the sample connected at the ground and the cathode of the electron gun (usually a hot cathode), at Vg:

$$E_p = e\left|V_g\right| \qquad [9\text{-}1]$$

This is just the "nominal" primary energy. There is an uncertainty of about ±1 eV due to the difference between the work-function (surface potential barrier) values of the sample ϕs and the cathode ϕg, both being usually 5 eV ±2 eV, since voltage meters measure only potential differences between Fermi levels.

The electron currents coming in and out the sample are: the primary current Ip from the e-gun, the emission current I_σ going to the surroundings (collector or the analysis chamber walls), and the sample current I_s.

A good experimental arrangement is a spherical collector around the sample; as schematized in Figure 9-4. Then, I_σ as measured in the collector meter positively biased at Vc. I_p is measured with a Faraday cup in place of the sample. I_p is also always negative. When testing a sample, the sample and the collector all together form a Faraday cup and then:

$$I_p = I_\sigma + I_S \qquad [9\text{-}2]$$

This is the condition of no charge accumulation for a conductive sample connected to ground at a constant bias. This is also an approximation. The 2nd-generation secondary emission from the surroundings falling on the sample has been neglected. This is a very good approximation if the appropriate sample negative bias or positive collector bias is set.

I_s is measured in the sample meter connected to ground, and has the sign of σ - 1.

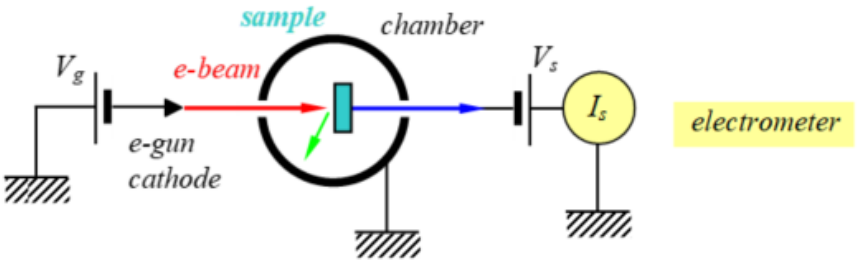
The secondary electron emission coefficient or yield (SEY) is then:

$$\sigma = \frac{I_\sigma}{I_p} = \frac{I_\sigma}{I_\sigma + I_p} \qquad [9\text{-}3]$$

When a collector is not available, only the sample current Is is measured, see Figure 9-4. In this case, the e-gun current I_p is previously measured with a Faraday cup or calibrated by a reference sample with well-known SEY properties (equation [9-4]):

$$I_p = -\frac{1}{(\sigma_{ref} - 1)} I_S(ref) \qquad [9\text{-}4]$$

Where σ_{ref} and $I_s(ref)$ are respectively the secondary electron emission coefficient and the sample current to ground of a reference sample, usually a Faraday cup. In equation [9-4], for σ_{ref} approaches 1 I_p tends to infinite. It is an artefact of the coordinate system, and it is best practice to remove this apparent discontinuity or singularity.



The red, green, and blue arrows correspond to the primary, secondary, and sample electron currents. Electrometers give positive charge currents

Figure 9-4: SEY experimental setup (without collector around the sample)

The secondary electron emission coefficient or yield (SEY) is then:

$$\sigma = \frac{I_\sigma}{I_p} = 1 - \frac{I_S}{|I_p|} \qquad [9\text{-}5]$$

For a Faraday cup $\sigma_{ref} \cong 0$ with a precision depending on its design. The Faraday cup set-up has to be well positioned and designed (Faraday Cup positively biased and positioned directly at the output diaphragm of the e-gun). In case of reference method samples, the best is to use noble metals as Pt, Au, Ag, or Cu, used with the same test conditions of the sample to be tested. In this case, surface oxidation or contamination of these reference metals have also to be avoided or eliminated. Before SEY measurements if reference samples were exposed to the air, they are cleaned in-situ. Clean surfaces are easily obtained by low-energy Ar ion sputtering (few keV) at room temperature.

A combination of techniques optimized for the particular experimental arrangement is usually the best calibration technique.

The e-gun, is able to supply a stable beam current for all required energies with controlled low dose. These low values are necessary for avoiding surface "conditioning" or modifying by the e-beam. This effect is well known and tends to modify SEY by surface processes. Also the total dose or fluency is small, for metallic or conductive samples

In general, for any surface analysis technique, and more important in relation to surface conditioning, ultra-high vacuum is recommended in the analysis chamber.

Minimization of electron dose becomes even more crucial in dielectric or non-conductive samples. Indeed, primary charge is trapped on the surface leading to surface charge potential that affects the real energy of primary electrons. That results in SEY-energy values very different from the uncharged sample one. This effect can be avoided by using a pulsed e-beam with low- dose pulses. The induced image charge on the sample substrate or stage can still be measured with a fast oscilloscope. The charge trapped on the surface on a non-conductive sample in the pulsed method can also be measured by a Kelvin probe detecting the corresponding surface potential.

Some dielectric samples can also be charged by tribo-electrification before irradiation. The surface potential is in this case measured and removed before SEY measurements.

Apart from the instrumental errors (e.g. in the measurements of e-gun energy and sample currents, noise induced in cables and electric contacts) the main problems in the accuracy of SEY measurements are the accuracy of the e-gun primary current impacting on the sample. This last one becomes crucial for very low primary energies.

9.2 SEY measurements justification

No supporting material needed.

9.3 Worst case SEY measurement

No supporting material needed.

9.4 SEY measurements conditions

9.4.1 Environmental conditions

9.4.1.1 Handling storage and transportation

In the light of results obtained during the ERS satellite test programme and other tests where significant degradation in multipactor occurred due to contamination, the methods used for long term component storage are applicable in the present case.

External protection

- Storage is performed by using hard plastic boxes rather than plastic bags.
- If hard plastic boxes are used, they are cleaned before use with a solvent, such as Isopropyl Alcohol.
- If plastic bags are used, prevent direct contact of the plastic with the component.
- To prevent the direct contact of the plastic with the component in the case specified in point ◎. above, the component is well wrapped with lint free tissue.

Inert gas

- With the component in the bag or box, fill with an inert gas such as dry nitrogen so as to exclude the normal atmosphere.

Storage environment

- The protected component is then kept in a stable environment, as specified in ESCC Basic Specification No. 24900.

9.4.1.2 Cleanliness

a. Contamination

   See ECSS-Q-ST-70-01

b. Ageing

The ageing effect on the SEE, is a very old problem that start to be addressed in beginning of the last century, shortly after the discovery of the secondary electron effect in 1901 by Austin and Starke [9-10]. The literature on this topic is very large. In this report we focused our attention to the recent work that was performed mainly by the CERN the last ten years and also by the CSIC and UAM in the framework

of the ESA projects and the ONERA in the framework of CNES projects. However, near all the studies were dedicated to the metallic surfaces. For dielectric, an analysis is given.

It is well known that the surface composition and structure of the samples changes during the time (ageing). As the SEE is highly sensitive to first nanometers depths of the material, obviously the ageing affects the SEY. When the surface of metallic or dielectric sample interact with a specific atmosphere, oxidation and contamination process occur. The kinetic of this two processes depends on the nature of the sample and the composition of the environment.

Atmospheric contamination

A metal considered to be pure (> 99.99%), has a very low concentration of impurity in its volume (bulk). Despite its purity, this material can no longer be considered pure regarding its surface composition since it is exposed to the ambient atmosphere. Indeed, ambient atmosphere contains a certain amount of volatile compounds as carbons species, oxygen, water…

The Figure 9-5 shows the example of aluminum which oxidizes on contact with the oxygen in the air. A layer of aluminum native oxide Al_2O_3 is directly present at the surface. McCafferty [9-12] analyzed in details (layer by layer) the exposed to atmosphere. The contamination and oxidation layers form many material layers with distinct compositions (see Figure 9-5). The thickness of this contamination layer varies typically from few nm to tens nm.

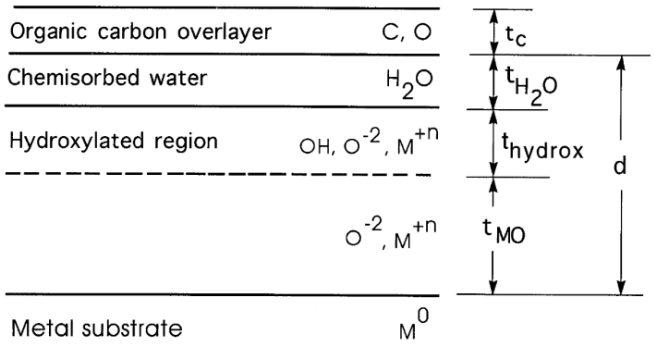


Figure 9-5: Typical composition of exposed to air metal surface

According the fact that the SEY is extremely dependent of the first nanometers of the material surface, the measured SEY of exposed and not cleaned metals reflects more the properties of the contaminant than the material itself.

Figure 9-6 shows SEY measured on metals exposed to air without a specific surface cleaning procedure (ion etching, heating,). The SEY are very similar with a typical SEY maximum about 2. This figure illustrates the fact that in many practical cases the measured SEY is that of the contamination. For instance, when the contamination layer of aluminum is removed with Argon etching the maximum of the yield falls from 2,3 to 0,95 [9-13].

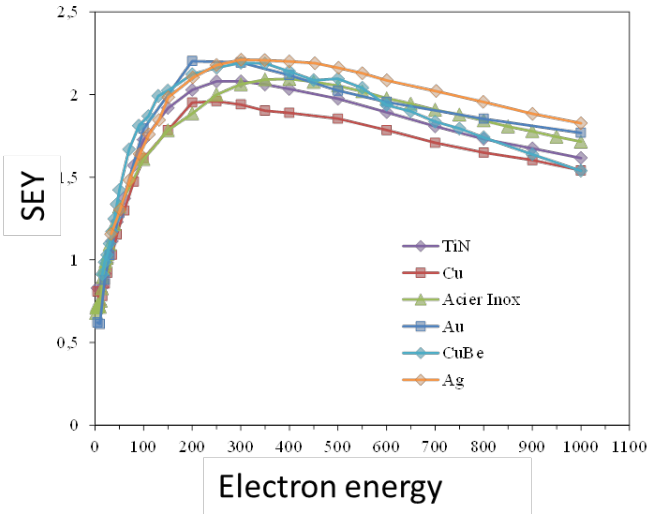


Figure 9-6: Measured SEY of metals exposed to air without a specific surface cleaning procedure

During the EVEREST project (ESA TRP project ESA contract TRP n°22452/09/NL/GLC under CNES coordination), a SEY sample measurement strategy was devised to obtain SEY inputs (in addition SEY data from ECSS-E-20-01A) for the Multipactor threshold prediction. Since the critical surfaces were inside of the RF devices, SEY samples (simple metallic plates) representing the surface properties "as built" and "as tested" were manufactured. Great care has been taken to manufacture the SEY samples from the same batch and with the same material process as the corresponding RF component: i.e. same base material, same coating and surface treatment (Ag plated Aluminium alloy). For each RF device 6 samples where used, 3 of them (as built) were sent to 3 SEY entities identified in Europe. The other 3 (as tested) were following the corresponding RF device, before being sent to the 3 SEY entities at the time the Multipactor test was carried out [9-14].

With this strategy it was possible to monitor the SEY properties evolution of the samples (and hence the RF devices) throughout the life cycle of the device until testing.

4 SEY entities were involved in the study.

The below tables sum up per SEY entity the average values of the main parameters for all "as built" (mentioned "Before RF testing" in the Table 9-1) and all the "as tested" SEY samples (mentioned "After RF testing" in the below table) for a given SEY measurement facility:

Table 9-1: Average values of the main SEY parameters for all "as built" (mentioned, "Before RF testing" in the below table) and all the "as tested" SEY samples (mentioned, "After RF testing" in the below table) for a given SEY measurement facility

SEY	BEFORE RF TESTING				
Values	E_1	σ_m	E_m	σ_{1000}	N
SEY entity 1	26	2.17	334	1.86	6
SEY entity 2	19	2.25	316	1.76	6
SEY entity 3	21	2.43	325	2.03	6
SEY entity 4	27	3.1	381	2.61	1
Average	**22**	**2.28**	**325**	**1.88**	**19**

SEY	BEFORE RF TESTING				
Dispersion	E_1	σ_m	E_m	σ_{1000}	N
SEY entity 1	6	0.45	27	0.43	6
SEY entity 2	2	0.29	36	0.34	6
SEY entity 3	3	0.23	37	0.28	6
SEY entity 4	0	0	0	0	1
Average	**4**	**0.32**	**33**	**1.78**	**19**

SEY	AFTER RF TESTING				
Values	E_1	σ_m	E_m	σ_{1000}	N
SEY entity 1	25	2.17	329	1.78	10
SEY entity 2	20	2.17	295	1.69	10
SEY entity 3	23	2.28	330	1.88	10
SEY entity 4	17	2.62	271	2.03	4
Average	**23**	**2.21**	**318**	**1.79**	**34**

SEY	AFTER RF TESTING				
Dispersion	E_1	σ_m	E_m	σ_{1000}	N
SEY entity 1	8	0.42	72	0.41	10
SEY entity 2	4	0.32	50	0.28	10
SEY entity 3	8	0.21	55	0.34	10
SEY entity 4	2	0.24	10	0.16	4
Average	**6**	**0.3**	**53**	**0.32**	**34**

A few elements of synthesis can be underlined. First, the average values are in line with known values for the silver plating. Then, the difference between the direct and the non-direct SEY samples, SEY characteristics for the main parameters are quite light, which proves that the effect of manipulation is quite limited for silver plating: E1 has an identical average value before and after RF testing and σm has a spread of 0,06 for the average values before and after RF testing. Through the tables, the dispersion of the E1 parameter is confirmed to be of about 6 eV - 8 eV.

The silver coating is commonly used in RF space applications. According to literature review a schematic view of the sample surface is given in Figure 9-7.

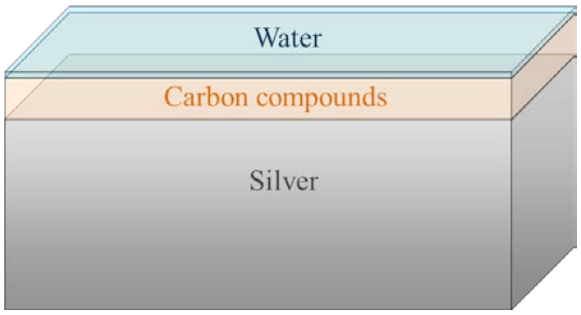


Figure 9-7: Schematic view of material exposed to atmosphere: the case of silver

Comment: the RF Hardware in space is subject to a relatively high temperature in some situations (80 °C and more) due to the power dissipation and also due to thermic constraints of the spacecraft and under ultrahigh vacuum (< 10^{-13} hPa).

Literature review: consequences on the SEY

- **Metals**

Many studies demonstrated that, the atmosphere exposition always increases the SEY of metals. The CERN conducted many works on the subject because the multipactor in the protons injection chamber is considered one of most limiting problem for the Large Hardon Collider. All these references, pointed out that:

"The SEY increase during air exposure is mainly caused by the adsorption of an organic surface contamination with embedded water molecules. In some cases, the formation of an insulating oxide or hydroxide can contribute

to the overall SEY increase. The SEY of air-exposed metal surfaces is related to the degree of surface contamination. The stronger the contamination, the higher the SEY" (paragraph extracted from [9-15])

This is illustrated by Figure 9-8 from [9-16], where the SEY of Nb is plotted as function of the baking time and temperature. These measurements were conducted in conjunction with chemical analyses of the surface that clearly demonstrated that the decrease of the SEY is correlated to the evaporation of the surface contaminants.

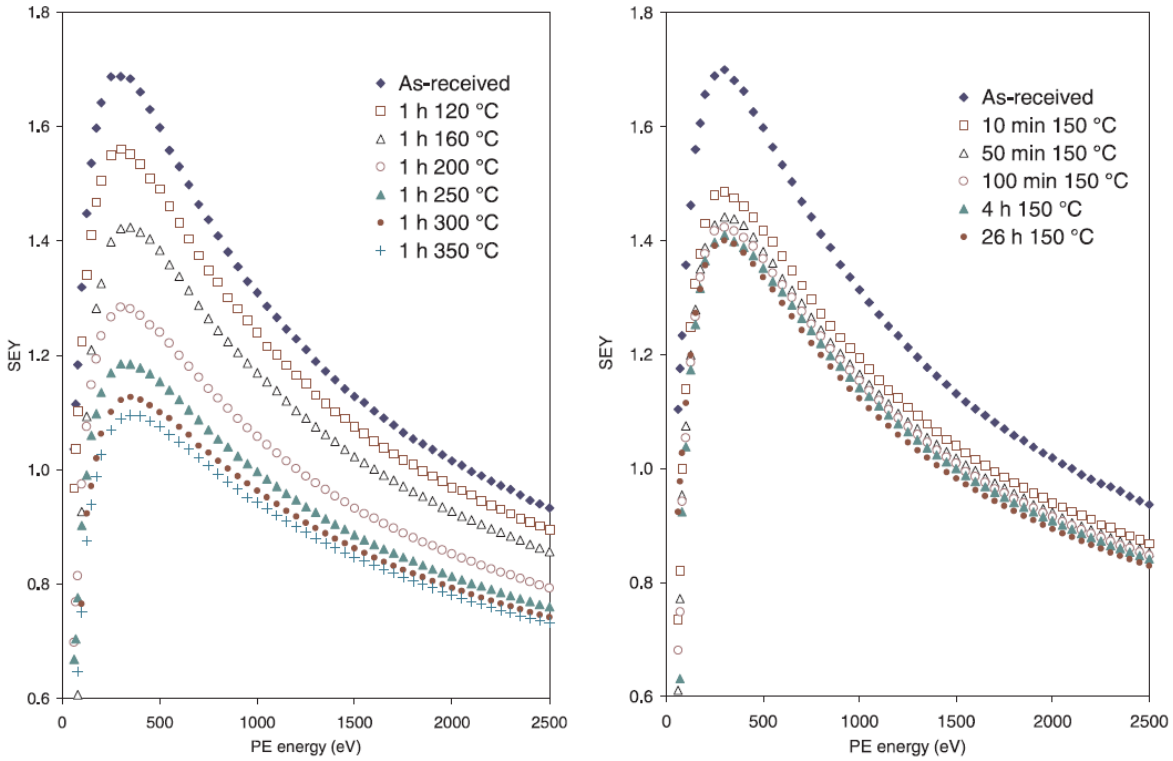


Figure 9-8: Effect of cleaning of the surface by heating on the SEY of Nb.

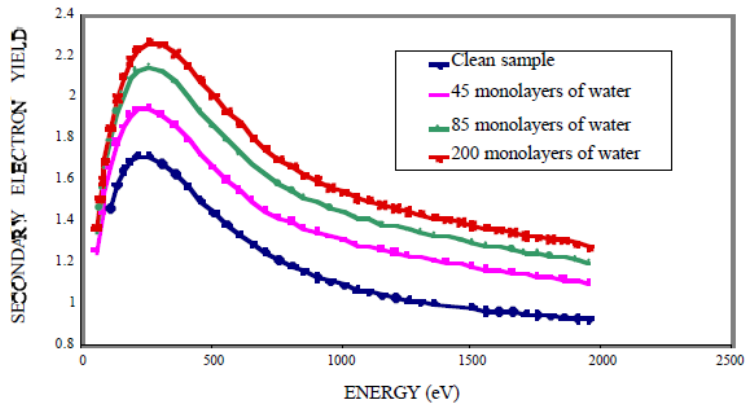
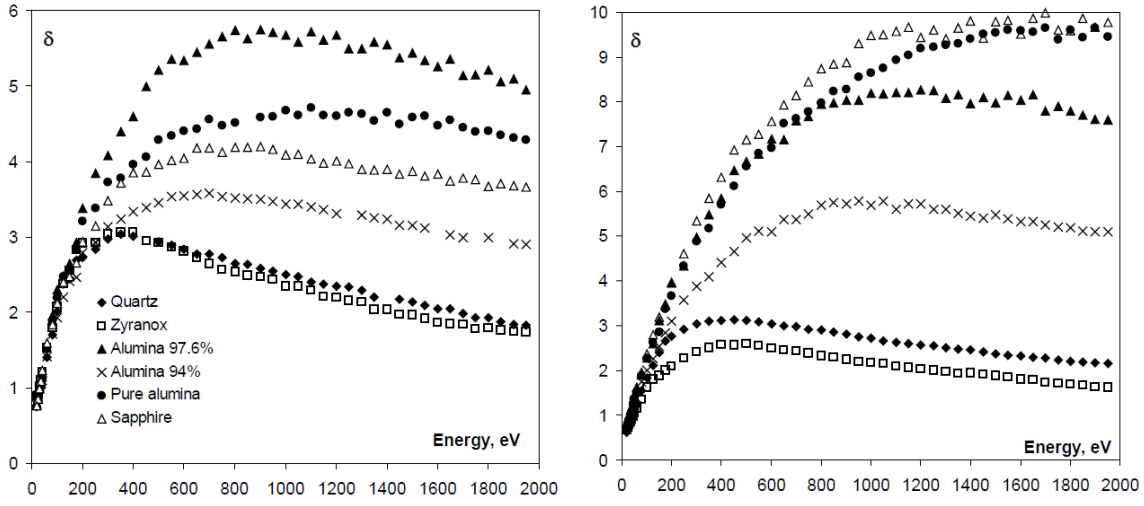


Figure 9-9: Effect of the water absorption on the SEY.

As conclusion: for metals any organic or mineral contaminant generated by the storage conditions (air, oxidation, water,…) increases the SEY of clean metals.

- **Dielectrics**

The literature on ageing effect due to the storage conditions on dielectrics is extreme poor. The SEY of most dielectrics are higher than that of metals (even for the exposed to air metals). Therefore, as the typical SEY maximum of contaminants is about 2 – 2,5, it is expected that the exposure of dielectrics to atmosphere (controlled or not) reduce the SEY. An illustration of this is given in the Figure 9-10, extracted from [9-17]. The SEY of ceramics and quartz increases (opposite situation to that of metals) after heating the samples to 350 °C under UHV.



Crystal	"as received" state		After baking out 350°	
	σ_{max}	E_{max}	σ_{max}	E_{max}
Quartz	3	370	3,15	405
Zyranox	3,06	335	2,6	470
Alumina 97.6%	5,7	935	8,2	1150
Alumina 94%	3,55	695	5,75	1000
Pure Alumina	4,6	1090	…	…
Sapphire	4,2	775	…	…

Figure 9-10: Effect of baking on the SEY of dielectrics.

9.4.1.3 Pressure

During the EVEREST project [9-14], it was studied the influence of the pressure of the chamber on the SEY characteristics of the silver samples. SEY curves were measured in the range 10^{-6} to 10^{-9} hPa on several metallic samples. Figure 9-11 shows the SEY curves of a silver coating and a silver foil measured by the pulsed method. In this pressure range, it was demonstrated that, at room temperature, the SEY characteristics are not sensitive to the pressure.

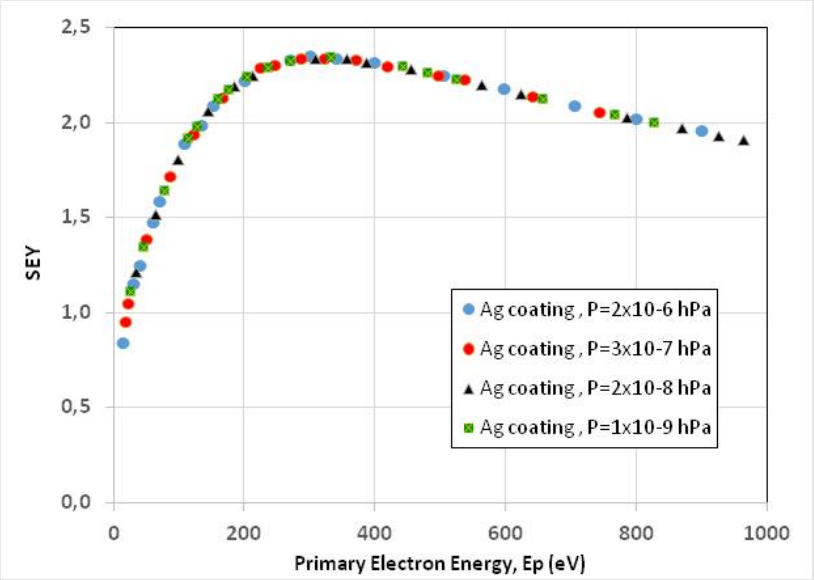


Figure 9-11: Evolution of the SEY of the technical silver versus pressure.

9.4.1.4 Temperature

The variation of the temperature affects also the SEY. According to the literature [9-5] [9-6] for most metals a decrease of the yield is systematically observed whereas for dielectrics there is no general rule.

- **Metals**

The main effect of the temperature on metals is the partial or the total evaporation under vacuum of a part of the surface contamination. The SEY of clean surface of metals is originally low, for instance the maximum of SEY of clean silver is about 1,6 and the first crossover is about 130 eV. When exposed to atmosphere, the contamination process is quite fast (in the range of few minutes).

When its surface is exposed to atmosphere, the SEY growth to 2,25 and E1 decreases rapidly to 24 eV (This fact is illustrated in the Figure 9-12). The contamination either composed by hydrocarbon molecules and a monolayer of H_2O has typically a maximum of SEY yield between 2 and 2,6, significantly higher than that of most of metals. The desorption of contaminants leads to the decrease of the electron emission yield. This tendency can be extended to others many metallic materials as it was observed by many groups (Al, Cu, Au, TiN, Surtec, Pd, Cr, Ni…). This is illustrated for a silver sampleb [9-18] in Figure 9-12.

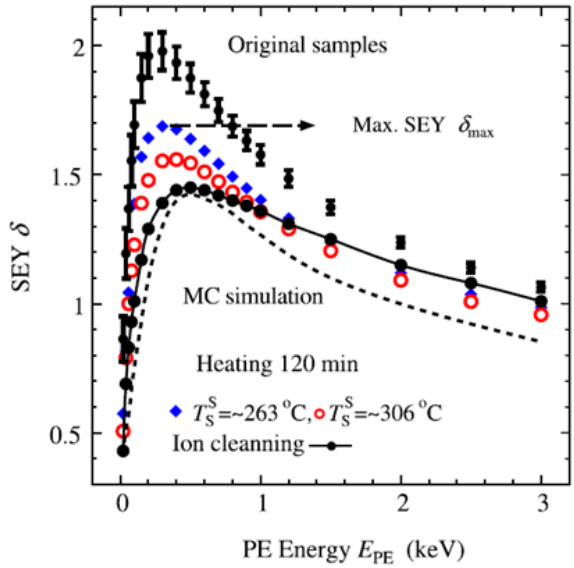


Figure 9-12: Effect of the temperature on the SEY of silver. Figure extracted from [9-18].

- **Dielectrics**

For dielectrics the two opposite trends were observed:

A decrease of the electron emission yield due to the increase of the electron-lattice vibration [9-19] interactions as it is shown for MgO and also due to temperature stimulated desorption of contaminant as it is shown in for BN-SiO2, see Figure 9-13.

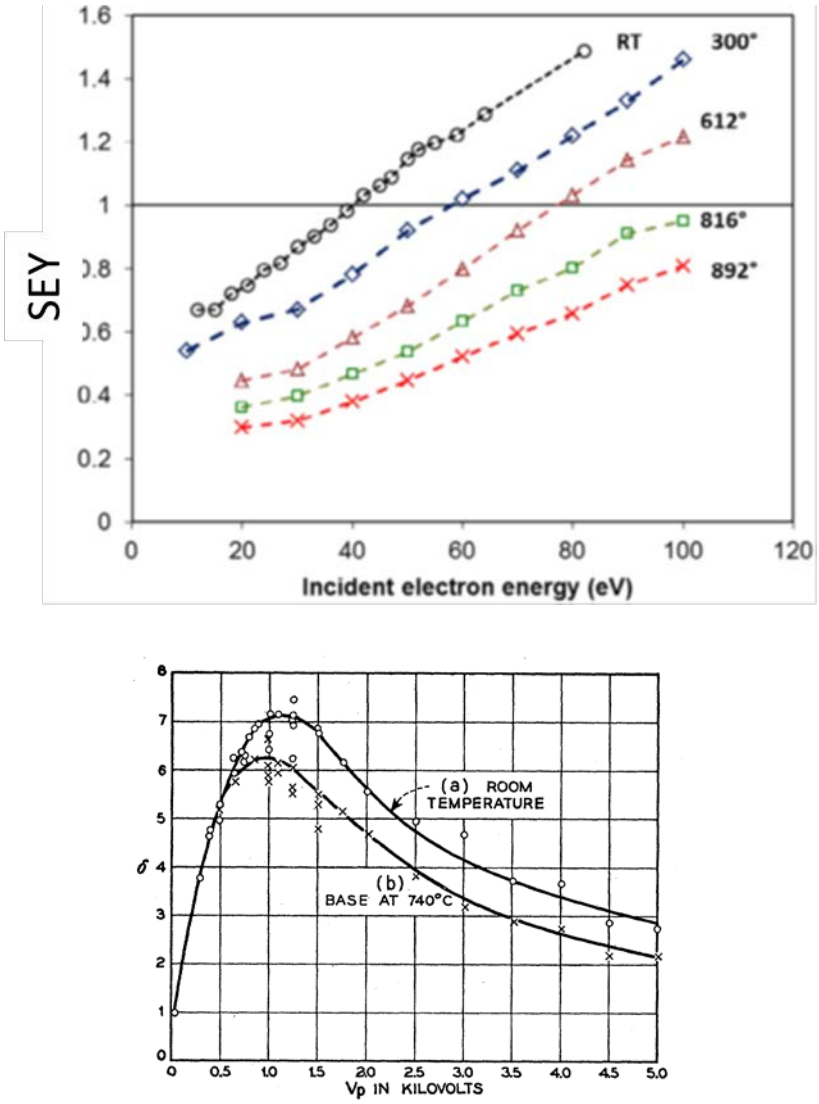


Figure 9-13: Effect of the temperature on the SEY of MgO and BN-SiO2 ceramics.

An increase of the SEY due to the enhancement of the charge carrier transport that results on the attenuation of the effects of charging in the case of satellite coverglass and CVD diamond [9-19] [9-20] [9-21], see also Figure 9-14.

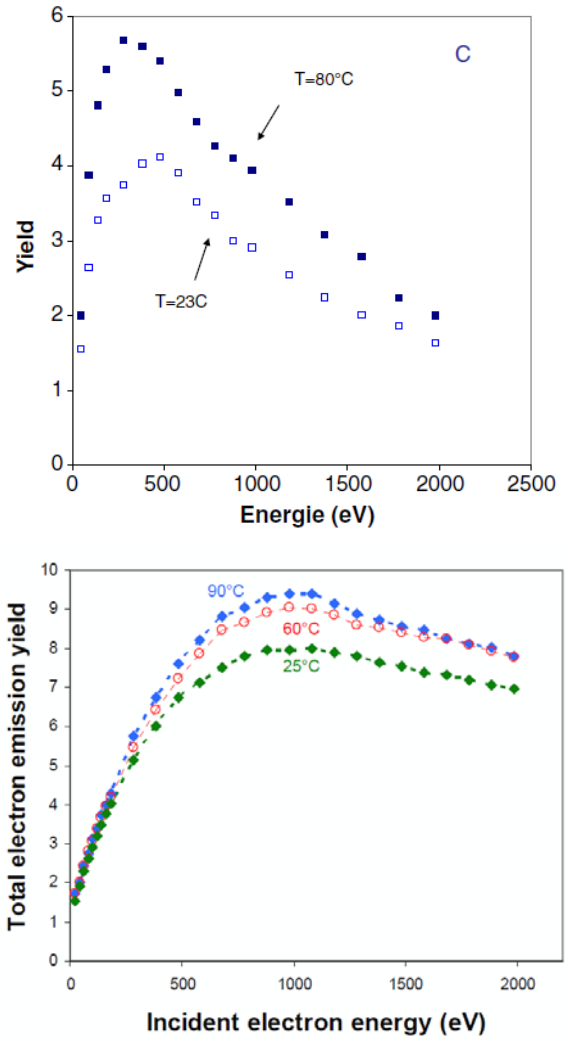


Figure 9-14: Effect of the temperature on the SEY of coverglass and CVD diamond

9.4.2 SEY test bed conditions

9.4.2.1 Incident electron energy

No supporting material needed.

9.4.2.2 Incident angle

An overall increase of the SEY is generally observed when the incidence angle increases for flat surfaces. Note that the first crossover energy, which is one most important SEY parameter for multipactor, is approximately independent from the incidence angle for flat surfaces.

The Figure 9-15, shows the influence of the incidence angle on silver SEY (an electron that hits the sample perpendicularly to the surface is said to have a 0° incidence angle and a tangent electron a 90° incidence angle), [9-22] [9-23] [9-24].

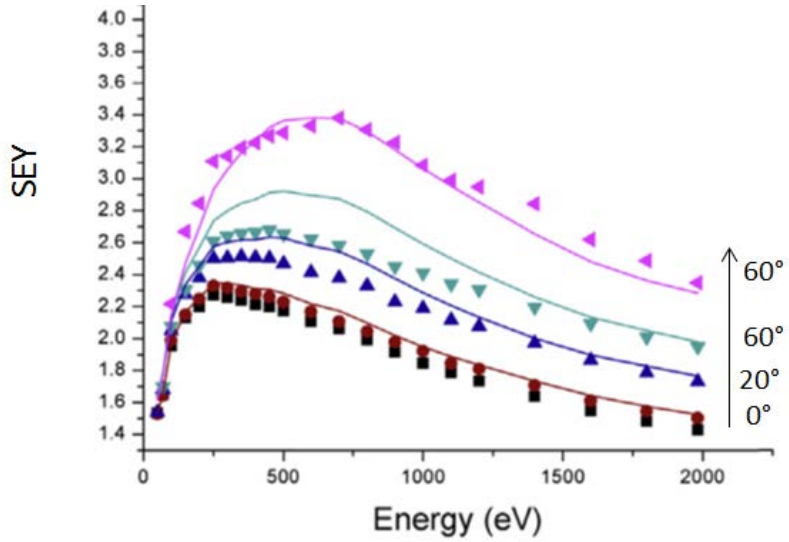


Figure 9-15: Effect of the incidence angle variations on the SEY of silver

9.4.2.3 Electron dose

Radiation induced desorption of contaminates yields to SEY decrease as the effect of the increase of temperature for metals. This phenomenon has been systematically observed by many groups [9-7]. This effect results has been observed at CERN for many materials: Aluminium, copper, steel, TiN,…(see Figure 9-16).

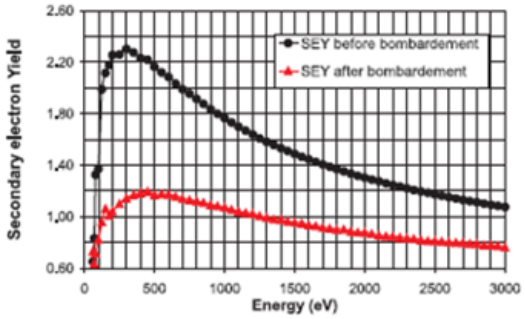


Figure 1: Variation of δ_{SEY} as a function of the primary electron energy, for a sample of copper colaminated on stainless steel, before and after bombardment with 500 eV electrons, corresponding to a dose of 5×10^{-3} C/mm^2.

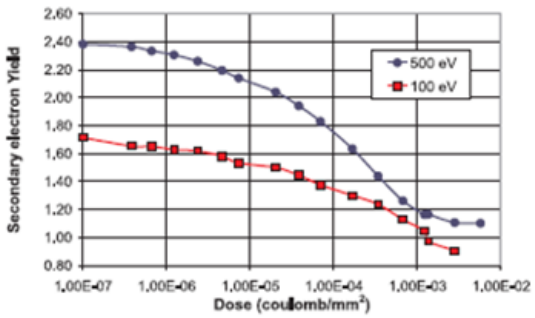


Figure 9-16: Effect of electron irradiation on SEY (CERN)

9.4.2.4 Charging requirements for dielectric samples

When a grounded metallic sample is exposed to electron irradiation, the excess of injected charge is evacuated via a leakage current to the ground. For dielectric the situation is different. Indeed, the charge carrier mobility is in most cases very low, so that a net positive or negative charge accumulated on the near surface region of the sample.

Figure 9-1 shows schematically the typical dependence of SEY on the landing energy of incoming electrons. If the incident electron energy, E_0 is higher than the second crossover energy E_2, or lower than the first crossover energy E_1, then flux of incoming electrons exceeds that of the emitted ones and negative charge is injected in the sample. This charge give rise to an electric field in the vacuum of the specimen chamber and inside the dielectric, which slows the incident electrons and shift their landing energy down to $E_0 + eVs$, e being the electron charge ($e = 1{,}6\ 10^{-19}$ C) and Vs being the negative surface potential. This decrease of the landing energy leads to an increase of the SEY. The negative trapped charge reaches its saturation value when SEY = 1 (the electron landing energy equals, E_1 or E_2).

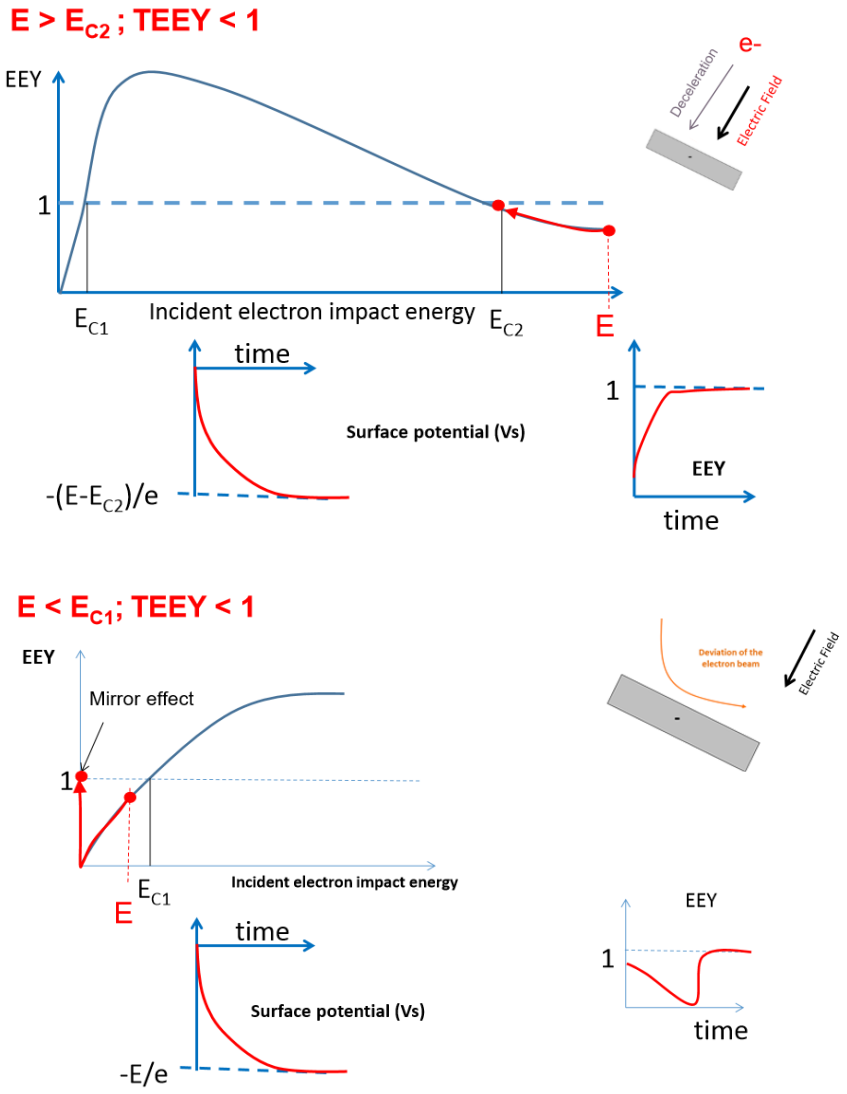


Figure 9-17: Influence of the primary electron energy on the charging process. TEEY = SEY, E_{C1} = E1 and E_{C2}=E2

Conversely, If E_0 is between E_2 and E_1, the dielectric charge positively, but very low secondary electrons were attracted back to the sample so that the total charge is close to zero and the insulator is then charged to small positive potential (some volts).

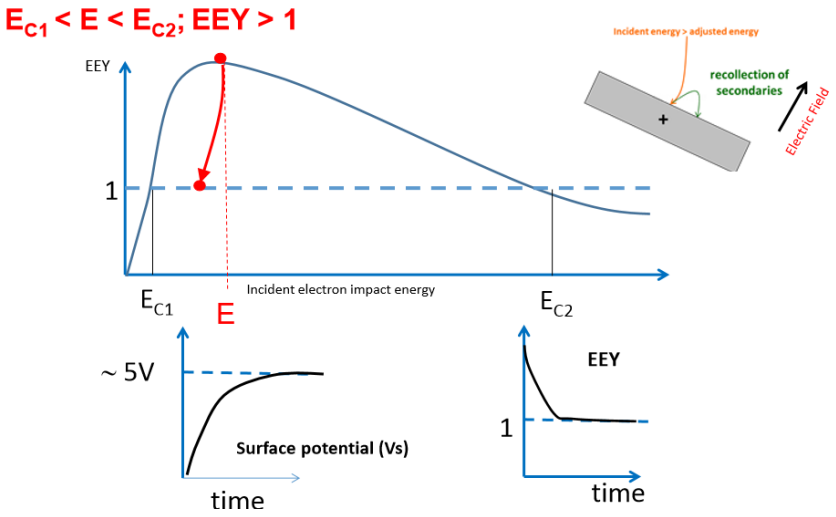


Figure 9-18: Influence of the primary electron energy on the charging process, EEY = SEY, E_{C1} = E1 and E_{C2}=E2

In addition to external effects of charging, the internal ones are also considered. The generated holes subsequent to the SEY emission [9-25] [9-26] [9-27] as well as the inner electric field [9-28] [9-29] [9-30] leads to the reduction of the SEY escape probability and hence to the decrease of the SEY.

For dielectric sample a special care and an appropriate methodology is used to monitor the charging level during the SEY measurement and discharge the sample surface when the charging interfere with the SEY measurement.

Note that in many situations the dielectric sample can be charged due to triboelectrification before the irradiation. For instance, Teflon can develop hundreds of volt just due to the mechanical stress when it was attached to the sample holder.

9.4.3 SEY sample characteristics

No supporting material needed.

9.5 SEY measurements procedure

9.5.1 SEY Measurements procedure documents

Table 9-2: Requirement in the experimental conditions for SEY measurement

SEY TEST PROCEDURE GENERAL CONDITIONS ICMM		
Parameters	**Specifications**	**Results**
Sample:	**KS2-CSI (Thales Alenia)**	
Sample inspection	Rapid visual inspection	Clean
Time between sample bag aperture and chamber closure	< 10 min	6-8 min
Time under vacuum	No spec	23 days
Bake-up	Defined in paragraph 2.1	No bake-up
Conditioning or treatments	No	No
Post-test Conditioning	Sample kept in dry atmosphere and room temperature	From 12/07/2012 in dry N_2 atmosphere, 12% humidity
Test Chamber:		
Temperature	Room Temperature	22°C
Pressure	$<5.10^{-6}$hPa	$3,7.10^{-8}$ hPa
Pumping system	Dry pumps	Scroll, turbo and ion pumps
Electron beam:		
Electron gun type	No spec	Kimball EGPS-2
Spot size	Below sample dimensions	10 mm^2
Beam current	No spec	$\sim 5.10^{-9}$ A
Primary Energy range	≤15 eV to 1000 eV	5 eV to 1000 eV
Energy accuracy	< 1 eV	<1eV
Charge density	< 100 µC/cm^2	6 µC/cm^2
Pulse or continuous	No spec	Continuous
Total time	No spec	8 min
Incident angle	Higher than 80°	90°
Method:		
Type of calibration	See Annex	Pt sample
Measurement method	As described	Continuous
Measurement accuracy	10%	10%
Extracting field		
Sample bias	No spec	-27,6V
Collector bias	No spec	-

9.5.2 SEY measurement calibration

No supporting material needed.

9.6 ECSS SEY data selection

Table 9-3: SEY parameters of the SEY curves of Al, Cu, Au and Ag samples

Aluminium				
	Average	min	max	Std Val
SEY Max	2.92	2.75	3.11	0.18
E1	16.97	15.85	18.62	1.39
Emax	276	253	291	19

Copper				
	Average	min	max	Std Val
SEY Max	2.48	2.39	2.56	0.08
E1	19.40	17.20	21.61	2.20
Emax	232	218	236	9

Gold				
	Average	min	max	Std Val
Coef Max	2.23	2.12	2.35	0.07
E1	20.96	17.05	27.21	2.58
Emax	212	168	666	34

Silver				
	Average	min	max	Std Val
Coef Max	2.34	2.14	2.54	0.20
E1	19.86	16.82	22.90	3.04
Emax	315	279	351	36

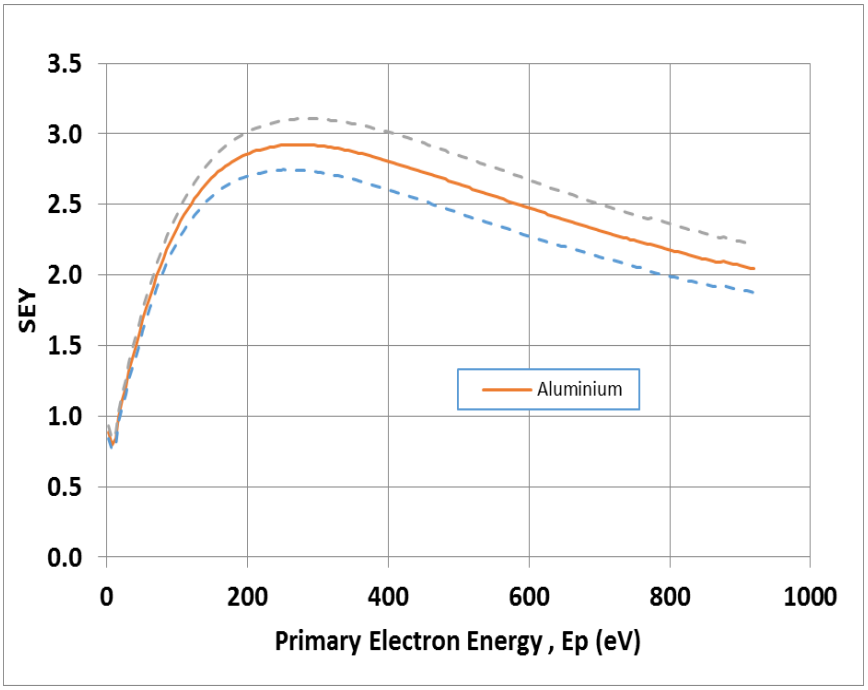


Figure 9-19: SEY as a function of the primary electron energy for aluminium

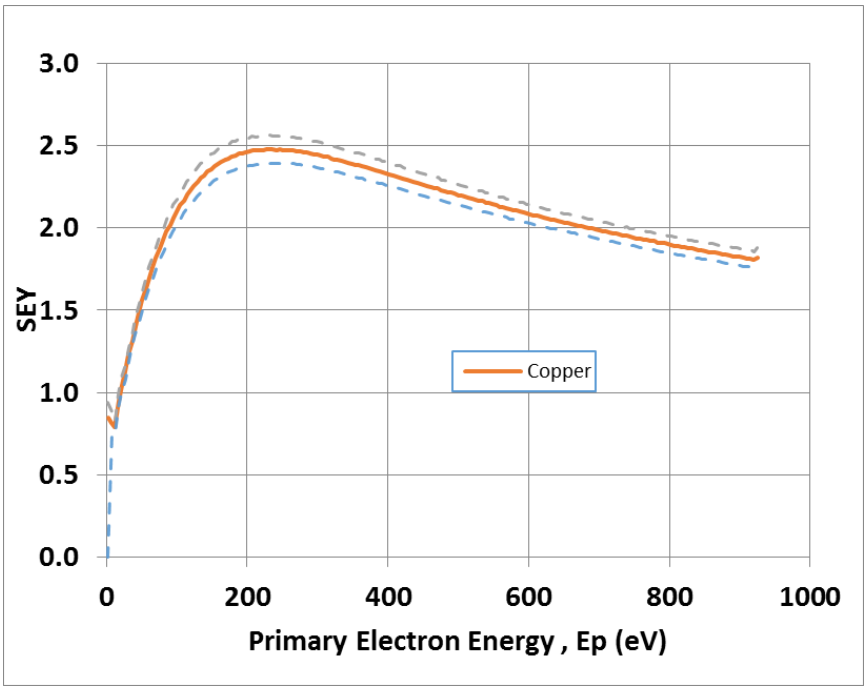


Figure 9-20: SEY as a function of the primary electron energy for copper

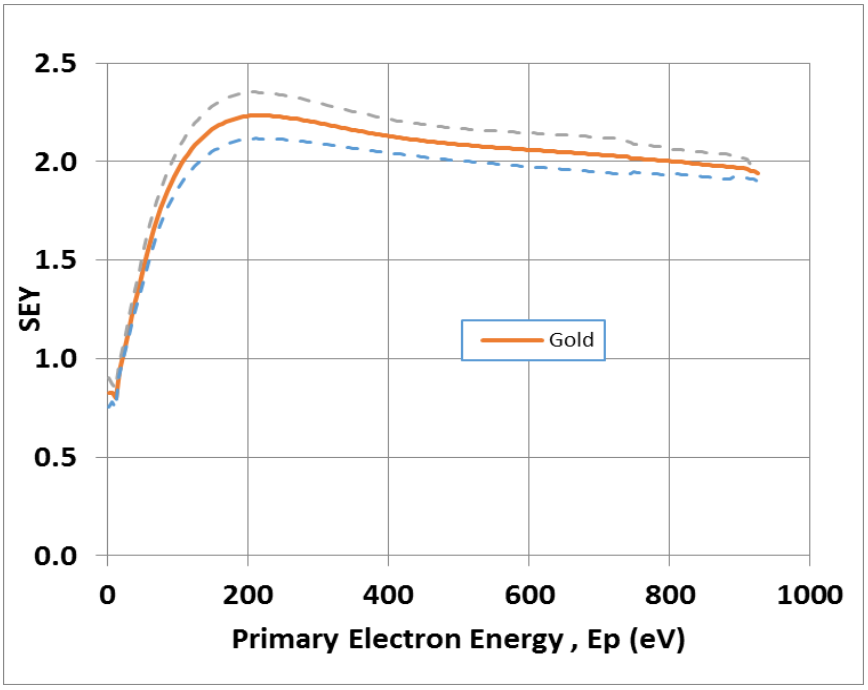


Figure 9-21: SEY as a function of the primary electron energy for gold

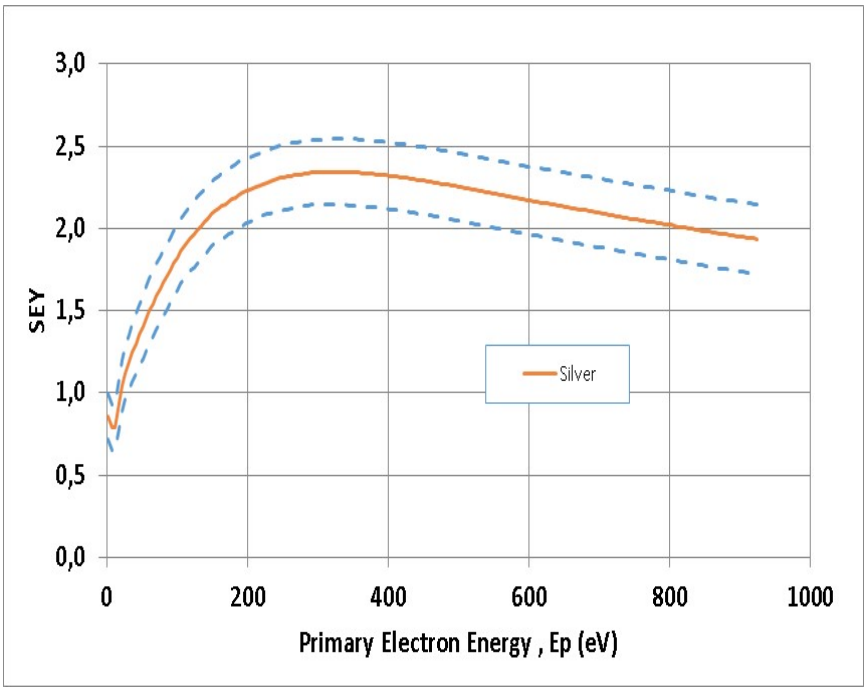


Figure 9-22: SEY as a function of the primary electron energy for silver coatings

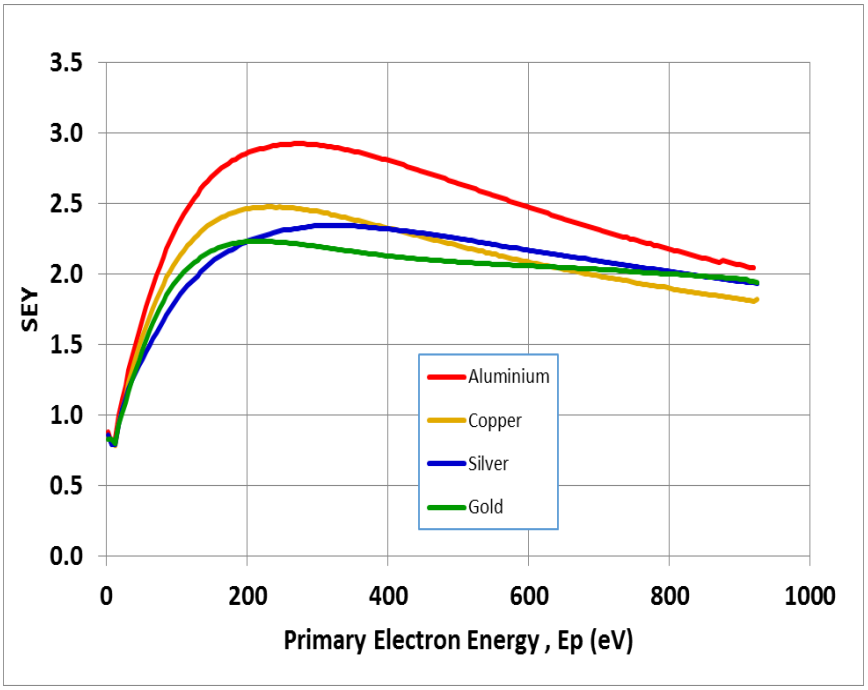


Figure 9-23: Comparison of the SEY curves for Cu, Al, Ag and Au

Table 9-4: SEY curve data for aluminium

Ep(eV)	SEY Average	Std Dev	SEY Average+Std Dev	SEY Average-Std Dev
	Aluminium			
2,3	0,89	0,05	0,93	0,84
7,2	0,80	0,04	0,84	0,76
12,1	0,84	0,05	0,89	0,79
16,9	1,00	0,04	1,04	0,96
21,8	1,11	0,05	1,16	1,06
26,7	1,21	0,05	1,26	1,16
31,6	1,32	0,06	1,38	1,26
36,5	1,41	0,07	1,48	1,34
41,3	1,50	0,07	1,58	1,43
46,2	1,59	0,08	1,67	1,52
51,1	1,68	0,08	1,76	1,61
56,0	1,77	0,08	1,85	1,69
60,9	1,85	0,08	1,93	1,77
65,8	1,92	0,08	2,00	1,84
70,6	1,99	0,08	2,08	1,91
75,5	2,06	0,09	2,14	1,97
80,4	2,12	0,09	2,21	2,03
85,3	2,18	0,09	2,27	2,09
90,2	2,23	0,09	2,33	2,14
95,1	2,29	0,10	2,38	2,19
99,9	2,33	0,10	2,43	2,24
104,8	2,38	0,10	2,48	2,28
109,7	2,42	0,11	2,53	2,32
114,6	2,47	0,11	2,57	2,36
119,5	2,50	0,11	2,61	2,39
124,3	2,54	0,12	2,65	2,42
129,2	2,57	0,12	2,69	2,45
134,1	2,60	0,12	2,73	2,48
139,0	2,63	0,13	2,76	2,51
143,9	2,66	0,13	2,79	2,53
148,8	2,69	0,13	2,82	2,56
153,6	2,71	0,13	2,84	2,58
158,5	2,73	0,14	2,87	2,60
163,4	2,75	0,14	2,89	2,61
168,3	2,77	0,14	2,91	2,63
173,2	2,79	0,14	2,93	2,64
178,0	2,80	0,15	2,95	2,66
182,9	2,82	0,15	2,97	2,67
187,8	2,83	0,15	2,98	2,68
192,7	2,84	0,15	3,00	2,69
197,6	2,85	0,16	3,01	2,70
202,5	2,86	0,16	3,02	2,71
207,3	2,87	0,16	3,03	2,71
212,2	2,88	0,16	3,04	2,72

Ep(eV)	SEY Average	Std Dev	SEY Average+Std Dev	SEY Average-Std Dev
	Aluminium			
217,1	2,89	0,16	3,05	2,72
222,0	2,89	0,17	3,06	2,73
226,9	2,90	0,17	3,07	2,73
231,7	2,90	0,17	3,07	2,74
236,6	2,91	0,17	3,08	2,74
241,5	2,91	0,17	3,09	2,74
246,4	2,92	0,17	3,09	2,74
251,3	2,92	0,17	3,09	2,75
256,2	2,92	0,18	3,10	2,74
261,0	2,92	0,18	3,10	2,74
265,9	2,92	0,18	3,10	2,74
270,8	2,92	0,18	3,11	2,74
275,7	2,92	0,18	3,11	2,74
280,6	2,92	0,18	3,11	2,74
285,4	2,92	0,18	3,11	2,74
290,3	2,92	0,19	3,11	2,74
295,2	2,92	0,19	3,11	2,73
300,1	2,92	0,19	3,11	2,73
305,0	2,91	0,19	3,10	2,73
309,9	2,91	0,19	3,10	2,72
314,7	2,91	0,19	3,10	2,72
319,6	2,90	0,19	3,10	2,71
324,5	2,90	0,19	3,09	2,71
329,4	2,90	0,20	3,09	2,70
334,3	2,89	0,20	3,09	2,70

Ep(eV)	SEY Average	Std Dev	SEY Average+Std Dev	SEY Average-Std Dev
	Aluminium			
339,2	2,89	0,20	3,08	2,69
344,0	2,88	0,20	3,08	2,68
348,9	2,88	0,20	3,07	2,68
353,8	2,87	0,20	3,07	2,67
358,7	2,86	0,20	3,06	2,67
363,6	2,86	0,20	3,06	2,66
368,4	2,85	0,20	3,05	2,65
373,3	2,85	0,20	3,05	2,65
378,2	2,84	0,20	3,04	2,64
383,1	2,83	0,20	3,03	2,63
388,0	2,83	0,20	3,03	2,62
392,9	2,82	0,20	3,02	2,62
397,7	2,81	0,20	3,01	2,61
402,6	2,80	0,20	3,01	2,60
407,5	2,80	0,20	3,00	2,59
412,4	2,79	0,20	2,99	2,59
417,3	2,78	0,20	2,99	2,58
422,1	2,77	0,20	2,98	2,57
427,0	2,77	0,20	2,97	2,56
431,9	2,76	0,20	2,96	2,55
436,8	2,75	0,20	2,96	2,55
441,7	2,74	0,20	2,95	2,54
446,6	2,74	0,20	2,94	2,53
451,4	2,73	0,20	2,93	2,52
456,3	2,72	0,20	2,92	2,51

Ep(eV)	SEY Average	Std Dev	SEY Average+Std Dev	SEY Average-Std Dev
	Aluminium			
461,2	2,71	0,21	2,92	2,51
466,1	2,70	0,20	2,91	2,50
471,0	2,69	0,20	2,90	2,49
475,8	2,69	0,20	2,89	2,48
480,7	2,68	0,21	2,88	2,47
485,6	2,67	0,20	2,87	2,47
490,5	2,66	0,20	2,87	2,46
495,4	2,65	0,20	2,86	2,45
500,3	2,64	0,20	2,85	2,44
505,1	2,64	0,20	2,84	2,43
510,0	2,63	0,20	2,83	2,42
514,9	2,62	0,20	2,82	2,42
519,8	2,61	0,20	2,81	2,41
524,7	2,60	0,20	2,81	2,40
529,5	2,59	0,20	2,80	2,39
534,4	2,59	0,20	2,79	2,38
539,3	2,58	0,20	2,78	2,38
544,2	2,57	0,20	2,77	2,37
549,1	2,56	0,20	2,76	2,36
554,0	2,55	0,20	2,76	2,35
558,8	2,54	0,20	2,75	2,34
563,7	2,54	0,20	2,74	2,34
568,6	2,53	0,20	2,73	2,33
573,5	2,52	0,20	2,72	2,32
578,4	2,51	0,20	2,71	2,31

Ep(eV)	SEY Average	Std Dev	SEY Average+Std Dev	SEY Average-Std Dev
	Aluminium			
583,3	2,50	0,20	2,70	2,30
588,1	2,50	0,20	2,69	2,30
593,0	2,49	0,20	2,69	2,29
597,9	2,48	0,20	2,68	2,28
602,8	2,47	0,20	2,67	2,27
607,7	2,46	0,20	2,66	2,27
612,5	2,45	0,20	2,65	2,26
617,4	2,45	0,20	2,64	2,25
622,3	2,44	0,20	2,63	2,24
627,2	2,43	0,19	2,63	2,24
632,1	2,42	0,19	2,62	2,23
637,0	2,41	0,19	2,61	2,22
641,8	2,41	0,19	2,60	2,21
646,7	2,40	0,19	2,59	2,21
651,6	2,39	0,19	2,59	2,20
656,5	2,38	0,19	2,58	2,19
661,4	2,38	0,19	2,57	2,19
666,2	2,37	0,19	2,56	2,18
671,1	2,36	0,19	2,55	2,17
676,0	2,35	0,19	2,54	2,16
680,9	2,35	0,19	2,54	2,16
685,8	2,34	0,19	2,53	2,15
690,7	2,33	0,19	2,52	2,14
695,5	2,32	0,19	2,51	2,14
700,4	2,32	0,19	2,50	2,13

Ep(eV)	SEY Average	Std Dev	SEY Average+Std Dev	SEY Average-Std Dev
	Aluminium			
705,3	2,31	0,19	2,50	2,12
710,2	2,30	0,19	2,49	2,12
715,1	2,30	0,19	2,48	2,11
719,9	2,29	0,18	2,47	2,10
724,8	2,28	0,18	2,46	2,10
729,7	2,27	0,18	2,46	2,09
734,6	2,27	0,18	2,45	2,08
739,5	2,26	0,18	2,44	2,08
744,4	2,25	0,18	2,43	2,07
749,2	2,25	0,18	2,43	2,06
754,1	2,24	0,18	2,42	2,06
759,0	2,23	0,18	2,41	2,05
763,9	2,22	0,18	2,40	2,04
768,8	2,22	0,18	2,40	2,04
773,6	2,21	0,19	2,40	2,02
778,5	2,21	0,19	2,40	2,02
783,4	2,20	0,19	2,39	2,01
788,3	2,19	0,19	2,38	2,01
793,2	2,19	0,19	2,38	2,00
798,1	2,18	0,19	2,37	1,99
802,9	2,18	0,19	2,36	1,99
807,8	2,17	0,19	2,35	1,98
812,7	2,16	0,19	2,35	1,98
817,6	2,16	0,18	2,34	1,97
822,5	2,15	0,18	2,33	1,97
827,4	2,14	0,18	2,33	1,96
832,2	2,14	0,18	2,32	1,95
837,1	2,13	0,18	2,31	1,95
842,0	2,12	0,18	2,30	1,94
846,9	2,12	0,18	2,30	1,94
851,8	2,11	0,18	2,29	1,93
856,6	2,11	0,18	2,29	1,93
861,5	2,10	0,18	2,28	1,92
866,4	2,09	0,18	2,27	1,92
871,3	2,09	0,18	2,26	1,91
876,2	2,10	0,17	2,27	1,92
881,1	2,09	0,17	2,26	1,92
885,9	2,08	0,17	2,26	1,91
890,8	2,08	0,17	2,25	1,91
895,7	2,07	0,17	2,24	1,90
900,6	2,07	0,17	2,24	1,90
905,5	2,06	0,17	2,23	1,89
910,3	2,05	0,17	2,22	1,89
915,2	2,05	0,17	2,22	1,88
920,1	2,04	0,17	2,21	1,88
924,99	2,03	0,21	2,25	1,82

Table 9-5: SEY curve data for copper.

Ep(eV)	SEY Average	Std Dev	SEY Average+Std Dev	SEY Average-Std Dev
2,3	0,85	0,09	0,94	0,00
7,2	0,82	0,06	0,88	0,76
12,1	0,79	0,03	0,82	0,76
16,9	0,95	0,04	0,99	0,91
21,8	1,05	0,05	1,10	1,00
26,7	1,13	0,05	1,17	1,08
31,6	1,23	0,04	1,27	1,19
36,5	1,31	0,03	1,35	1,28
41,3	1,40	0,05	1,45	1,36
46,2	1,49	0,05	1,54	1,43
51,1	1,56	0,06	1,62	1,50
56,0	1,63	0,06	1,69	1,57
60,9	1,70	0,07	1,77	1,63
65,8	1,76	0,07	1,83	1,70
70,6	1,82	0,07	1,89	1,75
75,5	1,88	0,07	1,95	1,80
80,4	1,93	0,07	2,00	1,85
85,3	1,98	0,08	2,05	1,90
90,2	2,02	0,07	2,09	1,94
95,1	2,06	0,08	2,14	1,98
99,9	2,10	0,08	2,17	2,02
104,8	2,14	0,08	2,22	2,05
109,7	2,17	0,08	2,25	2,09
114,6	2,20	0,08	2,29	2,12
119,5	2,23	0,08	2,31	2,15
124,3	2,26	0,09	2,34	2,17
129,2	2,28	0,08	2,36	2,19
134,1	2,30	0,09	2,39	2,22
139,0	2,32	0,08	2,40	2,23
143,9	2,34	0,09	2,43	2,25
148,8	2,36	0,09	2,45	2,27
153,6	2,37	0,08	2,46	2,29
158,5	2,39	0,09	2,48	2,30
163,4	2,40	0,08	2,49	2,32
168,3	2,41	0,09	2,50	2,33
173,2	2,42	0,09	2,51	2,34
178,0	2,44	0,09	2,52	2,35
182,9	2,44	0,09	2,53	2,36
187,8	2,45	0,09	2,54	2,37
192,7	2,46	0,08	2,54	2,37
197,6	2,46	0,09	2,55	2,38
202,5	2,46	0,08	2,55	2,38
207,3	2,47	0,09	2,56	2,38
212,2	2,47	0,08	2,55	2,39
217,1	2,47	0,09	2,56	2,39
222,0	2,47	0,08	2,55	2,39
226,9	2,48	0,08	2,56	2,39
231,7	2,48	0,08	2,56	2,39
236,6	2,48	0,08	2,56	2,39

Ep(eV)	SEY Average	Std Dev	SEY Average+Std Dev	SEY Average-Std Dev
241,5	2,47	0,08	2,56	2,39
246,4	2,48	0,08	2,56	2,39
251,3	2,47	0,08	2,56	2,39
256,2	2,47	0,08	2,56	2,39
261,0	2,47	0,08	2,55	2,39
265,9	2,47	0,08	2,55	2,39
270,8	2,47	0,08	2,54	2,39
275,7	2,46	0,08	2,54	2,38
280,6	2,46	0,08	2,54	2,38
285,4	2,46	0,08	2,54	2,38
290,3	2,45	0,08	2,53	2,38
295,2	2,45	0,08	2,53	2,37
300,1	2,45	0,08	2,52	2,37
305,0	2,44	0,08	2,52	2,36
309,9	2,43	0,08	2,51	2,36
314,7	2,43	0,08	2,51	2,35
319,6	2,42	0,08	2,50	2,35
324,5	2,42	0,08	2,49	2,34
329,4	2,41	0,08	2,49	2,34
334,3	2,41	0,08	2,48	2,33
339,2	2,40	0,07	2,48	2,33
344,0	2,40	0,08	2,47	2,32
348,9	2,39	0,07	2,47	2,32
353,8	2,38	0,07	2,46	2,31
358,7	2,38	0,08	2,46	2,30

Ep(eV)	SEY Average	Std Dev	SEY Average+Std Dev	SEY Average-Std Dev
363,6	2,37	0,07	2,45	2,30
368,4	2,37	0,08	2,44	2,29
373,3	2,36	0,07	2,43	2,29
378,2	2,36	0,07	2,43	2,28
383,1	2,35	0,07	2,42	2,28
388,0	2,35	0,07	2,42	2,27
392,9	2,34	0,07	2,41	2,27
397,7	2,33	0,07	2,40	2,26
402,6	2,33	0,07	2,39	2,26
407,5	2,32	0,07	2,39	2,25
412,4	2,31	0,07	2,38	2,25
417,3	2,31	0,07	2,38	2,24
422,1	2,30	0,07	2,37	2,23
427,0	2,29	0,07	2,36	2,22
431,9	2,29	0,07	2,36	2,22
436,8	2,28	0,07	2,35	2,21
441,7	2,28	0,07	2,34	2,21
446,6	2,27	0,07	2,33	2,20
451,4	2,26	0,07	2,33	2,20
456,3	2,25	0,07	2,32	2,19
461,2	2,25	0,07	2,32	2,18
466,1	2,24	0,06	2,31	2,18
471,0	2,24	0,07	2,31	2,17
475,8	2,23	0,06	2,29	2,17
480,7	2,23	0,07	2,29	2,16

Ep(eV)	SEY Average	Std Dev	SEY Average+Std Dev	SEY Average-Std Dev
485,6	2,22	0,06	2,28	2,16
490,5	2,21	0,07	2,28	2,15
495,4	2,21	0,06	2,27	2,15
500,3	2,20	0,06	2,26	2,14
505,1	2,20	0,06	2,26	2,13
510,0	2,19	0,06	2,25	2,13
514,9	2,18	0,06	2,24	2,12
519,8	2,18	0,06	2,24	2,12
524,7	2,17	0,06	2,23	2,11
529,5	2,16	0,06	2,23	2,10
534,4	2,16	0,06	2,22	2,10
539,3	2,15	0,06	2,21	2,10
544,2	2,15	0,06	2,21	2,09
549,1	2,14	0,06	2,20	2,09
554,0	2,14	0,06	2,20	2,08
558,8	2,13	0,06	2,19	2,07
563,7	2,13	0,06	2,19	2,07
568,6	2,12	0,06	2,18	2,07
573,5	2,12	0,06	2,18	2,06
578,4	2,11	0,06	2,16	2,05
583,3	2,11	0,06	2,16	2,05
588,1	2,10	0,06	2,15	2,04
593,0	2,09	0,06	2,15	2,04
597,9	2,09	0,06	2,14	2,03
602,8	2,08	0,06	2,14	2,03

Ep(eV)	SEY Average	Std Dev	SEY Average+Std Dev	SEY Average-Std Dev
607,7	2,08	0,06	2,13	2,02
612,5	2,07	0,06	2,13	2,02
617,4	2,07	0,06	2,12	2,01
622,3	2,06	0,06	2,12	2,01
627,2	2,06	0,06	2,11	2,00
632,1	2,05	0,06	2,11	2,00
637,0	2,05	0,05	2,10	1,99
641,8	2,04	0,06	2,10	1,99
646,7	2,04	0,05	2,09	1,98
651,6	2,03	0,05	2,09	1,98
656,5	2,03	0,05	2,08	1,98
661,4	2,02	0,05	2,08	1,97
666,2	2,02	0,05	2,07	1,97
671,1	2,01	0,05	2,07	1,96
676,0	2,01	0,05	2,06	1,96
680,9	2,00	0,05	2,06	1,95
685,8	2,00	0,05	2,05	1,95
690,7	2,00	0,05	2,05	1,94
695,5	1,99	0,05	2,04	1,94
700,4	1,99	0,05	2,04	1,93
705,3	1,98	0,05	2,03	1,93
710,2	1,98	0,05	2,03	1,93
715,1	1,97	0,05	2,02	1,92
719,9	1,97	0,05	2,02	1,92
724,8	1,97	0,05	2,02	1,91

Ep(eV)	SEY Average	Std Dev	SEY Average+Std Dev	SEY Average-Std Dev
729,7	1,96	0,05	2,02	1,91
734,6	1,95	0,05	2,00	1,91
739,5	1,95	0,05	2,01	1,90
744,4	1,95	0,05	2,00	1,90
749,2	1,94	0,05	1,99	1,89
754,1	1,94	0,05	1,99	1,88
759,0	1,94	0,05	1,99	1,88
763,9	1,93	0,05	1,98	1,88
768,8	1,93	0,05	1,98	1,88
773,6	1,92	0,05	1,97	1,87
778,5	1,92	0,05	1,97	1,87
783,4	1,91	0,05	1,96	1,86
788,3	1,91	0,05	1,96	1,86
793,2	1,91	0,05	1,96	1,86
798,1	1,90	0,05	1,95	1,85
802,9	1,90	0,05	1,95	1,84
807,8	1,89	0,05	1,94	1,84
812,7	1,89	0,05	1,95	1,84
817,6	1,89	0,05	1,94	1,83
822,5	1,88	0,05	1,94	1,83
827,4	1,88	0,05	1,93	1,83
832,2	1,87	0,05	1,93	1,82
837,1	1,87	0,05	1,92	1,82
842,0	1,87	0,05	1,92	1,81
846,9	1,86	0,05	1,91	1,81

Ep(eV)	SEY Average	Std Dev	SEY Average+Std Dev	SEY Average-Std Dev
851,8	1,86	0,05	1,91	1,81
856,6	1,85	0,05	1,91	1,80
861,5	1,85	0,05	1,90	1,80
866,4	1,85	0,05	1,90	1,80
871,3	1,85	0,05	1,90	1,80
876,2	1,84	0,05	1,90	1,79
881,1	1,84	0,05	1,89	1,79
885,9	1,84	0,05	1,89	1,78
890,8	1,83	0,05	1,88	1,78
895,7	1,83	0,05	1,88	1,78
900,6	1,82	0,05	1,88	1,77
905,5	1,82	0,05	1,87	1,77
910,3	1,82	0,05	1,86	1,77
915,2	1,81	0,05	1,87	1,76
920,1	1,81	0,05	1,86	1,76
925,0	1,82	0,06	1,88	1,76

Table 9-6: SEY curve data for gold

Ep(eV)	SEY Average	Std Dev	SEY Average+Std Dev	SEY Average-Std Dev
2,3	0,83	0,08	0,91	0,75
7,2	0,83	0,04	0,87	0,78
12,1	0,80	0,05	0,85	0,75
16,9	0,94	0,03	0,97	0,91
21,8	1,01	0,03	1,05	0,98
26,7	1,09	0,04	1,13	1,05
31,6	1,17	0,05	1,22	1,12
36,5	1,25	0,05	1,31	1,20
41,3	1,32	0,06	1,37	1,26
46,2	1,38	0,06	1,45	1,32
51,1	1,46	0,08	1,54	1,38
56,0	1,53	0,08	1,62	1,45
60,9	1,60	0,08	1,68	1,51
65,8	1,66	0,09	1,74	1,57
70,6	1,71	0,09	1,80	1,63
75,5	1,76	0,09	1,85	1,68
80,4	1,81	0,09	1,90	1,72
85,3	1,85	0,09	1,94	1,76
90,2	1,89	0,09	1,98	1,80
95,1	1,92	0,10	2,02	1,83
99,9	1,96	0,10	2,05	1,86
104,8	1,99	0,10	2,09	1,89
109,7	2,01	0,10	2,12	1,91
114,6	2,04	0,11	2,14	1,93
119,5	2,06	0,11	2,17	1,95
124,3	2,08	0,11	2,19	1,97
129,2	2,10	0,11	2,21	1,99
134,1	2,12	0,11	2,23	2,01
139,0	2,14	0,11	2,25	2,02
143,9	2,15	0,11	2,26	2,04
148,8	2,16	0,11	2,28	2,05
153,6	2,17	0,11	2,29	2,06
158,5	2,18	0,12	2,30	2,07
163,4	2,19	0,12	2,31	2,08
168,3	2,20	0,12	2,32	2,08
173,2	2,21	0,12	2,33	2,09
178,0	2,22	0,12	2,33	2,10
182,9	2,22	0,12	2,34	2,10
187,8	2,23	0,12	2,34	2,11
192,7	2,23	0,12	2,35	2,11
197,6	2,23	0,12	2,35	2,11
202,5	2,23	0,12	2,35	2,11
207,3	2,23	0,12	2,35	2,12
212,2	2,23	0,12	2,35	2,12
217,1	2,23	0,12	2,35	2,12
222,0	2,23	0,12	2,35	2,12
226,9	2,23	0,12	2,35	2,12
231,7	2,23	0,12	2,35	2,12
236,6	2,23	0,11	2,34	2,12

Ep(eV)	SEY Average	Std Dev	SEY Average+Std Dev	SEY Average-Std Dev
241,5	2,23	0,11	2,34	2,12
246,4	2,23	0,11	2,34	2,11
251,3	2,23	0,11	2,34	2,11
256,2	2,22	0,11	2,34	2,11
261,0	2,22	0,11	2,33	2,11
265,9	2,22	0,11	2,33	2,11
270,8	2,22	0,11	2,32	2,11
275,7	2,21	0,11	2,32	2,10
280,6	2,21	0,11	2,32	2,10
285,4	2,21	0,11	2,31	2,10
290,3	2,20	0,10	2,31	2,10
295,2	2,20	0,10	2,30	2,10
300,1	2,20	0,10	2,30	2,09
305,0	2,19	0,10	2,30	2,09
309,9	2,19	0,10	2,29	2,09
314,7	2,19	0,10	2,29	2,09
319,6	2,18	0,10	2,28	2,08
324,5	2,18	0,10	2,28	2,08
329,4	2,18	0,10	2,27	2,08
334,3	2,17	0,10	2,27	2,08
339,2	2,17	0,10	2,26	2,07
344,0	2,17	0,09	2,26	2,07
348,9	2,16	0,09	2,26	2,07
353,8	2,16	0,09	2,25	2,07
358,7	2,16	0,09	2,25	2,06

Ep(eV)	SEY Average	Std Dev	SEY Average+Std Dev	SEY Average-Std Dev
363,6	2,15	0,09	2,24	2,06
368,4	2,15	0,09	2,24	2,06
373,3	2,15	0,09	2,24	2,06
378,2	2,14	0,09	2,23	2,05
383,1	2,14	0,09	2,23	2,05
388,0	2,14	0,09	2,22	2,05
392,9	2,13	0,09	2,22	2,05
397,7	2,13	0,09	2,22	2,05
402,6	2,13	0,09	2,21	2,04
407,5	2,13	0,09	2,21	2,04
412,4	2,12	0,08	2,21	2,04
417,3	2,12	0,08	2,20	2,04
422,1	2,12	0,08	2,20	2,03
427,0	2,12	0,08	2,20	2,03
431,9	2,11	0,08	2,20	2,03
436,8	2,11	0,08	2,19	2,03
441,7	2,11	0,08	2,19	2,03
446,6	2,11	0,08	2,19	2,03
451,4	2,10	0,08	2,19	2,02
456,3	2,10	0,08	2,19	2,02
461,2	2,10	0,08	2,18	2,02
466,1	2,10	0,08	2,18	2,02
471,0	2,10	0,08	2,18	2,02
475,8	2,10	0,08	2,18	2,01
480,7	2,09	0,08	2,17	2,01

Ep(eV)	SEY Average	Std Dev	SEY Average+Std Dev	SEY Average-Std Dev
485,6	2,09	0,08	2,17	2,01
490,5	2,09	0,08	2,17	2,01
495,4	2,09	0,08	2,17	2,01
500,3	2,09	0,08	2,17	2,01
505,1	2,09	0,08	2,17	2,00
510,0	2,08	0,08	2,17	2,00
514,9	2,08	0,08	2,16	2,00
519,8	2,08	0,08	2,16	2,00
524,7	2,08	0,08	2,16	2,00
529,5	2,08	0,08	2,16	2,00
534,4	2,08	0,08	2,16	1,99
539,3	2,08	0,08	2,16	1,99
544,2	2,07	0,08	2,16	1,99
549,1	2,07	0,08	2,16	1,99
554,0	2,07	0,08	2,15	1,99
558,8	2,07	0,08	2,15	1,99
563,7	2,07	0,08	2,15	1,99
568,6	2,07	0,08	2,15	1,98
573,5	2,07	0,08	2,15	1,98
578,4	2,06	0,08	2,15	1,98
583,3	2,06	0,08	2,15	1,98
588,1	2,06	0,09	2,15	1,98
593,0	2,06	0,09	2,15	1,98
597,9	2,06	0,09	2,15	1,98
602,8	2,06	0,09	2,14	1,97

Ep(eV)	SEY Average	Std Dev	SEY Average+Std Dev	SEY Average-Std Dev
607,7	2,06	0,09	2,14	1,97
612,5	2,06	0,09	2,14	1,97
617,4	2,06	0,09	2,14	1,97
622,3	2,05	0,09	2,14	1,97
627,2	2,05	0,09	2,14	1,97
632,1	2,05	0,09	2,14	1,97
637,0	2,05	0,09	2,14	1,96
641,8	2,05	0,09	2,14	1,96
646,7	2,05	0,09	2,14	1,96
651,6	2,05	0,09	2,13	1,96
656,5	2,05	0,09	2,13	1,96
661,4	2,05	0,09	2,13	1,96
666,2	2,04	0,09	2,13	1,96
671,1	2,04	0,09	2,13	1,95
676,0	2,04	0,09	2,13	1,95
680,9	2,04	0,09	2,13	1,95
685,8	2,04	0,09	2,13	1,95
690,7	2,04	0,09	2,13	1,95
695,5	2,04	0,09	2,12	1,95
700,4	2,03	0,09	2,12	1,95
705,3	2,03	0,09	2,12	1,94
710,2	2,03	0,09	2,12	1,94
715,1	2,03	0,09	2,12	1,94
719,9	2,03	0,09	2,12	1,94
724,8	2,03	0,09	2,12	1,94

Ep(eV)	SEY Average	Std Dev	SEY Average+Std Dev	SEY Average-Std Dev
729,7	2,03	0,09	2,12	1,94
734,6	2,03	0,08	2,11	1,95
739,5	2,02	0,08	2,10	1,94
744,4	2,02	0,08	2,10	1,94
749,2	2,02	0,07	2,09	1,95
754,1	2,02	0,07	2,09	1,95
759,0	2,01	0,07	2,08	1,94
763,9	2,01	0,07	2,08	1,94
768,8	2,01	0,07	2,08	1,94
773,6	2,01	0,07	2,08	1,94
778,5	2,01	0,07	2,08	1,94
783,4	2,01	0,07	2,08	1,94
788,3	2,00	0,07	2,07	1,93
793,2	2,00	0,07	2,07	1,93
798,1	2,00	0,07	2,07	1,93
802,9	2,00	0,06	2,06	1,94
807,8	2,00	0,06	2,06	1,94
812,7	2,00	0,06	2,06	1,94
817,6	2,00	0,06	2,06	1,94
822,5	2,00	0,06	2,06	1,93
827,4	1,99	0,06	2,05	1,93
832,2	1,99	0,06	2,05	1,93
837,1	1,99	0,06	2,05	1,93
842,0	1,99	0,06	2,05	1,93
846,9	1,99	0,06	2,05	1,92

Ep(eV)	SEY Average	Std Dev	SEY Average+Std Dev	SEY Average-Std Dev
851,8	1,98	0,06	2,05	1,92
856,6	1,98	0,06	2,05	1,92
861,5	1,98	0,06	2,04	1,92
866,4	1,98	0,06	2,04	1,92
871,3	1,98	0,06	2,04	1,92
876,2	1,98	0,06	2,04	1,91
881,1	1,97	0,06	2,04	1,91
885,9	1,97	0,06	2,03	1,91
890,8	1,97	0,05	2,02	1,92
895,7	1,97	0,05	2,02	1,92
900,6	1,97	0,05	2,02	1,92
905,5	1,97	0,05	2,02	1,92
910,3	1,96	0,05	2,01	1,91
915,2	1,95	0,04	1,99	1,91
920,1	1,95	0,04	1,99	1,91
925,0	1,94	0,04	1,98	1,90

Table 9-7: SEY curve data for silver

Ep(eV)	SEY Average	Std Dev	SEY Average+Std Dev	SEY Average-Std Dev
2,29	0,86	0,14	0,99	0,72
7,2	0,79	0,14	0,93	0,66
12,1	0,79	0,14	0,93	0,65
16,9	0,93	0,15	1,08	0,79
21,8	1,04	0,15	1,20	0,89
26,7	1,12	0,16	1,28	0,96
31,6	1,19	0,17	1,36	1,02
36,5	1,25	0,18	1,42	1,07
41,3	1,30	0,18	1,48	1,12
46,2	1,35	0,19	1,54	1,17
51,1	1,40	0,19	1,59	1,21
56,0	1,45	0,20	1,64	1,25
60,9	1,50	0,20	1,69	1,30
65,8	1,54	0,20	1,74	1,34
70,6	1,59	0,20	1,79	1,39
75,5	1,63	0,20	1,83	1,43
80,4	1,67	0,20	1,87	1,47
85,3	1,71	0,20	1,91	1,51
90,2	1,75	0,20	1,94	1,55
95,1	1,78	0,20	1,98	1,59
99,9	1,82	0,19	2,02	1,63
104,8	1,86	0,20	2,05	1,66
109,7	1,89	0,20	2,09	1,70
114,6	1,92	0,20	2,12	1,72
119,5	1,94	**0,20**	2,14	1,74
124,3	1,97	0,20	2,17	1,76
129,2	1,99	0,20	2,19	1,79
134,1	2,01	0,20	2,22	1,81
139,0	2,04	0,20	2,24	1,84
143,9	2,06	0,20	2,26	1,86
148,8	2,09	0,20	2,28	1,89
153,6	2,10	0,20	2,30	1,91
158,5	2,12	0,20	2,32	1,92
163,4	2,13	0,20	2,33	1,94
168,3	2,15	0,20	2,35	1,95
173,2	2,16	0,20	2,36	1,96
178,0	2,18	0,20	2,38	1,98
182,9	2,19	0,20	2,39	1,99
187,8	2,20	0,20	2,40	2,00
192,7	2,22	0,20	2,41	2,02
197,6	2,23	0,20	2,43	2,03
202,5	2,24	0,20	2,44	2,04
207,3	2,25	0,20	2,44	2,05
212,2	2,25	0,19	2,45	2,06
217,1	2,26	0,19	2,46	2,07
222,0	2,27	0,19	2,46	2,08
226,9	2,28	0,19	2,47	2,09
231,7	2,29	0,19	2,48	2,09
236,6	2,29	0,20	2,49	2,10

Ep(eV)	SEY Average	Std Dev	SEY Average+Std Dev	SEY Average-Std Dev
241,5	2,30	0,20	2,50	2,10
246,4	2,31	0,20	2,50	2,11
251,3	2,31	0,20	2,51	2,11
256,2	2,32	0,20	2,52	2,12
261,0	2,32	0,20	2,52	2,12
265,9	2,32	0,20	2,52	2,12
270,8	2,33	0,20	2,52	2,13
275,7	2,33	0,20	2,53	2,13
280,6	2,33	0,20	2,53	2,14
285,4	2,34	0,20	2,53	2,14
290,3	2,34	0,20	2,54	2,14
295,2	2,34	0,20	2,54	2,14
300,1	2,34	0,20	2,54	2,15
305,0	2,34	0,20	2,54	2,15
309,9	2,34	0,20	2,54	2,14
314,7	2,34	0,20	2,54	2,14
319,6	2,34	0,20	2,54	2,14
324,5	2,34	0,20	2,54	2,14
329,4	2,34	0,20	2,54	2,14
334,3	2,34	0,20	2,54	2,14
339,2	2,34	0,20	2,54	2,14
344,0	2,34	0,20	2,54	2,14
348,9	2,34	0,20	2,54	2,14
353,8	2,34	0,20	2,54	2,14
358,7	2,34	0,20	2,54	2,14

Ep(eV)	SEY Average	Std Dev	SEY Average+Std Dev	SEY Average-Std Dev
363,6	2,34	0,20	2,54	2,13
368,4	2,33	0,20	2,54	2,13
373,3	2,33	0,20	2,54	2,13
378,2	2,33	0,20	2,53	2,13
383,1	2,33	0,20	2,53	2,13
388,0	2,33	0,20	2,53	2,12
392,9	2,32	0,20	2,53	2,12
397,7	2,32	0,20	2,53	2,12
402,6	2,32	0,20	2,52	2,12
407,5	2,32	0,20	2,52	2,11
412,4	2,31	0,20	2,52	2,11
417,3	2,31	0,20	2,51	2,11
422,1	2,31	0,20	2,51	2,10
427,0	2,31	0,20	2,51	2,10
431,9	2,30	0,20	2,51	2,10
436,8	2,30	0,20	2,50	2,09
441,7	2,30	0,20	2,50	2,09
446,6	2,29	0,20	2,50	2,09
451,4	2,29	0,20	2,49	2,09
456,3	2,29	0,20	2,49	2,08
461,2	2,28	0,20	2,49	2,08
466,1	2,28	0,20	2,48	2,07
471,0	2,27	0,20	2,48	2,07
475,8	2,27	0,20	2,48	2,07
480,7	2,27	0,20	2,47	2,06

Ep(eV)	SEY Average	Std Dev	SEY Average+Std Dev	SEY Average-Std Dev
485,6	2,27	0,21	2,47	2,06
490,5	2,26	0,21	2,47	2,06
495,4	2,26	0,21	2,46	2,05
500,3	2,25	0,21	2,46	2,05
505,1	2,25	0,21	2,45	2,04
510,0	2,24	0,21	2,45	2,04
514,9	2,24	0,21	2,45	2,04
519,8	2,24	0,21	2,44	2,03
524,7	2,23	0,21	2,44	2,03
529,5	2,23	0,21	2,43	2,02
534,4	2,22	0,21	2,43	2,02
539,3	2,22	0,21	2,43	2,01
544,2	2,22	0,21	2,42	2,01
549,1	2,21	0,21	2,42	2,01
554,0	2,21	0,21	2,41	2,00
558,8	2,20	0,21	2,41	2,00
563,7	2,20	0,21	2,41	1,99
568,6	2,20	0,21	2,40	1,99
573,5	2,19	0,21	2,40	1,99
578,4	2,19	0,21	2,40	1,98
583,3	2,18	0,21	2,39	1,98
588,1	2,18	0,21	2,39	1,97
593,0	2,18	0,21	2,38	1,97
597,9	2,17	0,21	2,38	1,96
602,8	2,17	0,21	2,38	1,96

Ep(eV)	SEY Average	Std Dev	SEY Average+Std Dev	SEY Average-Std Dev
607,7	2,17	0,21	2,37	1,96
612,5	2,16	0,21	2,37	1,95
617,4	2,16	0,21	2,36	1,95
622,3	2,15	0,21	2,36	1,95
627,2	2,15	0,21	2,36	1,94
632,1	2,15	0,21	2,35	1,94
637,0	2,14	0,21	2,35	1,94
641,8	2,14	0,21	2,35	1,93
646,7	2,14	0,21	2,34	1,93
651,6	2,13	0,21	2,34	1,92
656,5	2,13	0,21	2,34	1,92
661,4	2,12	0,21	2,33	1,92
666,2	2,12	0,21	2,33	1,91
671,1	2,12	0,21	2,32	1,91
676,0	2,11	0,21	2,32	1,91
680,9	2,11	0,21	2,32	1,90
685,8	2,11	0,21	2,31	1,90
690,7	2,10	0,21	2,31	1,89
695,5	2,10	0,21	2,31	1,89
700,4	2,09	0,21	2,30	1,89
705,3	2,09	0,21	2,30	1,88
710,2	2,09	0,21	2,29	1,88
715,1	2,08	0,21	2,29	1,87
719,9	2,08	0,21	2,29	1,87
724,8	2,07	0,21	2,28	1,87

Ep(eV)	SEY Average	Std Dev	SEY Average+Std Dev	SEY Average-Std Dev
729,7	2,07	0,21	2,28	1,86
734,6	2,07	0,21	2,28	1,86
739,5	2,06	0,21	2,27	1,86
744,4	2,06	0,21	2,27	1,85
749,2	2,06	0,21	2,27	1,85
754,1	2,05	0,21	2,26	1,84
759,0	2,05	0,21	2,26	1,84
763,9	2,05	0,21	2,25	1,84
768,8	2,04	0,21	2,25	1,83
773,6	2,04	0,21	2,25	1,83
778,5	2,04	0,21	2,25	1,83
783,4	2,03	0,21	2,24	1,82
788,3	2,03	0,21	2,24	1,82
793,2	2,03	0,21	2,24	1,82
798,1	2,02	0,21	2,23	1,81
802,9	2,02	0,21	2,23	1,81
807,8	2,01	0,21	2,22	1,80
812,7	2,01	0,21	2,22	1,80
817,6	2,01	0,21	2,22	1,80
822,5	2,00	0,21	2,21	1,79
827,4	2,00	0,21	2,21	1,79

Ep(eV)	SEY Average	Std Dev	SEY Average+Std Dev	SEY Average-Std Dev
832,2	2,00	0,21	2,21	1,79
837,1	1,99	0,21	2,20	1,78
842,0	1,99	0,21	2,20	1,78
846,9	1,99	0,21	2,20	1,78
851,8	1,98	0,21	2,19	1,77
856,6	1,98	0,21	2,19	1,77
861,5	1,98	0,21	2,19	1,77
866,4	1,97	0,21	2,18	1,76
871,3	1,97	0,21	2,18	1,76
876,2	1,97	0,21	2,18	1,75
881,1	1,96	0,21	2,17	1,75
885,9	1,96	0,21	2,17	1,75
890,8	1,96	0,21	2,17	1,75
895,7	1,95	0,21	2,16	1,74
900,6	1,95	0,21	2,16	1,74
905,5	1,95	0,21	2,16	1,74
910,3	1,94	0,21	2,15	1,73
915,2	1,94	0,21	2,15	1,73
920,1	1,94	0,21	2,15	1,73
924,99	1,94	0,21	2,15	1,73

9.7 Bibliography for clause 9

[9-1] R. Cimino, SLAC-PUB-10350, February 2004.

[9-2] A. Woode, J.Petit, Diagnostic Investigations into the Multipactor Effect, Susceptibility Zone Measurements and Parameters Affecting A Discharge, in: ESTEC Working

[9-3] L. Aguilera, I. Montero, M.E. Dávila, L. Sacedón, V. Nistor, L. Galán, D. Raboso, S. Anza, C. Vicente, J. Gil., ESA Survey on Secondary Emission Yield of Industry Materials and Their Impact on Multipactor Threshold in: E. ESTEC (Ed.) MULCOPIM 2011, Noordwijk.

[9-4] A.L. Gilardini, G.E.W. B., v.E. A., New breakdown modes of the multipacting discharge, Journal of Applied Physics, 71 (1992) 4629-4631.

[9-5] M. Belhaj, T. Tondu, V. Inguimbert, B. Pierre, S. François, G. Alix, The effects of incident electron current density and temperature on the total electron emission yield of polycrystalline CVD diamond, Journal of Physics D: Applied Physics, 43 (2010) 135303.

[9-6] M. Belhaj, T. Tondu, V. Inguimbert, B. Elsafi, S. Fakhfakh, O. Jbara, Electron emission yield and charging process of alkali-silicate glass submitted to an electron beam under the varying temperature condition, 2011.

[9-7] O. Brüning, F. Caspers, I.R. Collins, O. Gröobner, B. Henrist, N. Hilleret, J.M. Laurent, M. Morvillo, M. Pivi, F. Ruggiero, X. Zhang, Electron cloud and beam scrubbing in the LHC, in: Proceedings of the 1999 Particle Accelerator Conference, New York

[9-8] I. Montero, L. Aguilera, M.E. Davila, V.C. Nistor, L.A. Gonzalez, L. Galan, D. Raboso, R. Ferritto, Secondary electron emission under electron bombardment from graphene nanoplatelets, Applied Surface Science, 291 (2014) 74-77.

[9-9] I. Montero, L.Aguilera, U. Wochner, D.Raboso, Antimultipactor device, patent EP3196917A1, 2014

[9-10] L. Austin, H. Starke, Ueber die Reflexion der Kathodenstrahlen und eine damit verbundene neue Erscheinung secundärer Emission, Annalen der Physik, 314 (1902) 271-292.

[9-11] J. Dennison, J. Christensen, J. Dekany, C. Thomson, N. Nickles, R.E. Davies, M. Belhaj, K. Toyoda, K. Kawasaki, I. Montero, M.E. Dávil, L. Olano, L. Galán, Absolute Electron Emission Calibration: Round Robin Test of Au and graphite, 14th Spacecraft Charging Technology Conference, Noordwijk, NL (2016).

[9-12] E. McCafferty, J.P. Wightman, Determination of the concentration of surface hydroxyl groups on metal oxide films by a quantitative XPS method, Surface and Interface Analysis, 26 (1998) 549-564.

[9-13] H.B. Zhang, X.C. Hu, M. Cao, N. Zhang, W.Z. Cui, The quantitative effect of thermal treatment on the secondary electron yield from air-exposed silver surface, Vacuum, 102 (2014) 12-15.

[9-14] J. Puech, C.E. Miquel-España, D. Raboso, EVEREST-consortium, Synthesis of the results of the EVEREST project, in: MULCOPIM 14, Valencia, Spain, 2014.

[9-15] M. Belhaj, T. Gineste, J. Puech, Effect of xenon etching on electron emission properties of dielectric and metallic samples, in: Spacecraft Charging Technology Conference, ESA/ESTEC, Netherlands, 2016.

[9-16] N. Hilleret, C. Scheuerlein, M. Taborelli, The secondary-electron yield of air-exposed metal surfaces, Appl. Phys. A-Mater. Sci. Process., 76 (2003) 1085-1091.

[9-17] V. Baglin, J. Bojko1, O. Gröbner, B. Henrist, N. Hilleret, C. Scheuerlein, M. Taborelli, The secondary electron yield of technical materials and its variation with surface treatments, in: Proceedings of EPAC 2000, Vienna, Austria, 2000.

[9-18] F. Le Pimpec, F. King, R. E. Kirby, M. Pivi, Secondary Electron Yield Measurements of TiN Coating and TiZrV Getter Film, 2003.

[9-19] B. Johnson, K. G. McKay, Secondary Electron Emission of Crystalline MgO, 1953.

[9-20] M. Buyanova, V.E. Semenov, D. Anderson, M. Lisak, J. Puech, V.J.R. M., Influence of secondary emission yield on the saturation properties of multipactor discharges between two parallel metal plates, Phys. Plasmas, 17 (2010) 043504.

[9-21] M. Belhaj, K. Guerch, P. Sarrailh, N. Arcis, Temperature effect on the electron emission and charging of BN-SiO2 under low energy electron irradiation, Nuclear Instruments and Methods in Physics Research Section B: Beam Interactions with Materials and Atoms, 362 (2015) 163-166.

[9-22] N. Bundaleski, M. Belhaj, T. Gineste, O.M.N.D. Teodoro, Calculation of the angular dependence of the total electron yield, Vacuum, 122 (2015) 255-259.

[9-23] R.E. Kirby, F.K. King, Secondary electron emission yields from PEP-II accelerator materials, Nuclear Instruments and Methods in Physics Research Section A: Accelerators, Spectrometers, Detectors and Associated Equipment, 469 (2001) 1-12.

[9-24] T. Gineste, M. Belhaj, N. Bundaleski, O.M.N.D. Teodoro, C. Pons, J. Puech, N. Balcon, Experimental investigation of the influence of electron incidence angle on the Total Electron Emission Yield of silver, in: 2013 IEEE 14th International Vacuum Electronics Conference (IVEC), 2013, pp. 1-2.

[9-25] N. Balcon, D. Payan, M. Belhaj, T. Tondu, V. Inguimbert, Secondary Electron Emission on Space Materials: Evaluation of the Total Secondary Electron Yield From Surface Potential Measurements, IEEE Transactions on Plasma Science, 40 (2012) 282-290.

[9-26] A. Melchinger, S. Hofmann, W. W., Dynamic double layer model: Description of time dependent charging phenomena in insulators under electron beam irradiation, Journal of Applied Physics, 78 (1995) 6224-6232.

[9-27] M. Belhaj, T. Tondu, V. Inguimbert, Experimental investigation of the effect of the internal space charge accumulation on the electron emission yield of insulators submitted to e-irradiation: application to polycrystalline MgO, Journal of Physics D: Applied Physics, 42 (2009) 145306.

[9-28] H.-J. Fitting, J. Boyde, Monte-carlo calculation of electron attenuation in SiO2, physica status solidi (a), 75 (1983) 137-142.

[9-29] M. Belhaj, K. Makasheva, G. Teyssedre, Effect of charging on the secondary electron emission, in: IEEE International Conference on Plasma Science (ICOPS) Banff Canada 2016.

[9-30] M. Belhaj, T. Tondu, V. Inguimbert, Effect of the incident electron fluence on the electron emission yield of polycrystalline Al2O3, Applied Surface Science, 257 (2011) 4593-4596.